FINAL REPORT

Energy Efficient, Ultra Low NO_x Industrial Gas Burners

Prepared for

California Institute for Energy Efficiency
Contract 4901510

South Coast Air Quality Management District
Contract 95152

California Air Resources Board California Air Resources Board
Contract 95-310

COMBUSTION LABORATORY

Project Technical Lead

Dr. G. S. Samuelsen

UCI Combustion Laboratory
University of California
Irvine, California 92697-3550

UCICL-ARTR-95-7(s-1)

June 2000

ABSTRACT

Reducing pollutant emissions from industrial burners is a prime concern in California, especially in regions that do not meet the National Ambient Air Quality Standards established by the federal government. The southern California air basin is a notorious example of such a "non-attainment" area for ozone, or "smog," and carbon monoxide (CO). Controlling and reducing the pollutant emission of nitrogen oxides (NO_x) is required to reduce ozone while carbon monoxide (CO) reduction is required to ensure energy efficient operation. Unfortunately, the simultaneous reduction of both NO_x and CO in burner systems is often times incongruous and results in poor stability with limited operability. The purpose of this program, sponsored by the California Air Resources Board, the South Coast Air Quality Management District, and the California Institute for Energy Efficiency is to address this challenge of reducing NO_x emissions while maintaining high efficiency for industrial, natural-gas fired burner applications. Three tasks are identified to achieve the program goals: (1) conduct support research and technology development on a model burner, including the advancement of the active control strategy for industrial burners, (2) transfer this information and understanding to industrial-manufactured burners at larger scales, including the measurement of air toxics to ensure that hazardous air pollutants are not increased as a result of low NO_x operation, and (3) provide input to the burner manufacturers for practical applications and demonstrations based on the previous tasks findings.

All three tasks were successfully achieved during the course of the five year program. The major contributions from the program are described below.

Task 1

- Established methodology and strategy for conducting mechanistic studies in complex systems.
- Determined that perfect premixing is not the optimum in terms of emissions and stability for the burner studied.
- Upgraded the active control methodology to include a modular design with improved hardware, software, and cost function.
- Demonstrated the active control system on an industrial burner from Coen.

Task 2

- Demonstrated effectiveness of statistical tool called design of experiments (DoE) for optimizing industrial burner hardware configurations.
- Provided data for burner manufacturers to use in present/future burner designs (see Task 3).

Task 3

- Provided input for design and testing of two commercial burner systems: Maxon SmartFire system and the Coen *QLN* burner.
- Established interaction and protocols for working with industrial partners with goal of commercializing research findings.

TABLE OF CONTENTS

1. INTRODUCTION 1

2. GOALS AND OBJECTIVES 3

3. BACKGROUND 4
   - 3.1. Industrial Burner Types 4
   - 3.2. Traditional Pollution Control 4
   - 3.3. Active Control for the Next Generation Burners 6

4. APPROACH 7
   - 4.1. Attaining Performance 7
   - 4.2. Maintaining Performance 7

5. FACILITIES AND DIAGNOSTICS 8
   - 5.1. Optical Access Furnace 8
   - 5.2. High Temperature Furnace 14
   - 5.3. Diagnostics 17
   - 5.4. Modeling 22

6. TASK 1 – TECHNOLOGY DEVELOPMENT AND SUPPORT RESEARCH 25
   - 6.1. Generic Burner Exhaust Measurements: Screening Studies 25
   - 6.2. Detailed Measurements 34
   - 6.3. Throat Investigations 42
   - 6.4. Summary of Mechanistic Findings 46
   - 6.5. Active Control Development 50

7. TASK 2A – BOILER SIMULATOR 57
   - 7.1. Design of Experiments Methodology 57
   - 7.2. Design Optimization 60
   - 7.3. Design of Experiments Analyses 65
   - 7.4. Characterization Measurements 74
   - 7.5. Reproducibility and Modified *QLN* 87
   - 7.6. Task 2A Summary 91

8. TASK 2B – MAXON, HIGH TEMPERATURE BURNER 93
   - 8.1. Design of Experiments 93
   - 8.2. Reaction Images 97
   - 8.3. Velocity Measurements 99
   - 8.4. Fuel Distribution 101
   - 8.5. Task 2B Summary 103

9. HAZARDOUS AIR POLLUTANTS AND OZONE PRECURSORS 105
   - 9.1. Goals and Objectives 105
   - 9.2. Survey of Emissions from Natural Gas Combustion 105
   - 9.3. Selection of Target Compounds 107

9.4. Approach 108
9.5. Experiment 110
9.6. Results 114
9.7. Summary 126

10. TASK 3 – SUPPORT TO PRACTICAL APPLICATIONS 129
10.1. Maxon Interaction 129
10.2. Coen Interaction 129

11. SUMMARY 131
11.1. Task 1: Support Research and Technology Development 131
11.2. Task 2: Industrial Burner Simulator Development 131
11.3. Task 3: Support to Practical Applications 132
11.4. Major Products and Contributions 133

12. REFERENCES 134

13. APPENDIX: AIR TOXICS DATA 137

LIST OF FIGURES

Figure 1.1: South Coast Air Basin and California NO_x Emission Sources 1
Figure 1.2: South Coast Air Basin and California CO Emission Sources 2
Figure 1.3: South Coast Air Basin and California Reactive Organic Gas Emission Sources 2
Figure 5.1: Furnace Floor and Burner Exit Dimensions 8
Figure 5.2: Furnace Enclosure with Water-Cooled Panels 9
Figure 5.3: Test Stand Traverse with Furnace Enclosure 9
Figure 5.4: Model Industrial Burner 10
Figure 5.5: Fuel Injectors 12
Figure 5.6: Scaled *QLN* Burner (Coen Company, Inc.) 13
Figure 5.7 Furnace Side Views 14
Figure 5.8 Cut-away View of Simulator 15
Figure 5.9: Maxon *Kinedizer* 16
Figure 5.10: Emissions Sampling Train 18
Figure 5.11: In-Furnace Video Camera and Air-Cooled Jacket 19
Figure 5.12: Bottom Window Backscatter Laser Anemometry Setup 21
Figure 5.13: Top Window Backscatter Laser Anemometry Setup 21
Figure 5.14: Near-Field Injection Model 23
Figure 6.1: NO_x and CO Emissions (corrected to 3% O_2) 26
Figure 6.2: NO_x vs. CO Emissions Trade-off 27
Figure 6.3: $f([NO_x])$ and $g(\eta)$ Contributions to J 29
Figure 6.4: Performance Indices 30
Figure 6.5: NO_x vs. S' at Various Excess Air Levels 31
Figure 6.6: CO vs. S' at Various Excess Air Levels 32
Figure 6.7: Premixed and Counter-swirl Performance 33
Figure 6.8: Performance Map and Selected Conditions 33
Figure 6.9: Reaction Photographs 35
Figure 6.10: Streamlines, NO_x, and Temperature Overlays for Co-swirl Injector at 20% Excess Air, S'=0.52 ② 36
Figure 6.11: Streamlines, NO_x, and Temperature Overlays for the Radial Injector at 5% Excess Air, S'=0.62 ③ 37
Figure 6.12: Streamlines, NO_x, and Temperature Overlays for Counter-swirl Injector at 20% Excess Air, S'=0.66 ⑦ 38
Figure 6.13: NO_x versus Recirculation Zone Size 39
Figure 6.14: Performance versus Recirculation Zone Size 39
Figure 6.15: In-Quarl Sampling Grid 40
Figure 6.16: Local Equivalence Ratios at Quarl Exit (z=1.0 inch) 41
Figure 6.17: Local Equivalence Ratios Inside Quarl (z=0.5 inches) 41
Figure 6.18: Local Equivalence Ratios at Quarl Exit 42

Figure 6.19: Acetone PLIF Fluorescence at Burner Throat 43
Figure 6.20: Modeling Predictions for Fuel Mole Fractions at Annulus Wall 43
Figure 6.21: Modeling Predictions for Fuel Mole Fractions at Burner Throat 44
Figure 6.22: Quartz Quarl Video Setup 44
Figure 6.23: Ignition Region Size Comparison 45
Figure 6.24: The Effect of Increasing Swirl and Excess Air 45
Figure 6.25: Reaction Mechanism for Model Industrial Burner 48
Figure 6.26: Performance vs. Swirl Intensity at 20% Excess Air for Co-swirl and Counter-swirl Injectors 49
Figure 6.27: Active Control Strategy 50
Figure 6.28: Second Generation Active Control Concept 51
Figure 6.29: Active Control System Schematic 52
Figure 6.30: *QLN* Burner Performance Map 53
Figure 6.31: *QLN* Active Control History [① start, ② finish] 54
Figure 6.32: *QLN* Burner Performance Map with System Efficiency Factor 54
Figure 6.33: *QLN* Active Control with System Efficiency Factor [① start, ② finish] 55
Figure 6.34: *QLN* Burner Performance Map with Adjusted Weighting Factors 55
Figure 7.1: Variable Geometric Parameters on Subject Burner 58
Figure 7.2: Statistical Effects for a Full 2-Level Factorial with Six Factors 59
Figure 7.3: Image of First 10 Runs from Design of Experiments Test Matrix 60
Figure 7.4: Impact of Core Fuel Flow on NO_x Emissions and Stability 61
Figure 7.5: Summary of Six Factors in DoE Test Matrix 63
Figure 7.6: Complete Design of Experiments (DoE) Test Matrix 64
Figure 7.7: Standard Form of 10% Blocked Matrix with Coded Factors 66
Figure 7.8: Yates's Algorithm Calculations for Effects on NO_x Response 67
Figure 7.9: ANOVA Output for NO_x Response in 10% Blocked Matrix 68
Figure 7.10: Diagnostic Graphs for NO_x Response in 10% Blocked Matrix 69
Figure 7.11: Half-Normal Probability Plot of NO_x Response 70
Figure 7.12: Cube Plot of NO_x (ppm) Response (10% Excess Air Blocked Matrix) 71
Figure 7.13: Square Plots of NO_x (ppm) Response 72
Figure 7.14: Normal Probability Plot of Combustion Efficiency Response 72
Figure 7.15: Normal Probability Plot of System Efficiency Response 73
Figure 7.16: Normal Probability Plot of System Efficiency Response (Full DoE Matrix) 73
Figure 7.17: High and Low Performance Burner Settings 74
Figure 7.18: Temperatures for Low Performance Condition 76
Figure 7.19: Equivalence Ratios for Low Performance Condition 77
Figure 7.20: NO_x Concentrations for Low Performance Condition 78
Figure 7.21: Temperatures for High Performance Condition 79
Figure 7.22: Equivalence Ratios for High Performance Condition 80
Figure 7.23: NO_x Concentrations for High Performance Condition 81
Figure 7.24: Axial Velocities for the Low Performance Condition 83

Figure 7.25: Axial Velocities for the High Performance Condition 84
Figure 7.26: Axial and Radial Velocities for Low Performance Condition at 1.50" Downstream of Throat Exit 85
Figure 7.27: Axial and Radial Velocities for High Performance Conditions at 1.50" Downstream of Throat Exit 86
Figure 7.28: Images of the High and Low Performance Conditions 87
Figure 7.29: Repeated Half-Normal Probability of NO_x Response – QLN_O 88
Figure 7.30: Cube Plot of NO_x Response – QLN_O 89
Figure 7.31: Half-Normal Probability Plot of NO_x Response – QLN_Γ 90
Figure 7.32: Cube Plot of NO_x Response – QLN_Γ 90
Figure 7.33: Half-Normal Probability Plot of Combustion Efficiency Response – QLN_Γ 91
Figure 8.1: Results from test #1 of effects on NO_x 94
Figure 8.2: Results from test #1 of effects on η 94
Figure 8.3: Results from test #2 of effects on NO_x 94
Figure 8.4: Results from test #2 of effects on η 95
Figure 8.5: Results from test #3 of effects on NO_x 95
Figure 8.6: Results from test #3 of effects on η 96
Figure 8.7: Results from test #4 of effects on NO_x 96
Figure 8.8: Results from test #4 of effects on η 96
Figure 8.9: Results from test #5 of effects on NO_x 97
Figure 8.10: Results from test #5 of effects on η 97
Figure 8.11: Reaction Image of Low Air Swirl Case 98
Figure 8.12: Reaction Image of High Air Swirl Case 98
Figure 8.13: Axial Velocity Exiting the Burner at Two Planes and for Two Cases 99
Figure 8.14: Plot of Tangential Velocity Profiles (Along X = 0 Axis) 100
Figure 8.15: Plot of Radial Velocity Profiles (Along Y = 0 Axis) 101
Figure 8.16: Fuel Distribution Contour for Case 1 102
Figure 8.17: Fuel Distribution Contour for Case 2 102
Figure 8.18: Fuel Distribution Contour for Case 3 103
Figure 9.1: Photographs of Burner Reaction Zone Operating at Source Test Conditions 112
Figure 9.2: Generic Burner Performance Map (Adapted from Miyasato and Samuelsen, 1995) 112
Figure 9.3: VOC Profile for Generic Burner Test G1 115
Figure 9.4: VOC Profile for Generic Burner Test G2 116
Figure 9.5: VOC Profile for Generic Burner Test G3 116
Figure 9.6: VOC Profile for Generic Burner Test G4 117
Figure 9.7: VOC Profile for Generic Burner Test G5 117
Figure 9.8: VOC Profile for Boiler Burner Test B1 118
Figure 9.9: VOC Profile for Boiler Burner Test B2 119
Figure 9.10: VOC Profile for Boiler Burner Test B3 119
Figure 9.11: VOC Profile for High Temperature Burner Test F1 120
Figure 9.12: VOC Profile for High Temperature Burner Test F2 120

Figure 9.13: VOC Profile for High Temperature Burner Test F3 121
Figure 9.14: VOC Profile for High Temperature Burner Test F4 121
Figure 9.15: VOC Profile for Natural Gas Supply 122
Figure 9.16: [Target VOCs] vs. [CO] for the Generic Burner 122
Figure 9.17: [Target VOCs] vs. [CO] for the Boiler Burner 123
Figure 9.18: Normalized High Temperature Burner Pollutant Concentrations vs. Stack Position 123
Figure 9.19: Chemical Kinetic Modeling Results at 5% Excess Air and 2000°F 125
Figure 9.20: Chemical Kinetic Modeling Results at 5% Excess Air and 1800°F 125
Figure 10.1: Maxon *SmartFire* System 129
Figure 10.2: Coen *QLN* Low NO_x Burner 130
Figure 10.3: Coen *QLN* Modeling of UCICL Optical Furnace 130

LIST OF TABLES

Table 3.1: National and California Ambient Air Quality Standards 5
Table 3.2: Emissions Standards for New Boilers in South Coast Air Basin 5
Table 5.1: Natural Gas and Air Operating Parameters 11
Table 5.2: Laser Induced Fluorescence Wavelengths 20
Table 5.3: Diagnostic Techniques Applied to Experiment 22
Table 6.1: Selected Conditions 34
Table 6.2: Results Summary 47
Table 9.1. OP and HAP Emissions from Selected Fuel Lean Gas-Fired Combustion Systems 107
Table 9.2: Target Analytes 109
Table 9.3: Generic Burner Test Conditions 111
Table 9.4: Boiler Burner Test Conditions 113
Table 9.5: High Temperature Burner Test Conditions 114
Table 13.1 VOC Concentrations (in ppbC @ 3% O2) for *QLN* Burner 137
Table 13.2: VOC Concentrations (in ppbC @ 3% O_2) for Generic Burner 138
Table 13.3: VOC Concentrations (in ppbC @ 3% O_2) for Furnace 139
Table 13.4: VOC Concentrations (in ppmC) in Natural Gas Supply 140

LIST OF ACRONYMS AND SYMBOLS

CARB	California Air Resources Board
CIEE	California Institute for Energy Efficiency
CO	Carbon monoxide
DoE	Design of Experiments
EA	Excess air
η	Combustion efficiency'
FGR	Flue gas recirculation
HAPs	hazardous air pollutants as defined by the EPA, which includes 188 compounds
J	performance index
NO_x	Nitrogen oxides
OPs	ozone precursors, subset of HAPs
QLN	Quantum Low NO_x (Coen Company burner)
S'	Input swirl intensity for model industrial burner
SCAQMD	South Coast Air Quality Management District
VOCs	volatile organic compounds, subset of HAPs

ACKNOWLDEGEMENTS

The research reported in this document spans over five years of funding provided by the California Institute for Energy Efficiency (CIEE), South Coast Air Quality Management District (SCAQMD), and the California Air Resources Board (CARB). Appreciation is expressed to the program monitors, specifically Dr. Jim Cole of CIEE, Andy Abele of SCAQMD, and Ralph Propper and Manjit Ahuja of CARB. The guidance from individuals on the Project Advisory Committee was also of great importance, and we thank Cherif Youssef and Henry Mak of Southern California Gas Company, and David Hatfield of the California Energy Commission for their input. The collaboration with Lawrence Livermore National Laboratories and Dr. Charles Westbrook for the air toxics kinetic modeling is also thankfully acknowledged. Finally, this work would not have been possible without the efforts of the students conducting the research; thanks are extended to Doug Brouwer, Chris Weakley, Ary Chang, and Trevor Demayo.

DISCLAIMER

This report was prepared as a result of work sponsored, paid for, in whole or in part by the California Institute for Energy Efficiency (CIEE), the South Coast Air Quality Management District (SCAQMD), and the California Air Resources Board (CARB). The opinions, findings, conclusions, and recommendations are those of the authors and do not necessarily represent the views of CIEE, SCAQMD, or CARB. CIEE, SCAQMD, and CARB, their officers, employees, contractors, and subcontractors make no warranty, expressed or implied, and assume no legal liability for the information in this report. CIEE, SCAQMD, and CARB have not approved or disapproved this report nor has CIEE, SCAQMD, or CARB passed upon the accuracy or adequacy of the information contained herein.

EXECUTIVE SUMMARY

Low emissions technologies are driving the development of new generation stationary power sources. The next generation industrial burners will be required to maintain extremely low levels of nitrogen oxides (NO_x) and carbon monoxide (CO) emissions. In 1990, the California Institute for Energy Efficiency (CIEE) established a program to investigate attaining these low levels of low NO_x and low CO in industrial burners using rapid fuel and air mixing. A further goal was to assess the viability of active control to these complex industrial systems. During this CIEE Phase I program, rapid mixing of the fuel and air was demonstrated to provide low NO_x and low CO emissions in a model industrial, natural gas-fired burner, and the proof-of-concept active control demonstration was completed.

In order to expand upon these promising findings, a basic understanding of the pollutant formation mechanisms in these complex, industrial burners is required. The goals of the current program, initiated in 1995 and sponsored by the California Air Resources Board (CARB), the South Coast Air Quality Management District (SCAQMD), and CIEE; have been to do just that by investigating the pollutant formation mechanisms in industrial burners and then apply this understanding to larger systems. Three specific tasks were identified to accomplish these goals: (1) technology development and support research on the small-scale, model burner, (2) transfer of the results and understanding to larger-scale boiler and furnace simulators, and (3) support and guidance input to practical burner applications and demonstrations.

Task 1 – Technology Development and Support Research

The first task was considered the discovery phase, where detailed measurements and modeling were conducted on a laboratory-scale, generic industrial burner to identify pollutant formation mechanisms. Extensive parametric variations and exhaust emissions measurements were conducted to determine relationships between input parameters and NO_x and CO emissions (performance). Detailed in-situ measurements (laser diagnostics for velocity, temperature, species concentration) were conducted on selected conditions to further investigate the pollutant formation mechanisms. The results provided relationships between input parameters (e.g., fuel jet velocity and swirling air velocity), fuel-air mixing, and performance. The fuel injection strategy that provided the fastest mixing (counter-swirl injector) prior to reaction demonstrated the optimum performance at higher excess air levels. Due to interaction with the swirling air, at lower excess air levels, the co-swirl injector provided better performance. The changing fuel injection strategy with excess air level demonstrated the need for active optimization of the fuel-air mixing for consistent peak performance over the turndown of the burner.

Task 1 also involved developing the experience and systematic methodology for acquiring this understanding, i.e., the journey or pathway of discovery was also important. This methodology includes the established scientific method but also incorporates statistical design of experiments (DOE) and computational fluid dynamic modeling (CFD). Both of these techniques helped to verify or further refine the mixing hypotheses developed through the detailed measurements. The computational fluid dynamic modeling, for example, agreed with the hypothesis that the counter-swirl injector provides the best mixing prior to reaction.

Also, as part of Task 1, further development of the active control methodology was developed. The real-time optimization of an industrial burner to its own emissions was accomplished on a burner designed and built by a major burner manufacture, Coen Company. The improvements made to the active control methodology established in the Phase I program also included the implementation of updated data acquisition software, modular and more portable software coding, and incorporation of system efficiency into the cost (or performance) function.

Task 2 – Boiler and Furnace Simulations

The second task was to design and build two different types of industrial burner simulators to apply the understanding gained in Task 1 to different applications and different sized burners. Two specific burner applications were targeted, boiler burners and high temperature burners. For both applications, UCI teamed with an industrial burner manufacturers to develop and test burner strategies for low NO_x emissions and control. The boiler burner partner was Coen Company, and the high temperature burner partner was Maxon Corporation. In both cases, the manufacturer's provided the burners such that actual hardware was tested. For the high temperature burner testing, a new test facility was designed and constructed to simulate the necessary adiabatic environment. Extensive parametric variations were conducted on the two systems using statistical DoE to identify the major parameters responsible for NO_x and CO emissions. The DoE enabled the selection of optimum conditions. These conditions were then the subject of more detailed measurements, such as laser anemometry, to determine the mechanisms responsible for the good and bad performance in terms of NO_x and CO emissions.

Another significant finding involved the extensive air toxics emissions measurements conducted for the industrial burners. This work was completed in order to ensure that low NO_x emission operation was not accomplished at the expense of emitting more toxic air pollutants. Hazardous air pollutants and ozone precursors were measured from the exhaust of the generic model burner, the scaled Coen boiler burner, and the high temperature Maxon burner. The results show that under certain conditions, the air toxics emissions can be elevated, especially when high levels of excess air and quenching can occur. The boiler burner exhibited the lowest levels, followed by the generic burner. The high temperature burner exhibited the highest amounts of volatile organic compound emission when operating in incinerator mode. The suspected cause for these elevated levels is a quenching mechanism and reduced residence time under certain operating conditions. This scenario was further verified using chemical kinetic modeling.

Task 3 – Support to Practical Burner Applications and Demonstrations

The third task has been accomplished through the interactions with the industrial partners, Maxon Corporation and Coen Company. Maxon Corporation is employing a control system setup in their commercial *SmartFire* burner system which is very similar to the initial CIEE Phase I active control testing methodology. For this testing, the complete burner operating envelope was mapped with NO_x and CO emissions in order to determine whether the active control system would in fact find the optimum condition. Maxon adopted a similar strategy for their *SmartFire* system by conducting full burner operating envelope maps at their test facility and programming the optimum conditions into their burner controls. This established a closed-loop, feed-forward ("lookup table) control scheme.

In working with Coen, two major results came out of the interaction. First, the smaller-scale burner was tested in the facility and shown to exhibit the same characteristics of the larger-scale, commercial burners. This validated the test facility for working on smaller-scale burners with the intent of discovery and scaling up to commercial sizes. The second finding was that the staged burner concept was not suited for ultra-low NO_x emissions without the addition of flue gas or another diluent. This further verified Coen's pursuit of other burner strategies for reducing NO_x emissions to lower and lower levels.

Comparative Assessment of Results and Objectives

All three tasks were completed within the spirit of the program goals and objectives. The only discrepancies between the objectives and the results occurred under Task 2 where the maximum firing rate of 4 MMBtu/hr for the boiler simulator was not achieved. The reasons for limiting the firing rate to 0.4 MMBtu/hr were twofold: (1) the cost to design and construct the boiler facility in parallel with the high temperature furnace was prohibitive and (2) the existing optical facility, with modifications, was better suited for obtaining the detailed laser measurements. The first challenge resulted from originally

underestimating the cost for constructing two large, new burner facilities. This was further complicated when the campus prohibited the use of the chilled water supply for experiment cooling due to the growing demand for air conditioning. As a result, the intended heat sink for the boiler was taken away and a new source was required, such as a cooling tower. This added cost and the higher than expected furnace simulator costs dictated that an existing infrastructure be utilized for the boiler burner studies. The modifications applied to the existing optical furnace test facility are described in the following section.

Problems and Resolutions

In order to utilize the existing optical furnace, several large modifications were required to allow as large a firing rate as possible for the facility. The maximum throughput was determined to be 400,000 Btu/hr based on the exhaust capabilities of the test cell. In order to simulate the radiative section of a boiler, and prevent material failure due to the increased heat load, a new furnace enclosure was fabricated consisting of a stainless steel frame with removable water-cooled walls. The test cell infrastructure was also modified to accommodate this water cooling circuit as well as adding two metered fuel injection lines and an air line for higher capacities.

Comparative Assessment of Costs

The total budgeted cost of $225,000 (CARB), $300,000 (SCAQMD), and $1,110,271 (CIEE) were expended over the five-year program. No cost overruns or savings were incurred.

1. INTRODUCTION

It has been well documented that pollutant emissions from combustion sources play a major role in local air quality. It is now also becoming apparent that emissions from combustion sources play a large role in regional and global air quality due to chemical reactions in the atmosphere and transport to the upper troposphere. As a result, regulatory agencies have legislated strict emissions standards on stationary combustion sources to mitigate the atmospheric damage caused by these combustion devices. Specifically, oxides of nitrogen (NO_x) and carbon monoxide (CO) have the most strict federal emissions standards due to their toxicity and role in the formation of photochemical oxidant (i.e., smog). These standards are even lower in southern California, where the large population density and atmospheric conditions combine to produce the worst air quality in the nation. In order to maintain industrial burner activity and economic competitiveness in California, especially southern California, low polluting technologies are required. This research program addresses these issues by investigating in-flame techniques to produce low NO_x and low CO emitting industrial burners.

Nitrogen oxides consist of nitric oxide (NO) and nitrogen dioxide (NO_2) and are emitted from all air-breathing combustion systems. Although the automobile is the most dominant emitter of NO_x, stationary sources also contribute a large amount. As shown in Figure 1.1, industrial burners account for approximately 7% of all NO_x emitted in the southern California air basin and 13% of all NO_x emitted in California according to emissions inventories compiled by the California Air Resources Board (CARB).

To reduce NO_x emissions from industrial burners, "cleaner" fuels have been employed. For example, natural gas is required at all industrial sites in southern California. However, even when burning natural gas, which is considered the cleanest fossil fuel, copious amounts of NO_x can still be emitted depending on the application of the process which dictates the fuel injection and the temperature of the combustion device. With the regulatory climate becoming more and more stringent, especially in areas notorious for poor air quality, manufacturers and end-users are seeking technologies to minimize NO_x emissions from industrial burners in order to foster economic progress without harming the environment.

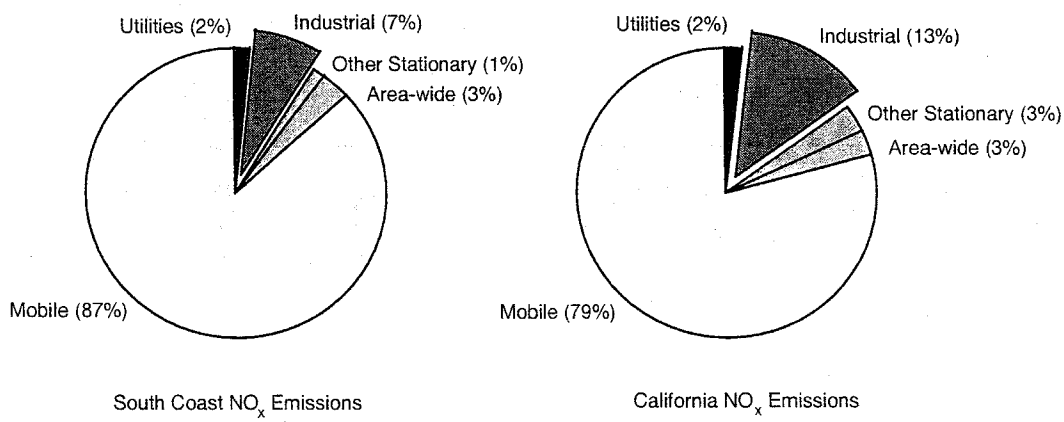

Figure 1.1: South Coast Air Basin and California NO_x Emission Sources (adapted from CARB, 1997)

Current methods of NO_x control rely on post–combustion treatment, off-stoichiometric combustion, or internal flue gas recirculation methods (Bentley and Jelinek, 1989; Eskinazi *et al.*, 1989; and EPA, 1992). Low NO_x burner technologies, which rely on empirical, trial-and-error, or case-specific fuel and air delivery strategies to achieve performance goals, are regularly limited by a reduction in stability and combustion efficiency due to the typically lean operating conditions or diluent injection required. This

reduced combustion efficiency is marked by poor CO burnout and higher CO emissions, which not only increases operating costs but also contributes to ozone production in the atmosphere. Thus, although mobile sources are the primary emitter of CO (see Figure 1.2), low NO_x emissions must be achieved while maintaining low CO emissions in industrial burners such that one evil is not traded for another.

There has also been recent concern regarding air toxics or hazardous air pollutants from industrial burners. The estimated amount of reactive organic gases emitted by source is shown in Figure 1.3 according to the emissions inventories of the CARB. As with CO, the emissions from industrial burners are small compared to other sources. However, the ozone forming potential of these reactive organic gases in the atmosphere can be significant despite the low concentration levels. As such, air toxic emissions should be investigated to ensure that they are not formed and released as a byproduct of favorable NO_x and CO operation in industrial burners.

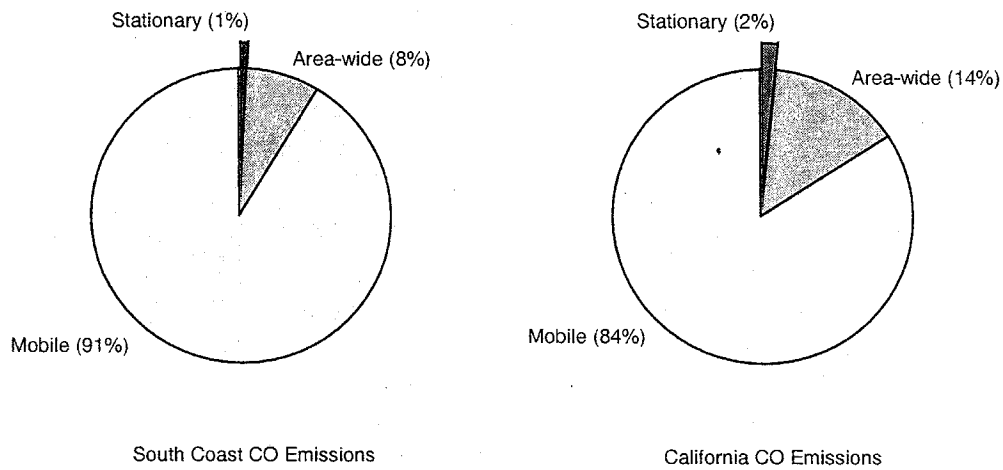

Figure 1.2: South Coast Air Basin and California CO Emission Sources (adapted from CARB, 1997)

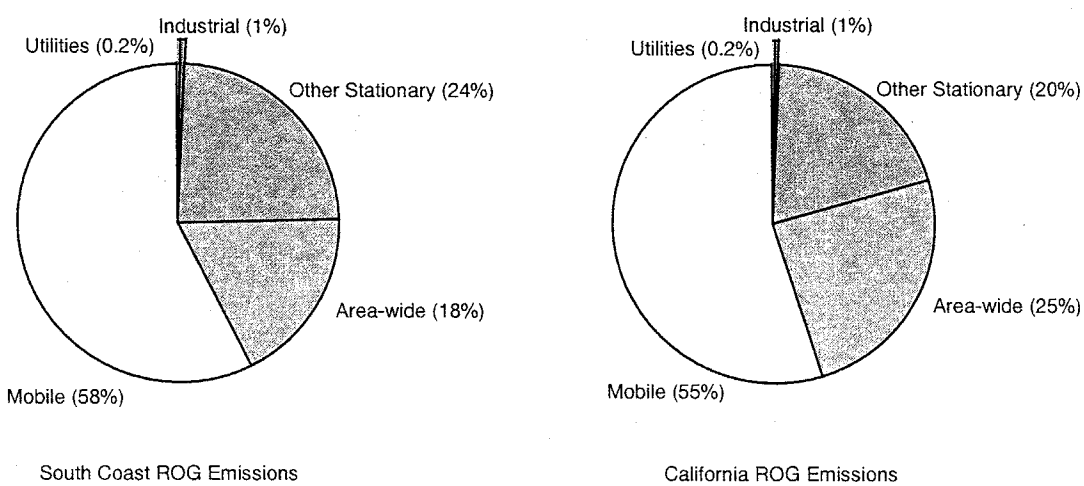

Figure 1.3: South Coast Air Basin and California Reactive Organic Gas Emission Sources (adapted from CARB, 1997)

2. GOALS AND OBJECTIVES

The current program sponsored by CARB, South Coast Air Quality Management District (SCAQMD), and the California Institute for Energy Efficiency (CIEE) was established in 1995 to further advance low NO_x burner technology by investigating the mechanisms of NO_x and CO formation in different, realistic industrial systems. This understanding would then be used to apply active control to these industrial systems in order to attain and maintain optimum performance despite changes to the burner environment. The specific tasks identified at the program outset have served as the program objectives.

Task 1 – Technology Development and Support Research

1.1. Conduct tests to develop detailed understanding of fuel-air mixing on performance

1.2. Develop improved numerical modeling and experimental diagnostic techniques to enhance the mechanistic understanding of burner performance.

1.3. Develop a systematic approach to understanding mechanisms for ultra-low NO_x emissions.

1.4. Develop an active control methodology for the ultra-low NO_x burner systems developed during the project.

Task 2 – Boiler and Furnace Simulators

2.1. Design a boiler and high temperature simulator with maximum firing rates of 4 MBtu/hr.

2.2. Fabricate and install the simulators.

2.3. Evaluate operation of simulators to ensure design criteria are met.

2.4. Test prototype ultra-low NO_x burners

2.5. Measure hazardous air pollutant levels from these industrial burners.

Task 3 – Support to Practical Burner Applications and Demonstrations

3.1 Provide burner design input to commercial burner manufacturer for a field demonstration application of a boiler burner.

3.2 Provide burner design input to commercial burner manufacturer for a field demonstration application of a high temperature burner.

3. BACKGROUND

3.1. Industrial Burner Types

Industrial burners are used for a myriad of heating applications: boilers, process heating, paint drying, baking, oxidation of process gas, steel annealing, cement kilns, glass melting, etc. The two target applications addressed in this program are boilers and high temperature process heating (e.g., process gas oxidation) due to their presence everywhere in the industrial marketplace. The two types of combustion devices are defined below with their respective emissions limits according to the SCAQMD. This agency's limits are used because these are the most stringent in the nation and therefore provide the ultimate standard of measure.

3.1.1. Boiler and Steam Generator Applications

The SCAQMD defines industrial boilers or steam generators as

> any combustion equipment fired with liquid and/or gaseous and/or solid fossil fuel and used to produce steam or to heat water and that is not used exclusively to produce electricity for sale. Boiler or Steam Generator does not include any waste heat recovery boiler that is used to recover sensible heat from the exhaust of a combustion turbine or any unfired waste heat recovery boiler that is used to recover sensible heat from the exhaust of any combustion equipment. (SCAQMD, Rule 1146)

The challenge with these types of burners is to reduce NO_x emissions while maintaining high combustion efficiency and good stability.

3.1.2. High Temperature Applications

This burner application is more generic and can be applied to process heating, metal mixing, volatile organic compound oxidation, as well as other high temperature fuel–air/furnace applications. Since high temperature applications allow for downstream oxidation of CO, combustion efficiencies are typically very high. The main challenges with these burners are to concurrently reduce NO_x emissions without impacting the necessary high temperatures required for the process.

3.2. Traditional Pollution Control

The ambient air quality standards in California are stricter than the federal standards, as shown in Table 3.1. Furthermore, in order to remain competitive in a region, industrial burners must meet the local emissions limits, and the strictest limits are in southern California imposed by the SCAQMD. The NO_x and CO limits for new or retrofitted industrial burners based on the "best available control technology" (BACT) are shown in Table 3.2. These technologies and their costs are from SCAQMD BACT applications (SCAQMD, 2000). Descriptions of the techniques required to meet these strict emissions limits are provided in the following sections.

Table 3.1: National and California Ambient Air Quality Standards

Species	*Type of Average*	*Federal Limit*	*California Limit*
CO	1 hour 8 hour	35 ppm 9 ppm	20 ppm
NO_2	1 hour	0.053 ppm *	0.25 ppm
Ozone	1 hour 8 hour	0.12 ppm 0.08 ppm	0.09 ppm

* Annual arithmetic mean

Table 3.2: Emissions Standards for New Boilers in South Coast Air Basin

Application	*NO_x (ppm)*	*CO (ppm)*	*BACT Technology*	*Cost x $1000*
Boilers, Steam Generators, and Process Heaters	9–12*	50–100	Ultra Low NO_x Burner	$30–110
	7	50	Selective Catalytic Reduction	$250–300
	5	50	Low Temperature Oxidation	$400-500

* Ranges shown are due to size (heat rate) considerations

3.2.1. Post Combustion Techniques (SCR, SNCR, LTO)

The traditional methods of pollutant emissions control have been exhaust gas "cleanup," using techniques downstream of the combustion process. The major techniques utilized are selective non-catalytic reduction (SNCR), selective catalytic reduction (SCR), and a new technique called low temperature oxidation (LTO). All of these strategies rely on injection of a chemical which reduces NO to N_2. For SNCR, ammonia or urea is injected in a region where the temperature is between 1800–2100°F. If the temperature is too high, the ammonia/urea can be oxidized to produce more NO_x. If the temperature is too low, the ammonia/urea does not adequately react with the NO_x and is released unreacted into the atmosphere. For SCR, a catalyst is used to allow the reaction of ammonia and NO_x to occur over a lower temperature range (600–800°F). The optimum temperature window is important for SCR for the same reasons as with SNCR. LTO uses ozone (O_3) injection into the downstream exhaust (300°F) to oxidize NO to nitric acid. The dilute acid is then neutralized with sodium hydroxide to form sodium nitrate, which can then be discharged to the sewer system. All three types of downstream injection strategies require additional storage tanks for the injectant and strict operating temperature windows to prevent "slip," release of the unreacted injectant into the atmosphere. Due to the additional equipment and increased operational and maintenance costs, the costs for these systems are extremely high (as seen in Table 3.2, which is $10–$100/kW), thereby making in-flame NO_x reduction techniques very attractive.

3.2.2. In-Flame Techniques (FGR, Staging, low NO_x Burners)

In-flame NO_x control techniques all rely on burning the fuel and air at off-stoichiometric mixture ratios (i.e., more fuel or air than is necessary for complete combustion). Flue gas recirculation (FGR) is a technique where the exhaust gas is pumped back into the combustion air to dilute and cool the reaction. Staging refers to the technique of injecting some of the fuel downstream such that two combustion zones exist, with both zones at off-stoichiometric ratios such that the temperatures and NO_x are reduced. The

final in-flame technique is employing a low NO_x burner, which typically consists of FGR, staging, or premixing.

These low-NO_x techniques, however, rely on empirical, trial-and-error, or case-specific fuel and air delivery strategies to achieve performance goals at a limited firing rate range. In addition, FGR and premixed burners suffer from poor stability at lean operating conditions. This reduced stability can result in increased CO emission as well as burner damage due to combustion induced oscillations. Furthermore, premixed burners are typically only used for surface (radiant) burners due to flame flashback safety concerns. Since these burners use a ceramic material to radiate and provide the heat transfer, large burners are required to achieve maximum firing rates. These radiant burners also suffer from possible reliability issues since the radiant ceramic material is very fragile.

3.3. Active Control for the Next Generation Burners

In order to ensure constant and reliable operation at optimum conditions, finer control of the burner is required. In addition, with the trend in operation near the stability limits for many of the optimized conditions, fast response is needed to ensure adequate stability. The strategy that has been investigated in this research is that of active control using a feedback sensor. With this strategy, the burner is computer controlled such that it can sense when it is operating in a region of "good" performance (low NO_x and low CO) or, more importantly, when it is in a region of "poor" performance (high NO_x or high CO) such that it can adjust its input parameters to move to a more favorable region of performance. These systems are thus "smart" and can adjust themselves according to prescribed algorithms and sensors feedback. This research documents the further advancement of the active control strategy on an industrial burner system.

4. APPROACH

In order to consistently attain and maintain favorable performance in terms of NO_x, CO, the following general approach was adopted.

4.1. Attaining Performance

Many studies have been conducted on applying improved fuel and air mixing for decreased NO_x production. Often, however, the effect on CO, stability, and the flow field have been excluded, or the mechanisms for the improved emissions characteristics have not been included. In order to tailor the fuel and air mixing, information about the local flow structures is required in order to determine the mechanisms responsible for good and bad emissions performance. Investigation was initiated on a small, model industrial, natural gas-fired burner. These results were then applied to a 4 times larger boiler burner and a then a 40 times larger high temperature furnace burner.

The strategy adopted for improved fuel and air mixing was to incorporate radial fuel injection into a co-flowing, swirling air stream. The radial mixing strategy and two parametric variations on the injection were applied to identify conditions, if any, of low NO_x and low CO as well as conditions of high NO_x and high CO for comparison. In order to understand why the selected conditions gave rise to favorable or unfavorable performance, the flow fields were interrogated using conventional and advanced diagnostic tools, including

- extractive emissions
- laser diagnostics for velocity, species, temperature, and mixing
- computational fluid dynamic modeling
- statistical, multivariate testing

The application of these tools allowed the refinement of the emission production hypothesis and then transition the strategies to the other, larger-scale applications.

4.2. Maintaining Performance

In order to maintain optimum performance over time, with degradation of hardware, through load swings, or changes in the heat content of the fuel, an "active" methodology is required. This system must be self-sensing and "smart," i.e. this system must incorporate active control using a feedback sensor. The feedback characteristics used in these experiments were the stack NO_x and CO emissions, and the variable input parameters used to maintain performance were the amount of excess air and the air swirl strength. Mass flow controllers were used to vary the input flows according to the feedback sensor and a computer algorithm. Several optimizing algorithms were investigated to produce the fastest and most efficient optimization.

The hardware used for this research will be addressed in detail in the following section.

5. FACILITIES AND DIAGNOSTICS

Two major facilities were constructed for the industrial burner research: an optical access furnace facility for burners with firing rates of 100,000 to 400,000 Btu/hr and a high temperature furnace facility for burners with firing rates up to 4 MMBtu/hr.

5.1. Optical Access Furnace

The optical access furnace facility provides a fully flexible test stand for optical and extractive measurement techniques for industrial burner applications. This facility is comprised of an octagonal furnace chamber with 360° optical access, computer controlled flow rates, and integrated emissions data acquisition. The furnace is capable of accommodating up-fired burners from 100,000 – 400,000 Btu/hr. The facility, and two burners used in this research are described in the following sections.

5.1.1. Furnace Enclosure

The test stand consists of a stainless-steel framed octagonal, optically accessible furnace enclosure mounted on a three axis traverse; the furnace geometry is similar to that of Edwards (1988). The furnace enclosure consists of 10 inch wide sides with a nominal diameter of 24 inches. The height of the enclosure, not including the exhaust stack, is 36 inches. The exhaust contracts at a 45° angle from the octagonal enclosure to a 6 inch diameter, 24 inch long stack. The exit contraction and distance from the burner exit provide a well-mixed region for representative exhaust measurements. The octagonal geometry was modeled after the design of Edwards (1988) to provide flat windows for optical access while simulating a common, cylindrical furnace and preserving axial symmetry. The entire furnace volume is 11.34 ft^3. The furnace footprint and burner exit are shown in Figure 5.1.

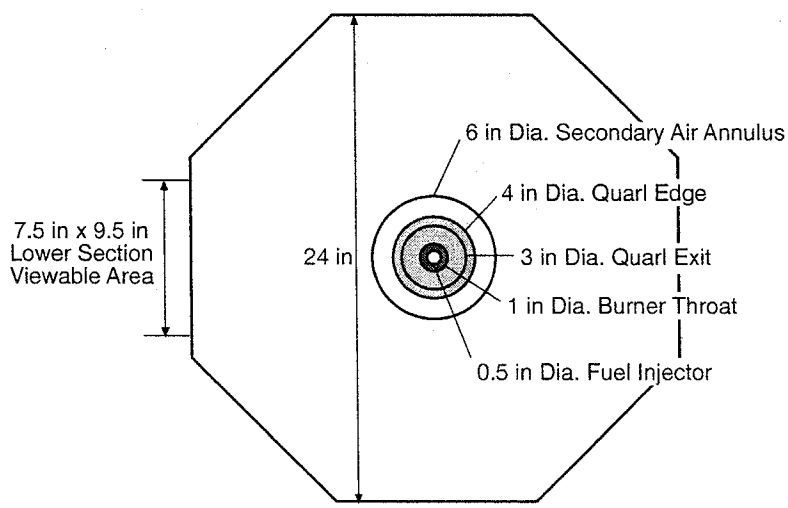

Figure 5.1: Furnace Floor and Burner Exit Dimensions

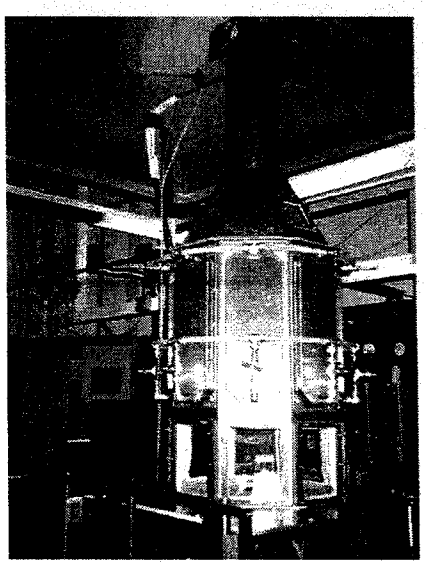

Figure 5.2: Furnace Enclosure with Water-Cooled Panels

The enclosure consists of an upper and lower panel section which can be changed to simulate different boundary conditions and allow for different viewable areas of the reaction. The upper panel section is 24 inches in length and can accommodate aluminum "blanks," optical windows, or water-cooled panels. The lower panel section is intended exclusively for optical access and consists of frames to hold the Vycor windows with a viewable area of 7.5 inches × 9.5 inches. A photograph of the furnace enclosure with water-cooled panels is presented as Figure 5.2.

The furnace enclosure is mounted on the traverse assembly, straddled between two large optical breadboards. The traverse assembly allows the translation of the burner/furnace system in any of the three coordinate axes while keeping the optics fixed on the stationary optical tables. A diagram of the furnace and test stand are shown in Figure 5.3 with one of the two laser anemometry systems used. The test stand and enclosure design are discussed in detail in Miyasato (1993) and Brouwer (1996).

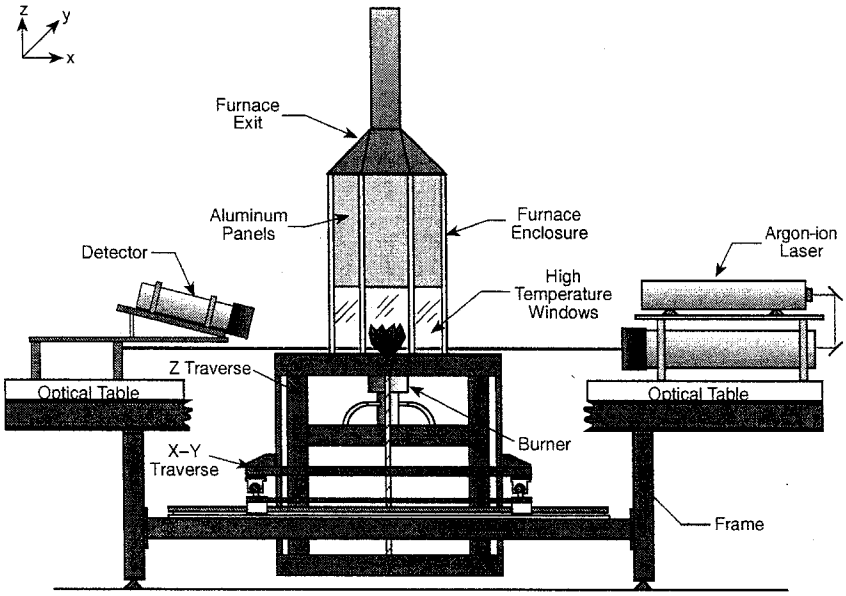

Figure 5.3: Test Stand Traverse with Furnace Enclosure

The axial air, swirl air, and natural gas flows are computer controlled using mass flow controllers. Each of the flow rates are redundantly metered by rotometers and can be manually set using metering valves. The manual flow delivery system and computer controlled mass flow controllers are discussed in detail in Miyasato (1993) and St. John (1994), respectively.

5.1.2. Generic Burner (100,000 Btu/hr)

The model industrial, natural gas fired burner ("generic burner") was designed with input from several major burner manufacturers, several combustion consultants, and the IFRF. The intent of this burner design was to maintain key characteristics of industrial burners while allowing experimental flexibility. This small, model burner served as the testbed for the mechanistic studies, from which the results were then applied to the other burner systems.

The burner, shown in Figure 5.4, is up-fired at a constant heat rate of 100,000 Btu/hr. The burner consists of four major elements: entry plenum, swirler, contraction, and quarl. The entry plenum is comprised of a 0.5 inch diameter central natural gas fuel tube and a 1 inch combustion air annulus. Swirl is introduced into the air annulus via an axial stream and a tangential, or swirl, air stream. With this arrangement, the swirl intensity can be varied by changing the ratio of swirl air to axial air.

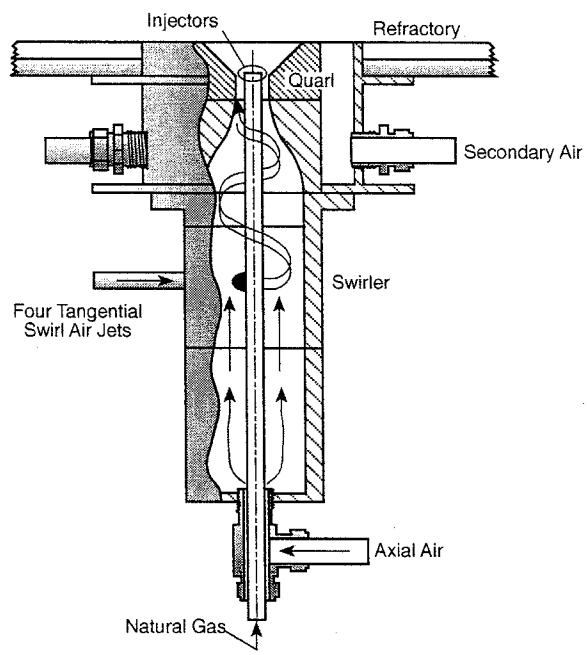

Figure 5.4: Model Industrial Burner

The swirling air is introduced in a clockwise direction (looking down on the burner), with the swirl intensity, S', represented as the square of the swirl air flow divided by the total air flow:

$$S' = \left(\frac{m_\phi}{m_a + m_\phi} \right)^2 \tag{5.1}$$

This definition is similar to the geometric swirl number defined as (Feikema, Chen, and Driscoll, 1990):

$$S_g = \frac{\pi \cdot r_o \cdot d_a}{2A_t} \left(\frac{m_\phi}{m_a + m_\phi} \right)^2 \tag{5.2}$$

where

r_o = radius to tangential swirl inlet

d_a = throat diameter

A_t = total area of tangential swirl inlets

m_a = axial air mass flow rate

m_ϕ = tangential air mass flow rate

As such, S' can be converted to the geometric swirl number by multiplying by a constant geometric factor, which is 3 for this burner.

The air flow contracts to a 1 inch diameter at the burner throat before expanding in the 45° half-angle quarl. The quarl expansion is 1 inch long and is flush with the furnace enclosure floor.

The fuel flow rate was set to provide a constant heat release rate of 100,000 Btu/hr, based on a heat content of 1,022 Btu/ft^3 for the natural gas. The corresponding air flow rates at 0%, 10%, and 20% excess air are provided in Table 5.1. The calculated bulk flow velocities, based on the flow rates and burner geometry, are also listed to illustrate the operational range of the burner.

Table 5.1: Natural Gas and Air Operating Parameters

	Flow Rate		*Bulk Velocity*	
	ft^3/min	*m^3/s (·10^4)*	*ft/s*	*m/s*
Natural Gas	1.6	7.7	378	115
0% Excess Air	15.7	74.1	64	20
10% Excess Air	17.2	81.2	70	21
20% Excess Air	18.8	88.7	77	23

The fuel injectors, shown in Figure 5.5, are 0.50 inches in diameter with six 0.0469 inch diameter jets located 0.25 in upstream of the injector tip. Earlier work in this burner by Miyasato (1993) identified that low NO_x and high combustion efficiency could be attained at certain conditions by introducing the fuel radially into the swirling annular air. As such, the radial fuel injection strategy became the baseline for this research. Building on this concept, two other radial mixing strategies were employed by varying the fuel jet injection geometry: in the same direction as the swirling air stream ("co-swirl") and in a direction opposing the swirling air stream ("counter-swirl"). Since the co-swirl injector delivers fuel in the same direction as the swirling air, mixing occurs via shear due to the velocity difference between the jets and the air stream. For the radial injector, mixing is mostly due to the vortical mixing caused by the cross-flow. And since the counter-swirl injector opposes the swirling air, mixing via a jet injected into a cross-flow takes place. Hence the co-swirl, radial, and counter-swirl injectors represent, in simplified yet descriptive models, turbulent jet, jet in a cross-flow, and opposed jet type mixing scenarios, respectively.

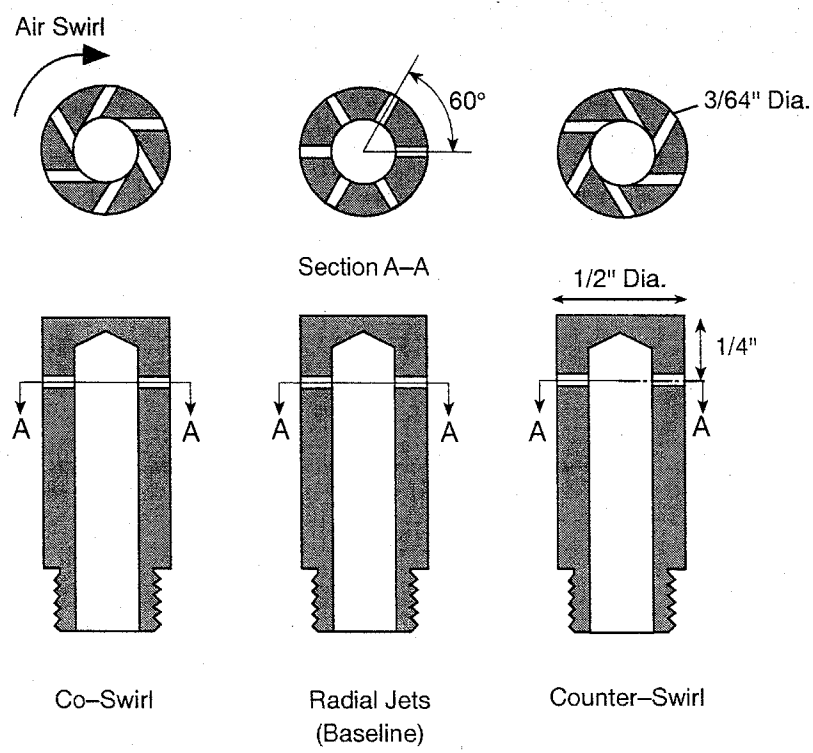

Figure 5.5: Fuel Injectors

5.1.3. Industrial Boiler Burner

Tests were also conducted on a scaled model (400,000 Btu/hr) of a production Coen burner called the Quantum Low NO_x, or *QLN*. The goal of the design was to build a burner similar to the large scale model in most aspects, but amenable to geometric variation and compatible with the existent research facility. The burner is shown schematically in Figure 5.6, with a 6.5 inch diameter and 14.5 inches in total length. The windbox consists of a 4.0 inch outside diameter pipe extrusion at its base. The total combustion air enters the windbox horizontally, transitions upward, passes through the distribution plate, and finally enters the primary reaction zone. The midsection of the windbox contains a honeycomb flow straightener to uniformly distribute the air and to ensure a vertically directed flow. Following the straightener, the air completes its flow through the windbox section by passing around the radial fuel injectors, where reactant mixing first begins, and passing through the slots of the distribution plate. As a visualization aid, the windbox section of this burner is also designed with a Plexiglass section at its bottom to allow viewing of the primary reaction zone from the base of the burner.

The distribution plate has two primary purposes. Its first function is to increase mixing between the air and the fuel from the radial fuel injectors. Its second function is to serve as a creator of recirculation. The sudden expansion exit plane from the slots to the throat produces recirculation zones which aid in stabilizing the entire flame of the burner. The slots are located at four locations around the circumference of the burner, directly above the four radial fuel injectors. The width of each slot is 0.5 inches and its length is 1.5 inches. These values were chosen to produce a velocity of 80 ft/sec of the reactants passing through the slots at an operating condition of 25% excess air. After exiting the distribution plate, the reactants pass through the throat region of the burner. For geometric variation purposes, the throat length of the subject burner is variable from 1.125 to 1.500 inches by utilizing mechanical spacers. This will later be referred to as the geometrical parameter "throat depth."

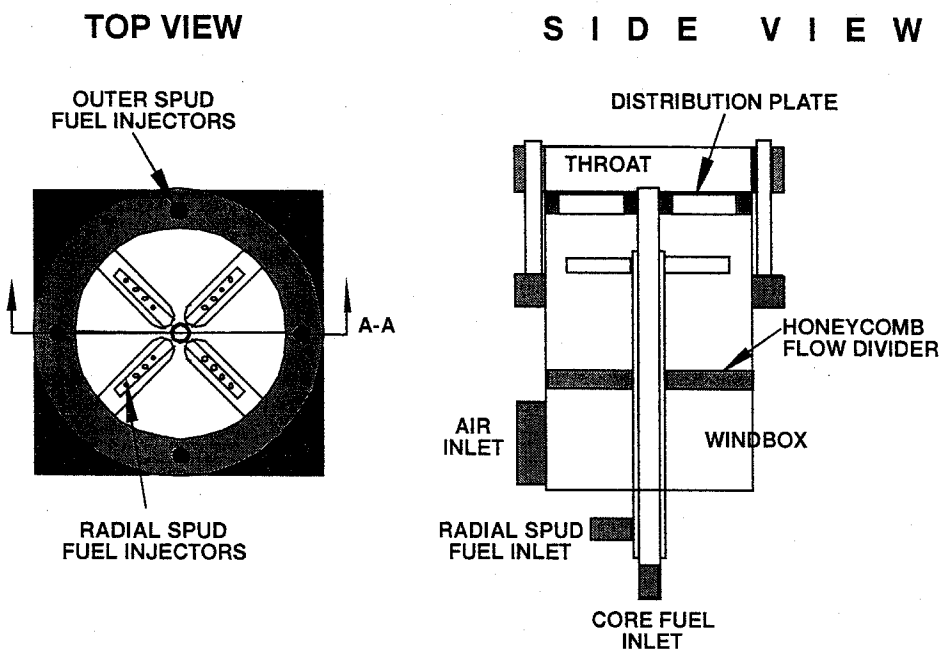

Figure 5.6: Scaled *QLN* Burner
(Coen Company, Inc.)

The design of the subject burner is fuel staged. The flow of natural gas is monitored and controlled through three different sections of the burner. The radial fuel injectors serve as one of these three fuel flows. The radial injectors are located beneath the distribution plate, within the upper section of the windbox. When looking from the exhaust section, down into the burner, the radial injectors can be seen through the distribution plate slots as shown in the top view of the burner schematic. There are four injectors placed symmetrically around the burner centerline. These four injectors are supplied with natural gas from a header located at the center of the burner. Each of these injectors has four evenly spaced, 0.12 inch diameter holes along its length which inject fuel axially upward through the distribution plate slots. The radial injectors can be moved up and down vertically as a single unit. This permits changing the distance between the radial injectors and the distribution plate. This will later be referred to as the geometrical parameter "radial depth."

The outer fuel injectors are the second location of fuel injection and are the secondary fuel components of the fuel staged burner. Four 0.5 inch diameter injectors are located in a circular array about the burner throat. Each of the four injectors has two holes which are slightly angled inward toward the burner centerline. Each of these injectors can be moved up and down vertically and can also be turned in either direction to possibly aim the injector holes away from the burner centerline. These two geometrical parameters will later be referred to as "outer depth" and "outer direction," respectively.

Finally, natural gas is injected through a 0.25 inch diameter tube in the center of the burner to provide pilot flame, termed the core fuel. The gas is radially injected over the centerline of each of the four slots in the distribution plate. The fuel injector has four 0.005 inch diameter holes at each 90 degree location around the circumference of the tube. The four holes are positioned 0.125 inches above the exit plane of the distribution plate. The primary purpose of this injector is to produce a locally rich flame to ignite the

reactants passing through the distribution plate slots. This core fuel produces a central pilot flame which outputs 25% (100,000 Btu/hr) of the total heat load.

5.2. High Temperature Furnace

The high temperature furnace facility was constructed during the CIEE program to provide an industrial scale test stand capable of firing at 4 MMBtu/hr for the testing of high heat rate applications, such as metal processing and VOC oxidation. Full detail on the furnace design process, construction, and initial shakedown can be found in Weakley (1997).

The simulator is 16 feet long and 16 feet from the floor to the top of the stacks, with an internal volume of 8 feet square by 10 feet long. The external dimensions of the furnace simulator box are 12 feet long by 10 feet square. The maximum allowable internal service temperature is 2400° F, the maximum design burner load is 4 MMBtu/hr, and the maximum allowable internal pressure is 0.5 inches H_2O. The simulator walls and ceiling are insulated with 12 inch square blocks of 10 lb/ft^3 ceramic fiber modules. The stacks contain 9 inch thick modules. The ceramic modules have a peak exposure temperature of 2600° F. The floor is a layered construction of 2000° F insulating fire brick 4 1/2 inches thick underneath an 8 inch layer of castable refractory (for greater wear resistance). The castable is RefLite 30-90, which is a alumina-silica base with a maximum service temperature of 3000° F.

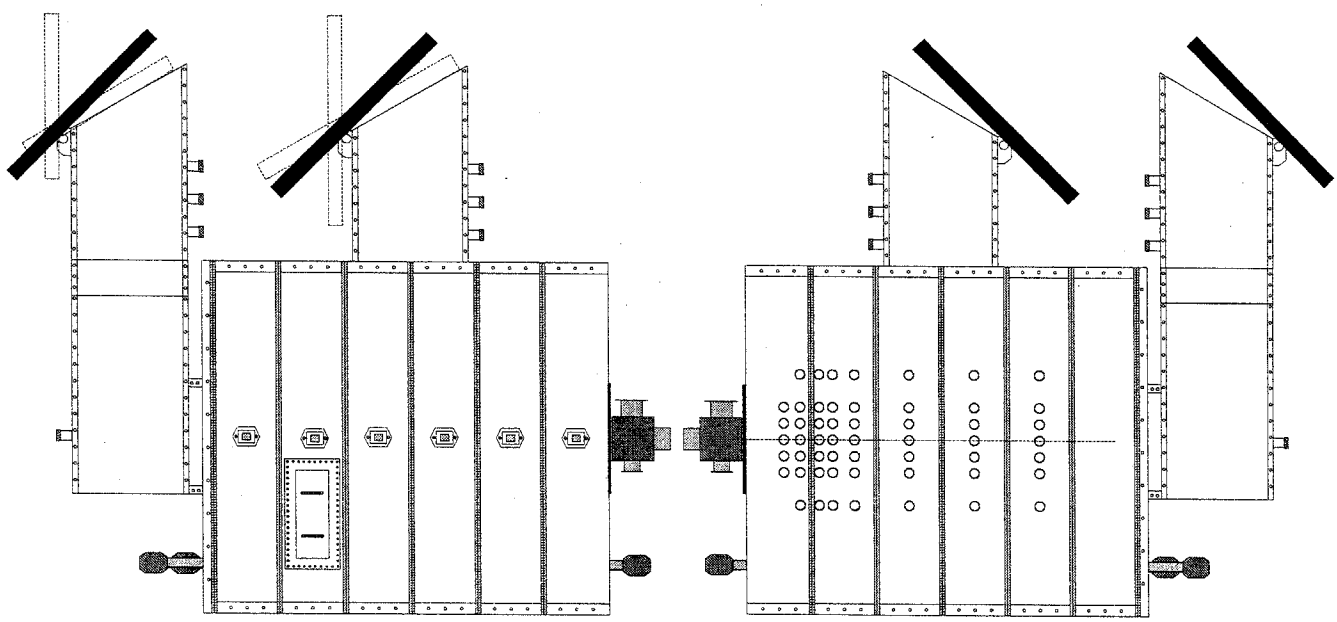

Figure 5.7 Furnace Side Views

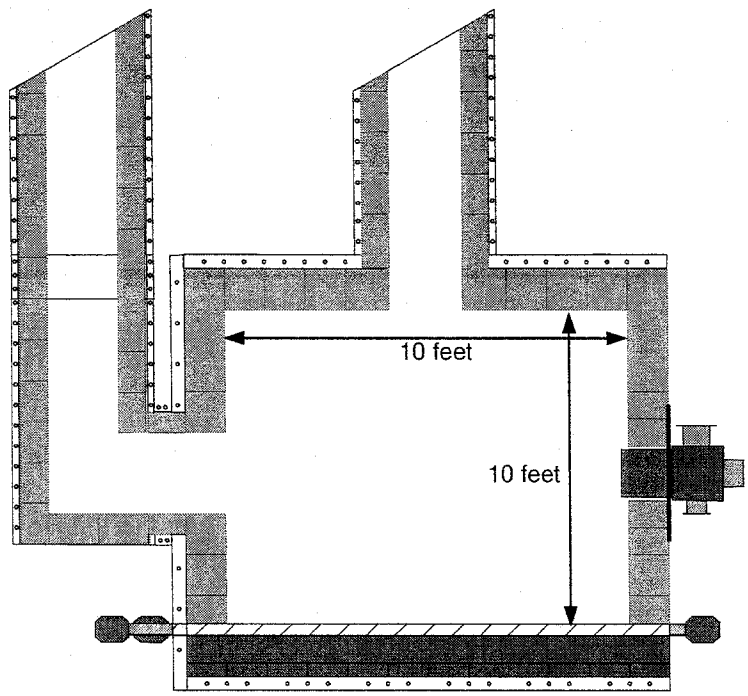

Figure 5.8 Cut-away View of Simulator

The furnace is equipped with two emission stacks which are used individually - one at the rear to simulate continuous industrial processes and to provide uniform, homogeneous boundary conditions for verifying CFD simulations, and one in the center to simulate batch-type industrial processes. Each exhaust stack has a 38 inch by 38 inch opening, is insulated with 9 inch thick ceramic fiber modules, and has three 3 inch sampling ports for obtaining bulk emissions samples. At the top of each flue is a ceramic fiber-lined mechanical damper for sealing off the flue not being used and controlling the internal furnace pressure on the flue being used.

The furnace also has an internal cooling system consisting of 25-2 inch schedule 40 carbon steel pipes which run along the furnace bottom from front to back. These pipes are arranged in five banks of five pipes each with a square plate-steel header at either end. The pipes lay on top of the cast refractory floor of the simulator and cover approximately 60% of the floor area. This cooling system allows three different furnace floor temperature levels to be set. A very low temperature environment (approximately 1300° F exhaust temperature) can be set by operating with the bare pipes. A high temperature environment can be achieved (approximately 2400° F exhaust temperature) by placing 2 inch thick blankets of 8 lb/ft^3 'Durablanket 2600' ceramic fiber over the cooling pipes. This achieves a basically adiabatic condition. An intermediate thermal environment (approximately 2000° F exhaust temperature) can be achieved by placing 1/2 inch thick blankets of 4 lb/ft^3 ceramic fiber blankets. This cuts off direct radiative heat transfer from the hot gases to the pipes but allows convective/conductive heat transfer to continue. Fine control of the internal thermal environment can be achieved by adjusting the cooling water flowrate and temperature to the pipes, although this must be done with caution to avoid pipe overheating.

Visual access into the furnace is provided via seven standard industrial viewports arranged on one side at the furnace centerline and one at the front and back. The viewports are North American SAF-T-EYE No. 11 double-shutter air cooled viewport. They are arranged along the wall to allow observation at fixed points downstream of the main reaction. Although these are not of laser quality, the viewports provide access for visual inspection.

The furnace air system consists of a blower, piping, a flowmeter, and control valve. The piping consists of sections of 6 inch schedule 40 carbon-steel piping which are joined by flanges. The final connection from the piping to the burners is made with a 6 inch length of wire-reinforced polyethylene HVAC hose. The fuel system consists of a pipe train, flame safety panel and associated instruments, flowmeter, and valve. Natural gas is supplied to the system by a commercial 2 inch-50 psig line supplied by Southern California Gas Company.

The simulator is extensively instrumented at multiple locations. Thermocouples are located in the exhaust gas exit stream in both flues, and are embedded in the inside refractory wall and attached to the exterior surface at one location on the ceiling. Together with the extensive thermocouple instrumentation of the furnace cooling system already discussed, these allow calculation of wall and stack losses as well as thermal load heat extraction, so that a complete heat balance can be performed on the simulator. The furnace is also equipped with a interior pressure tap, which consists of a stainless-steel tube through the furnace wall, connected to a copper tube leading to the Dwyer pressure gage on the control panel.

All inlet flowrates of air, gas, and water into the furnace are carefully metered. In addition, a small amount of cooling air must be supplied to the furnace viewports and the burner flame supervisor. This flow (approximately 15 scfm under normal conditions) is also measured by a Dwyer rotometer. Finally, the moisture content of the main combustion air is monitored by a Vaisala model HMP-233 hygrometer. This unit uses a bi-metallic element as the humidity sensing head, and measures relative humidity and dry-bulb temperature. A hygrometer is not as accurate as a chilled-mirror unit, but is less expensive, requires less maintenance, and gives continuous readings. The sensing head is placed in the main air line, while the reading is taken at the main control panel.

5.2.1. High Temperature Industrial Burner

The high temperature burner used for these studies, the *Kinedizer*, is a variation on a commercially available burner manufactured by Maxon Corporation. The geometrically simple burner is shown in Figure 5.9. Air flows through the swirl vanes and around the "goose-neck" fuel delivery pipe. The injector is located within the constricted region of the flow. The fuel and air mix and proceed downstream to the burner throat. The throat opens to a refractory quarl, which expands at an acute 6° half-angle. The simplicity of design is typical of high temperature or process heater-type industrial burners.

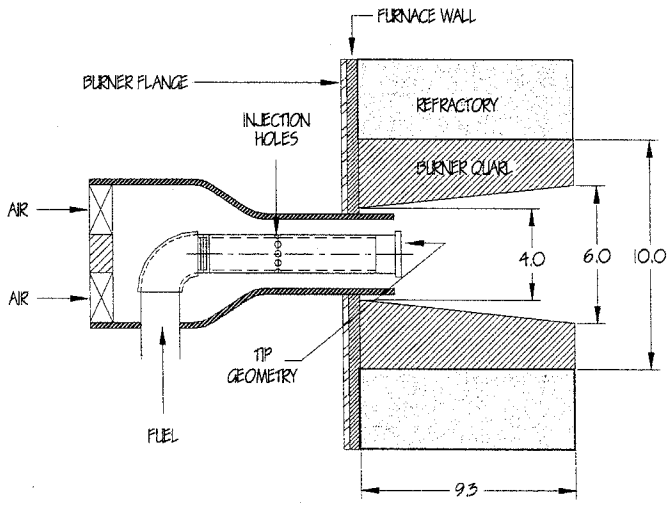

Figure 5.9: Maxon *Kinedizer*

5.3. *Diagnostics*

The diagnostic ensemble applied to these applications can be divided into two main categories: conventional and advanced. The conventional diagnostics are typically intrusive whereas the advanced diagnostics are laser-based and non-intrusive.

5.3.1. Conventional

The conventional diagnostics include extractive emissions sampling, intrusive temperature measurement, and film photography and videography. Although the last two diagnostics, photography and videography, are optical and non-intrusive, they are included as conventional diagnostics due to their long tradition as imaging techniques.

Emissions Analyzers

The extractive emissions analyzers measure carbon monoxide (CO), carbon dioxide (CO_2), hydrocarbons (HC), oxygen (O_2), and nitrogen oxides (NO_x). The instruments are part of an integrated sampling and computer data acquisition system. The CO and CO_2 analyzers (Horiba model AIA–220) utilize the non-dispersive infrared technique which is based on infrared absorption proportional to the concentration of the species in the sample gas. The hydrocarbon analyzer is a flame ionization detector which detects the concentration of ionized carbon atoms in the sample by flowing the sample through an internal hydrogen flame. The hydrocarbon analyzer is packaged with a paramagnetic oxygen analyzer (Horiba model FIA/PMA–220) which measures the concentration of oxygen by applying a magnetic field to the sample and measuring the pressure difference caused by the build-up of oxygen molecules near the cathode. The NO_x analyzer (Horiba model CLA–220) utilizes the chemiluminescence technique which reacts any NO in the sample with ozone to form an excited NO_2 molecule, which in turn releases a photon to return to the ground state. The photons are measured by a photomultiplier tube to provide a linear relationship of photons to NO in the sample. These types of analyzers are commonly used for emission gas sampling; a more detailed summary of these measurement methods can be found in Miyasato (1993) or in the individual analyzer manuals.

For global emissions measurements, stack exhaust gases are sampled using water-cooled, 0.5 inch diameter, stainless steel probes. The water in the probes is heated to 125°F to protect the probe and quench the sample to prevent further reaction while avoiding condensation of water vapor inside the probe. The emissions are pumped through a Teflon line heated to 275°F to prevent water condensation, and the sample is then split into two streams. The NO_x stream goes through a converter to reduce any NO_2 in the sample to NO prior to the refrigeration unit. This is done to preserve the NO_x concentration since NO_2 is soluble in water and could be lost in the water drop-out if conversion is not performed. A schematic of the emissions sampling system is shown in Figure 5.10.

For in-flame emissions measurements conducted in the optical furnace, a smaller, 0.25 inch diameter water-cooled, stainless steel sampling probe is used. This probe is inserted through an upper panel in the furnace to allow spatial measurement of the reaction. The probe is attached to the same heated line and sampling system shown in Figure 5.10.

All of the emissions measurements from the analyzers are recorded using a digital data acquisition system. The measurements from the analyzers are sampled over a 20 second period at a rate of 5 Hz. One hundred samples for each analyzer are averaged and recorded in a data file on the computer as well as redundantly recorded manually in a lab notebook.

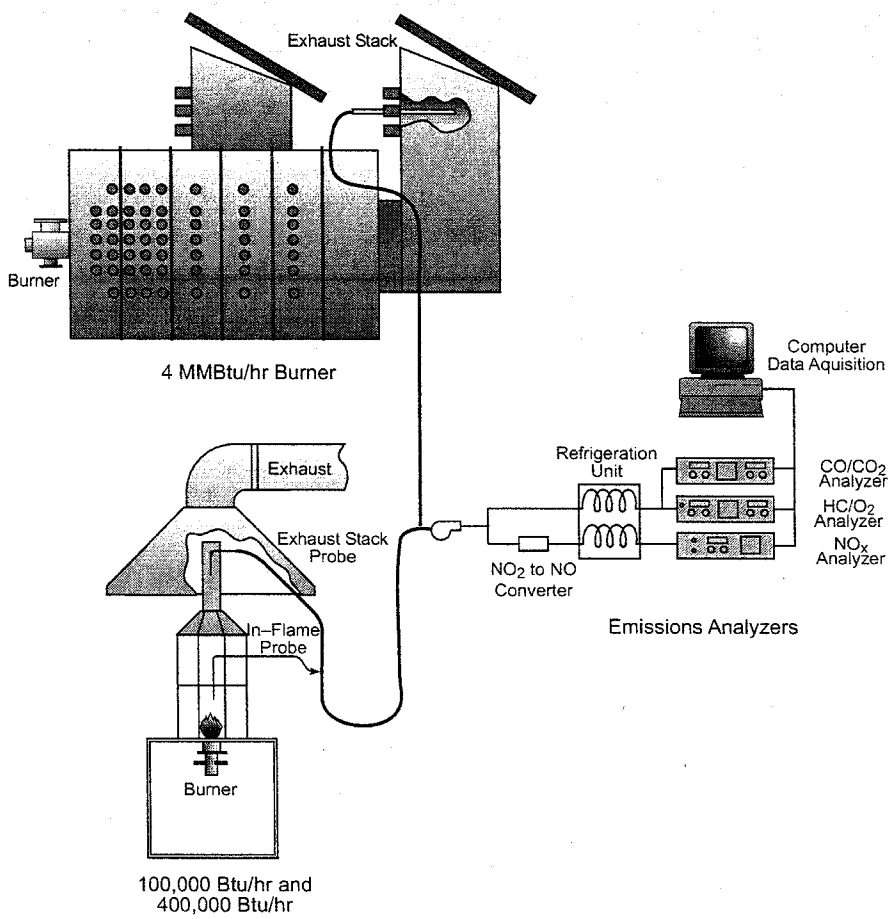

Figure 5.10: Emissions Sampling Train

The analyzers, water-cooled probes, and heated sample line setup are in general agreement with the guidelines set forth in Title 40 of the Code of Federal Regulations Part 60 (40 CFR 60), Appendix A, Methods 7E and 10 for NO_x and CO measurement, respectively. All of the reported emissions have been corrected to 3% O_2, unless stated otherwise, in accordance with industrial burner convention and 40 CFR 60 Appendix A, Method 21.

Thermocouples

Both facilities are outfitted with numerous Inconel-sheathed, type "K" thermocouples for monitoring the furnace temperature at various locations, the probe cooling water inlet and outlet, and the furnace cooling water inlet and outlet. These temperatures are also sampled in the data acquisition system to provide 100 count averages.

Point measurements of in-flame temperatures in the optical furnace are conducted using a 0.0625 inch diameter Inconel-sheathed, type "B" thermocouple. The thermocouple is inserted into the water-cooled, in-flame probe described in the previous section to preserve the thermocouple's integrity during sampling and reduce the movement of the probe due to aerodynamic and thermal effects. The temperature measurements are again input into the digital data acquisition system to produce 100 count averages of the temperature. A further correction is applied to account for radiation losses as outlined in Holman (1984), where an energy balance between the convective and radiative heat transfer is conducted on the thermocouple tip to calculate the true gas temperature.

Photography and Videography

A conventional 35 mm, single lens reflex camera (Minolta X-700) was used for capturing the time averaged reaction images from the generic and *QLN* burners. For the high temperature burner, video images were captured from the viewing port closest to the burner exit using an RCA video camera. For the in-furnace video in the optical furnace, a Toshiba IK–M41A, 0.5 inch diameter CCD color camera ("lipstick" camera) was used. The Toshiba camera was protected from excessive temperatures using an air-cooled copper jacket with a heat mirror (see Figure 5.11). Both video cameras were input to a Sony SVO–2000 video cassette recorder to capture the reaction. The images were then digitized from the video tape for inclusion into this report.

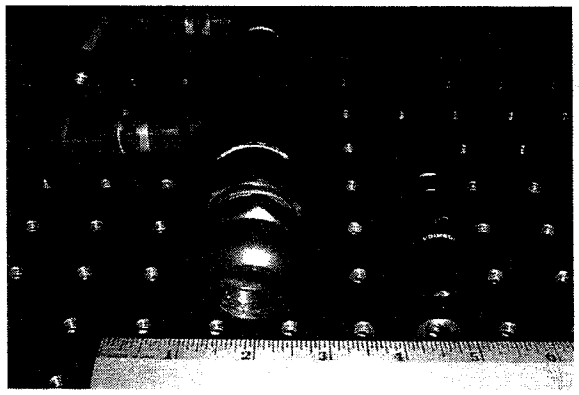

Figure 5.11: In-Furnace Video Camera and Air-Cooled Jacket

5.3.2. Advanced Optical (Non-Intrusive)

The non-intrusive, optical diagnostic measurements were conducted almost exclusively on the generic burner as this hardware was designed to investigate the pollution mechanisms by providing flexible, controllable, and simple parameters with relatively easy access to the reaction. Laser anemometry for velocity measurements, however, were also conducted on the *QLN* (in the optical furnace) and on the high temperature burner. The following provides a general description of the optical techniques applied.

LIF

Laser induced fluorescence (LIF) is a technique by which the relative concentration of a species can be measured. The laser wavelength is tuned to an energy transition of the species of interest. Some of the incident laser photons are absorbed, causing the molecule to excite to a higher energy state. Some of these higher energy molecules spontaneously emit a photon, i.e., "fluoresce", producing the LIF signal. This signal is then collected and imaged on to an intensified detector, with the collected intensity proportional to the concentration of the species in the probe volume. If the excitation laser beam is spread into an optical sheet, the resulting planar laser induced fluorescence (PLIF) can be imaged onto an intensified solid-state camera to provide a two-dimensional flow-field image of the molecule of interest.

The wavelength of the fluorescence is dependent on the molecule and the selected laser-stimulated resonance. The three species measured in these experiments were NO, OH, and acetone (CH_3–CO–CH_3). The NO and OH were products of the combustion reaction, while acetone was doped into the fuel flow to provide non-reacting fuel distribution images. The NO measurements were pointwise whereas the OH and acetone measurements were planar.

One of the major difficulties in LIF is obtaining the required wavelength resonant with the optical transition. The same Spectra-Physics DCR–3 Nd:YAG laser used for the CARS measurements was used

to provide the light for these LIF measurements. The incident and fluorescence wavelengths for each of the molecules studied are shown in Table 5.2. For more information on LIF, the reader is directed to Eckbreth (1988) and Hanson, Seitzman, and Paul (1990). Further details on acetone PLIF can be found in Lozano, Yip, and Hanson (1992).

Table 5.2: Laser Induced Fluorescence Wavelengths

Specie	*Measurement*	*Excitation λ (nm)*	*Fluorescence λ (nm) (λ_{max})*
OH	planar	283–285	305–316
NO	point	226	287
CH_3–CO–CH_3 (acetone)	planar	266	350–550 (445)

Laser Anemometry

Axial and azimuthal velocities were measured using laser Doppler anemometry, which is technique based on Mie scattering of particles in the fluid flow. Laser anemometry uses the intersection of two continuous wave laser beams of the same frequency to form a probe volume. The probe volume consists of alternating lines of constructive and destructive interference from the two beams, forming an interference pattern, or "fringes," of known spacing. When a particle passes through the probe volume, Mie scattering occurs at the light fringes producing a signal proportional to the time required to cross the fringes. The speed of the particle is then calculated from the known fringe spacing and the measured time. Furthermore, if a known frequency shift is applied to the fringes, the measured signal will also provide directional information due to the relative Doppler shift. For more information regarding laser anemometry, the reader is directed to Durst, Melling, and Whitelaw (1976) and Stevenson (1979).

Since the gaseous flow does not effectively scatter light, small (nominal 1 µm diameter) alumina particles were "seeded" into the air flow to allow velocity measurements. For the velocity measurements downstream of the burner quarl, a Spectra Physics 2016–04S (4 Watt) argon-ion laser was used with an Aerometrics Phase Doppler Particle Analyzer system. Due to the large distances and the desire to measure as close to the burner exit as possible, a 1,000 mm focal length transmitting lens and 629 mm focal length receiving lens were used. A Spectra Physics 2020–05 (5 Watt) argon-ion laser and an Aerometrics Real Time Signal Analyzer system were used with the fiber-optic transceiver in the backscatter configuration with a 620 mm lens.

A summary of the diagnostics applied to the experiment is provided in Table 5.3, which lists the measured flow characteristic, the technique applied, the location(s) of the measurement, the spatial resolution of the technique (point, planar, or global), and the amount of flow disturbance resulting from the measurement (intrusive vs. non-intrusive).

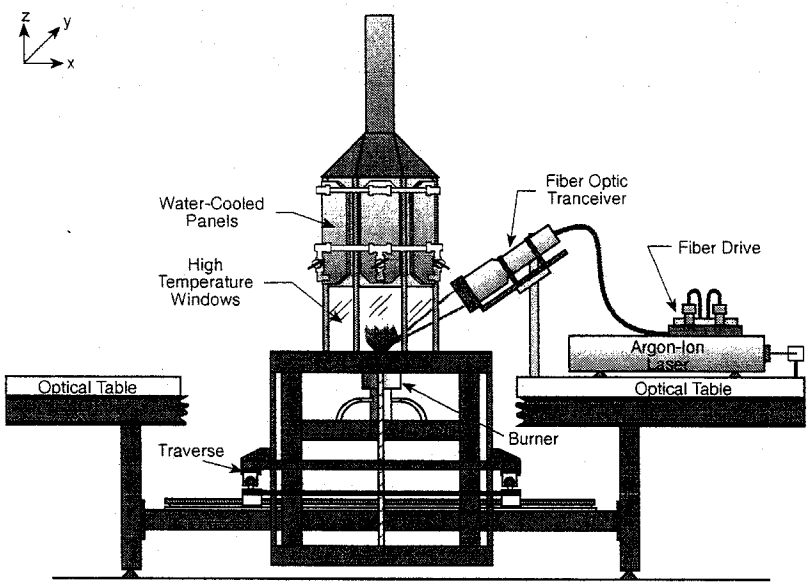

Figure 5.12: Bottom Window Backscatter Laser Anemometry Setup

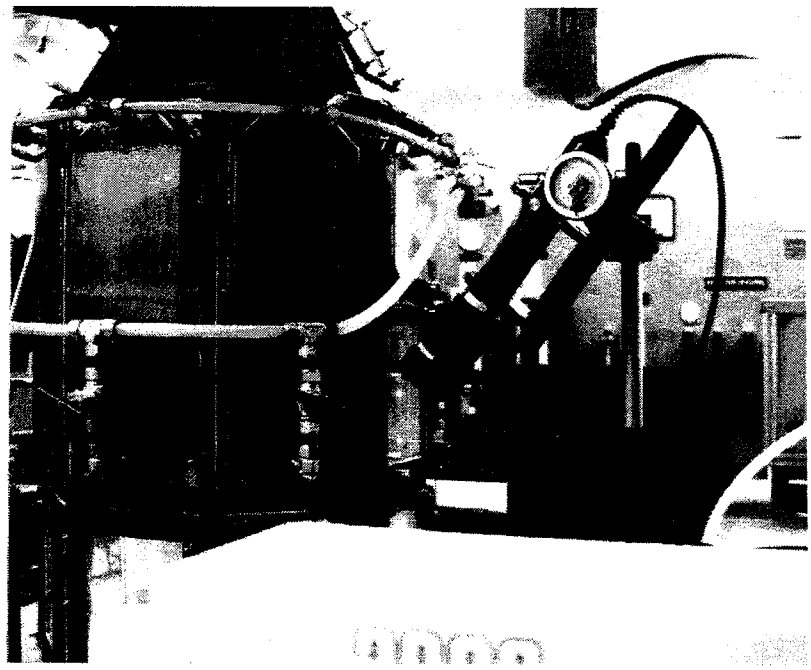

Figure 5.13: Top Window Backscatter Laser Anemometry Setup

Table 5.3: Diagnostic Techniques Applied to Experiment

Measurement	*Method*	*Location*	*Resolution*	*Perturbation*
CO, CO_2, HC, O_2, NO_x	extractive probe	stack in-flame	global point	intrusive intrusive
temperature	thermocouple	in-flame	point	intrusive
velocity	LA	in-flame throat in-quarl	point	non-intrusive
NO	LIF	in-flame	point	non-intrusive
OH	PLIF	in-flame	planar	non-intrusive
fuel distribution	acetone PLIF	throat	planar	non-intrusive
luminosity/shape	videography photography	luminous region	global	non-intrusive

5.4. Modeling

As seen in Table 5.3, a battery of extractive and non-intrusive measurements were taken at various locations within the furnace and burner itself. Despite all of these careful measurements, it is extremely difficult to access the near-field mixing region immediately downstream of the fuel jets with extractive probes or non-intrusive techniques due to the small spatial extent of the region and its location deep inside the burner. Furthermore, the actual chemical processes resulting from the mixing and aerodynamics cannot be measured in these practical systems. As a result, computer modeling was used as a tool to gain insight into the fuel and air mixing processes and pollutant emission mechanisms within the burner.

There were two types of modeling efforts conducted for the program: a time-averaged, computational fluid dynamic (CFD) model and a chemical kinetic model. The CFD modeling was done to determine flow structures and fuel injection characteristics for better mechanistic understanding in regions inaccessible to measurements. The chemical kinetic modeling was conducted to determine the best NO_x chemical mechanisms for industrial burner systems. Solution of the time-averaged modeling was conducted at UC Irvine and the chemical kinetic modeling was conducted at Lawrence Livermore National Laboratories.

5.4.1. Time Averaged CFD

The commercial CFD code *Fluent* (version 4.42) was selected due to its user-friendly graphical interface and wide acceptance in the burner industry. The near-field jet injection of the burner was modeled in three dimensions (3D) in order to capture the discrete fuel injection and swirling air flow interaction. Since the burner is axisymmetric, only a 60° sector encompassing a single fuel jet is modeled with cyclic boundary conditions at the sides of the sector. A power-law scheme is used for interpolating the computed velocity and scalar values at the grid centers to the cell boundaries. The SIMPLE (Semi Implicit Method for Pressure-Linked Equations) algorithm is used to solve the appropriate conservation

equations (Patankar, 1980). The model geometry is shown in Figure 5.14, rotated 90° from the actual burner hardware (this rotation was necessary in *Fluent* in order to make the horizontal axis a line of symmetry). The computational domain consists of a 26 × 16 × 30 grid (12,480 cells).

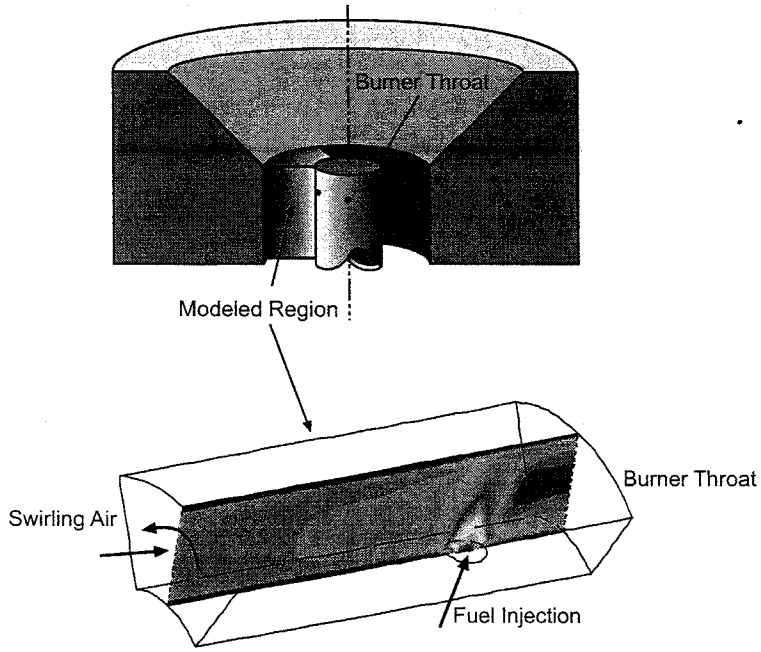

Figure 5.14: Near-Field Injection Model

Since the highest air velocities occur at the burner throat, the model assumes that (1) no negative axial velocities exist in this region and (2) the reaction initiates downstream of this region. As a result, the simpler k–ε turbulence model and non-reacting conditions are applied, which allow the calculations to converge more quickly.

5.4.2. Chemical Kinetics

The chemical kinetic modeling was conducted by Lawrence Livermore National Laboratories (LLNL) using the Hydrodynamics, Chemistry, and Transport (HTC) code. The need for kinetic (time dependent chemistry) models is necessary since equilibrium, steady state, or time averaged models cannot account for time dependent chemistry such as NO_x or air toxics formation. The software code is capable of modeling in detail one-dimensional time-dependent combustion phenomena of gases. The physical processes that are modeled are chemical reactions, thermal conduction, species diffusion, and hydrodynamics.

Models to describe combustion chemistry in practical combustion systems are constructed in a hierarchical manner. This is natural since reaction mechanisms for larger hydrocarbon fuels are built upon mechanisms for smaller fuels. The simplest fuels are hydrogen and carbon monoxide, and the next more complex fuels are methane and methanol. The next level consists of species with two carbon atoms, including ethane, ethene and acetylene, along with ethanol. Reaction mechanisms can be constructed for fuels with virtually any number of atoms, and current models routinely treat fuels with as many as 7 – 8 carbon atoms (i.e., heptane or octane fuels).

As a hydrocarbon fuel is consumed, it is taken apart by chemical reactions into smaller fragments, leading eventually to water and carbon dioxide. A reaction mechanism consists of all of the elementary chemical reactions that can occur with the given fuel and all of the intermediate species that can be produced during

its systematic conversion to final products. Each reaction has a temperature-dependent rate, and each chemical species has a heat of formation and other associated thermodynamic parameters. The mechanism is then used to formulate differential equations for concentrations of each chemical species which are then integrated in time to describe the combustion of the fuel, its accompanying release of chemical energy and resulting heating, and the rate of product formation. If combustion is not complete, the mechanism will predict the composition of the combustion products. Some of the products of incomplete combustion consist of chemical species which are covered by the Clean Air Act Amendments and other environmental regulations. Examples of such pollutant species that are produced during natural gas combustion include formaldehyde (CH_2O), acetaldehyde (CH_3CHO), carbon monoxide (CO), methanol (CH_3OH), 1,3-butadiene (C_4H_6) and many others.

The simulation used for these studies incorporates a steady flow reactor with sufficient heat transfer to keep the chemical contents at a constant temperature. This type of model allows specification of characteristic time scales and investigation of the residence time affect on the reaction evolution.

6. TASK 1 – TECHNOLOGY DEVELOPMENT AND SUPPORT RESEARCH

The work conducted under Task 1 was focused on gaining the requisite experience and understanding of representative industrial burner flowfields through measurements and modeling. In order to accomplish this task, the generic model burner was utilized due to its ready optical access, flexible and straightforward design, and large amount of previous measurements.

6.1. Generic Burner Exhaust Measurements: Screening Studies

Stack emissions measurements were taken over the entire stability limits of all three (co-swirl, radial, and counter-swirl) fuel injectors to determine if any of these mixing strategies led to reduced NO_x and CO emissions. The NO_x and CO emissions for each injector over their entire operational range are shown in Figure 6.1, with the NO_x emissions plots shown on the left and the CO emissions on the right. The horizontal axis of each plot is the input swirl intensity, S', and the vertical axis is the percent excess air.

The co-swirl injector displays low NO_x emissions over its entire operating range (represented by the blue color), but also has high CO emissions in these same regions (represented by the red color). In contrast, the counter-swirl injector has low CO emissions over most of its operating range but higher NO_x. For all three injectors, the lowest NO_X emissions are located near the high excess air stability limits, which also coincide with the regions of high CO. In order to more clearly illustrate this trade-off, the NO_x emissions for each injector are plotted against the CO emissions in Figure 6.1.

In Figure 6.2, the CO and NO_x emissions are plotted along the x and y axes, respectively. The NO_x vs. CO trade-off is evident for all three injectors to varying degrees; the co-swirl injector exhibits the greatest increase in CO emissions as NO_x is decreased and the counter-swirl injector displays the least sensitivity to CO emissions as NO_x is decreased. The radial injector has a trade-off which falls between these two extremes. Although this compromise between NO_x and CO emissions is well documented in the literature (e.g., A-Shaikhly *et al.*, 1992; Maughan *et al.*, 1992) the counter-swirl injector displays points with both low NO_x *and* low CO levels, identifying this injector as the superior performer. It is not possible from this figure, however, to determine the conditions at which this performance occurs.

Both Figure 6.1 and Figure 6.2 provide valuable information regarding the overall NO_x and CO concentrations as well as the emissions trade-off that occurs for each injector. These, plots, however, cannot conveniently identify conditions where low NO_x *and* low CO occur nor is it possible to quantitatively compare conditions in terms of NO_x *and* CO for the same injector or between injectors. This difficulty arises because the two variables of interest are plotted separately. To quantify and compare the NO_x–CO trade-off, the performance index is introduced.

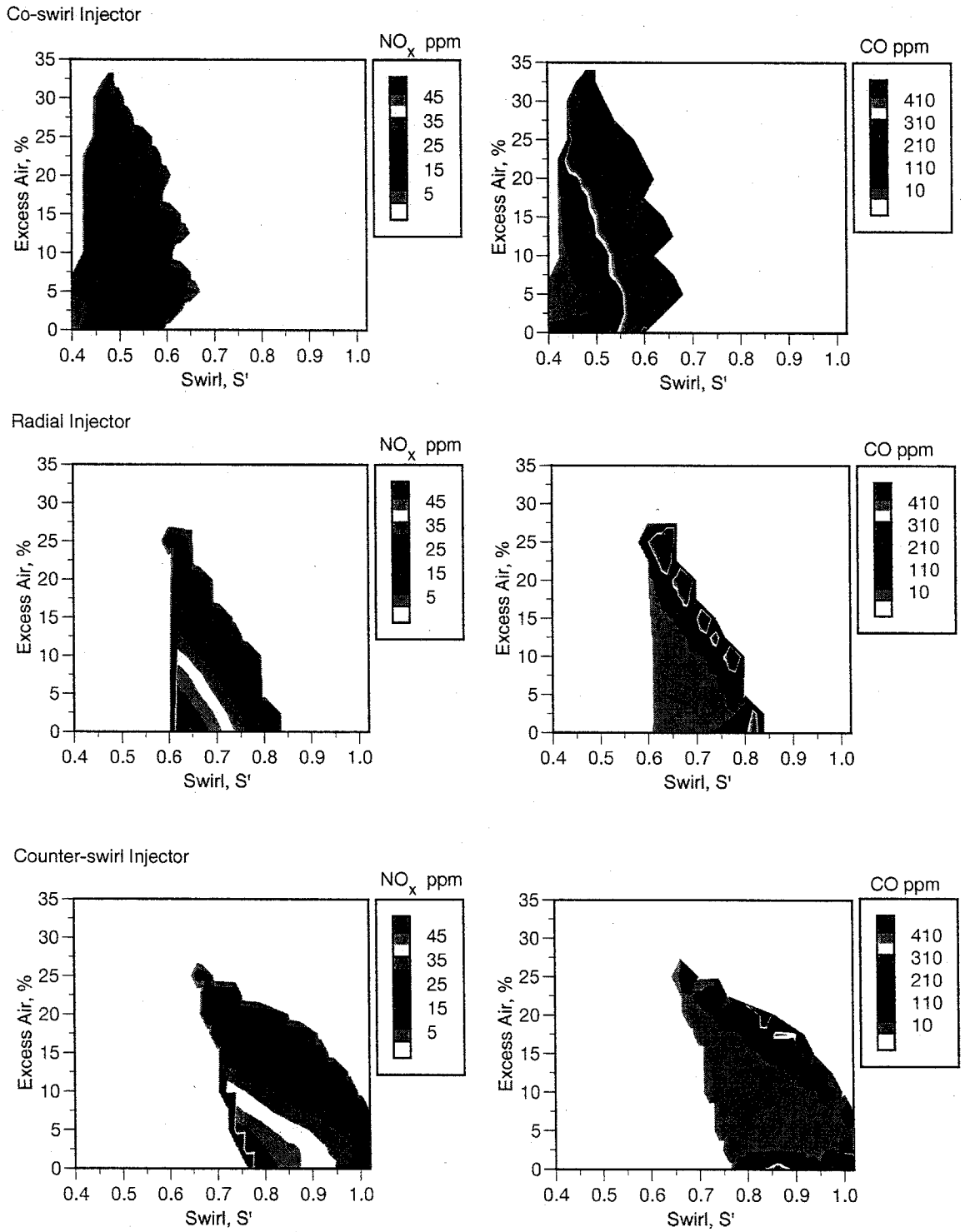

Figure 6.1: NO_x and CO Emissions (corrected to 3% O_2)

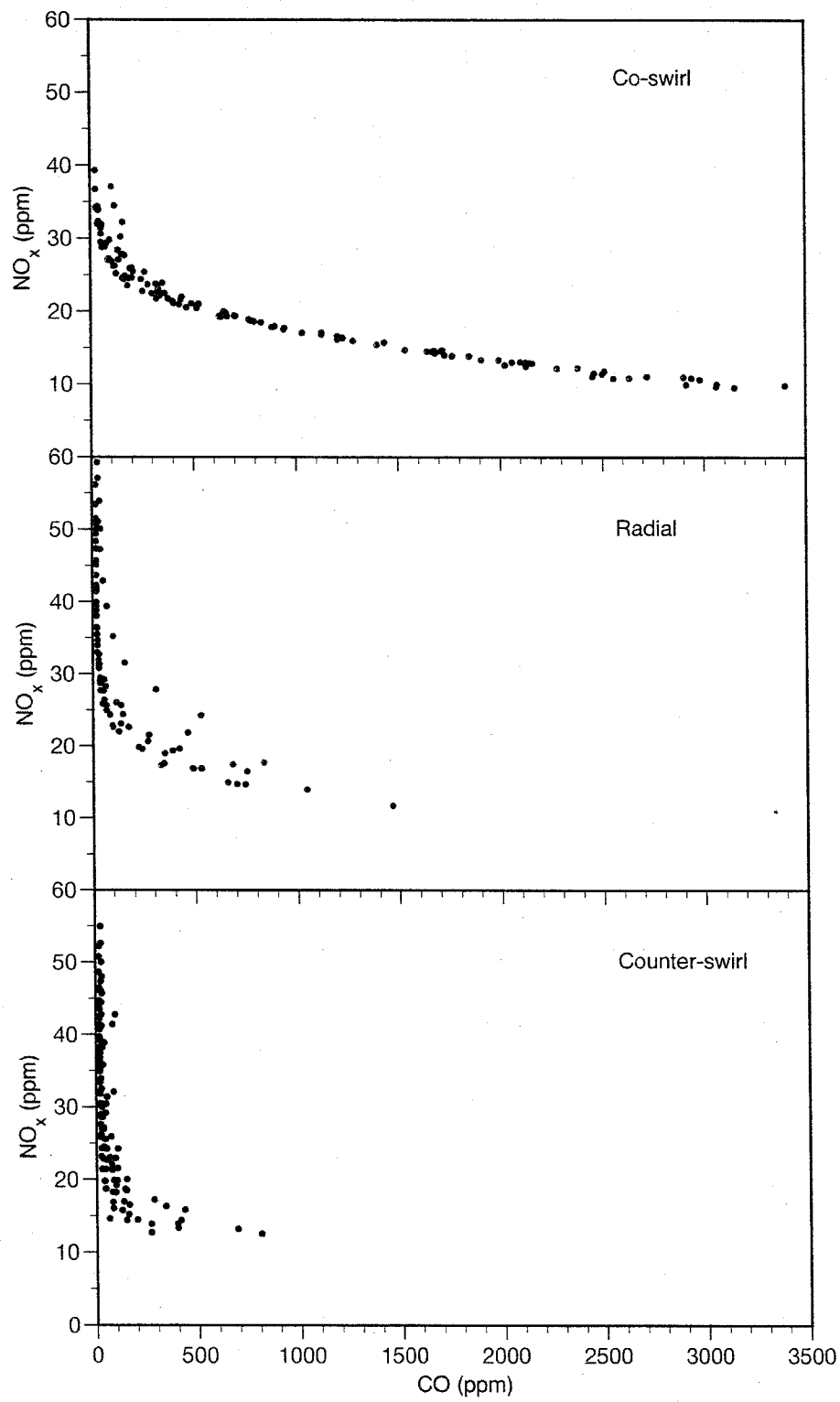

Figure 6.2: NO_x vs. CO Emissions Trade-off

6.1.1. Performance Index

In order to optimize a single variable, labeled *performance*, a cost function is introduced which incorporates both NO_x and combustion efficiency, η. The combustion efficiency was selected instead of CO because it incorporates both CO and unburned hydrocarbons thereby representing a more conservative measure. The performance function, J, is defined as

$$J = w_{NO_x} \cdot f([NO_x]) + w_\eta \cdot g(\eta) \tag{6.1}$$

The functions f and g are selected to give a maximum J value when combustion efficiency is high and NO_x is low. The terms w_{NOx} and w_η are weighting factors whose sum is equal to 1. For the results presented here, NO_x and efficiency were equally weighted at 0.5. The NO_x and efficiency functions are defined as follows,

$$f([NO_x]) = \begin{cases} 1 - 0.75 \cdot \left(\dfrac{[NO_x]}{25}\right)^4 & [NO_x] \leq 25 \text{ ppm} \\ (1-0.75) \cdot \dfrac{[NO_x]_{\max} - [NO_x]}{[NO_x]_{\max} - 25} & [NO_x] > 25 \text{ ppm} \end{cases} \tag{6.2}$$

$$g(\eta) = \begin{cases} 0 & \eta < 99.8\% \\ \left[\dfrac{\eta - \eta_{\min}}{100\% - \eta_{\min}}\right]^{1/2} & \eta \geq 99.8\% \end{cases} \tag{6.3}$$

Both of these functions vary from 0 to 1, with high values indicating low NO_x and high efficiency. For NO_x concentrations greater than 25 ppm, a linear contribution to f is provided that can be no greater than 25%. Once NO_x is below 25 ppm, a steep, fourth order slope contributes to f. The $[NO_x]_{\max}$ term is the maximum measured NO_x for all three injectors (61 ppm). The efficiency function, g, is zero when the efficiency is below 99.8%. Once the combustion efficiency is higher than this cutoff, g is the difference between the measured efficiency and the efficiency cutoff (99.8%) normalized by the maximum difference in efficiencies. This function is parabolic to provide a steep slope and large contribution to J at higher efficiencies. The NO_x and efficiency cutoffs are derived from South Coast Air Quality Management District Rule 1146, "Emissions of Oxides of Nitrogen from Industrial, Institutional, and Commercial Boilers, Steam Generators, and Process Heaters" (SCAQMD, 1988). The functions of f and g are shown in Figure 6.3.

It should be noted that although the specific equations for the performance are somewhat arbitrary, the shapes of the functions represent the simultaneous desires to reduce two different variables by different amounts and on a different scale. Although little or no credit should be given for operation above the SCAQMD limits, a continuous *function* is required to ensure that evaluation of subsequent conditions can be quantified as "better" or "worse." As with the weighting factors for the given NO_x and CO functions, the performance function should be tailored for the region or individual burner operator's needs. Furthermore, these studies were intended to analyze and optimize the combustion process; improvements to the overall emissions levels could have been achieved by optimizing the thermal environment and chamber size, but that was outside the scope of this study.

Applying this performance function to the same emissions data shown in Figure 6.1 results in the plots shown in Figure 6.4. The resulting performance values provide a quantitative index by which different conditions can be compared. Low values of performance ($J < 0.5$) are denoted by the color range of red to green and indicate regions of high NO_x or low combustion efficiency (i.e., high CO). High performance ($J > 0.7$) regions are denoted by the blue colors and represent areas of both low NO_x and high combustion efficiency.

As suspected from the individual CO and NO_x plots in Figure 6.1 and Figure 6.2, the co-swirl injector displays the poorest performance over most of its operating range (denoted by the red color). The radial injector exhibits only slightly higher performance whereas the counter-swirl injector shows a ridge of superior performance at higher excess air values (denoted by the blue colors).

The identification of this high performance region for the counter-swirl injector thus satisfies one of the research objectives: determine conditions with low NO_x *and* high combustion efficiency (low CO). The more significant pursuit, however, is determining the reasons for this behavior.

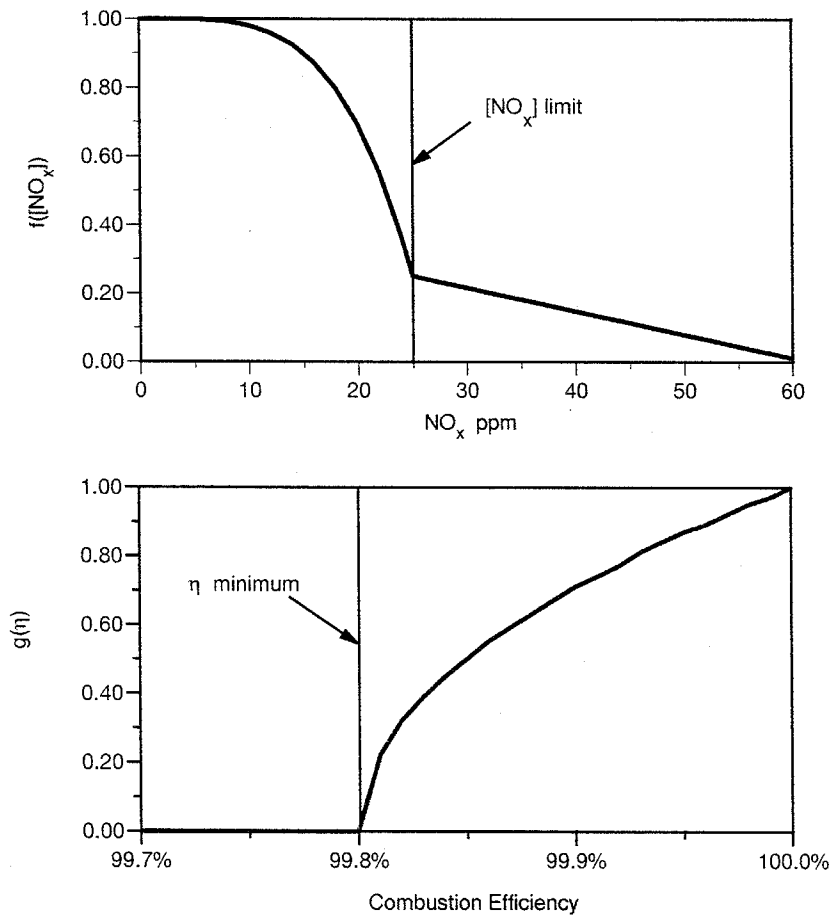

Figure 6.3: $f([NO_x])$ and $g(\eta)$ Contributions to J

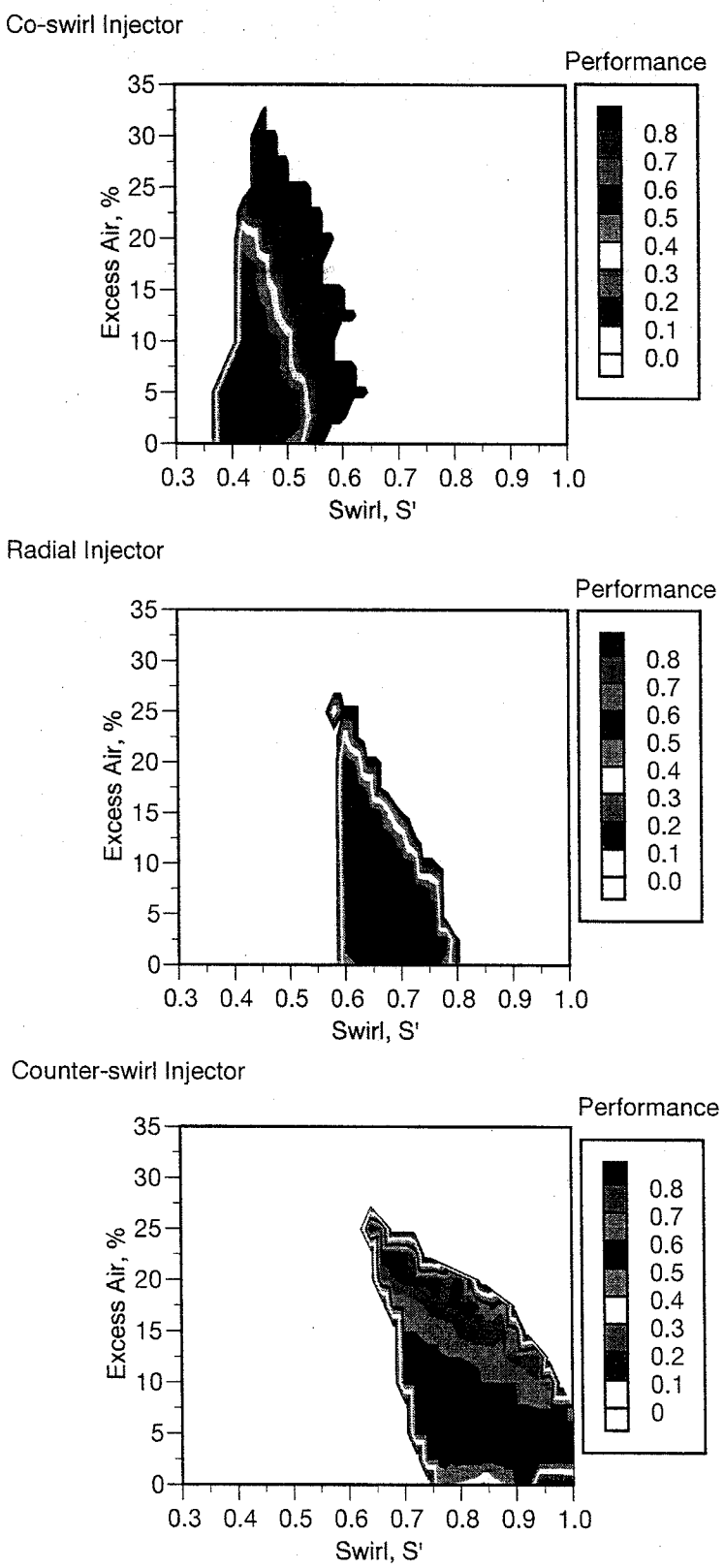

Figure 6.4: Performance Indices

6.1.2. Emissions Analysis

The discrete fuel injection geometry clearly has a large effect on the performance; however, excess air and swirl input also effect the emissions and hence the performance. In order to investigate the reasons for this performance, NO_x and CO are plotted against swirl intensity for three excess air levels Figure 6.5 and Figure 6.6, respectively; only three excess air levels for each injector are shown for clarity, however, all other excess air levels followed similar trends. To conserve space on the plots, the counter-swirl injector is abbreviated as "cx-swirl."

Figure 6.5 shows that for a given injector, increasing swirl decreases NO_x at a similar rate over all excess air levels; this indicates that the swirling air exerts a consistent mechanism on each injector over its entire stability range. In addition, the higher excess air levels have decreased NO_x and lower values of S'. The co-swirl injector is the least affected and the counter-swirl injector is the most affected by the increase in excess air, exhibited by the large difference in NO_x at a given S'. The radial, or baseline, injector is the most affected by the increase in swirl intensity (signified by the steeper slope).

The CO emissions vs. swirl intensity, shown in Figure 6.6, reveal that the CO increases with swirl and excess air. The increase in CO with swirl, however, is much steeper than the NO_x decrease (note the logarithmic scale). It is also notable that for the counter-swirl injector, swirl does not increase CO for excess air levels below 20% excess air and swirl values less than 0.84 (the flat portion of the plot); in addition, CO emissions do not increase drastically at low swirl values as excess air is increased. As with the NO_x trends, the co-swirl injector is least affected by increasing excess air levels, while the counter-swirl injector is the most affected at high swirl values, and the radial injector exhibits the greatest sensitivity to increasing swirl levels.

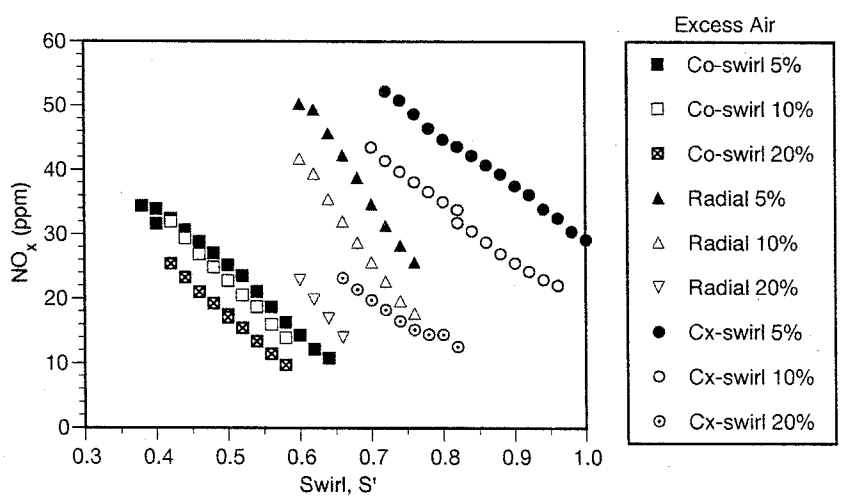

Figure 6.5: NO_x vs. S' at Various Excess Air Levels

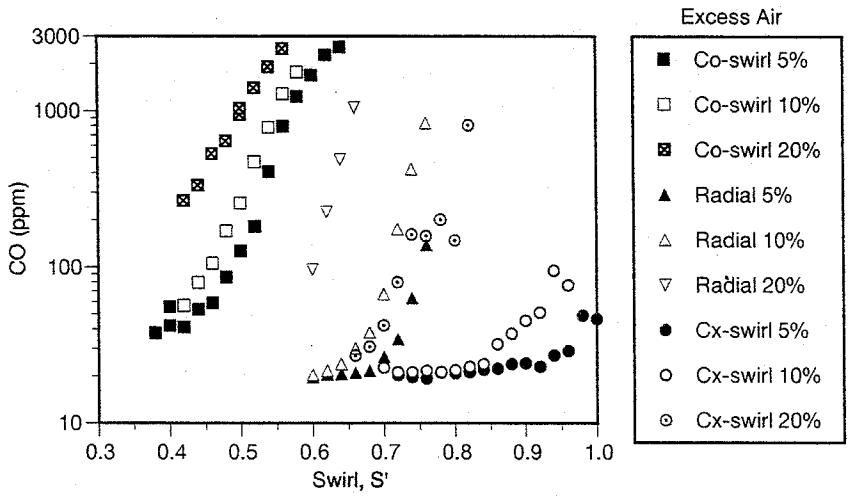

Figure 6.6: CO vs. S' at Various Excess Air Levels

The general trends are that 1) swirl decreases NO_x and increases CO for all the injectors but at different rates and 2) excess air has the greatest effect on the counter-swirl and radial injectors. The high performance exhibited by the counter-swirl injector is thus due to the maintenance of low CO with increasing swirl (up to 0.85) and excess air (up to 20%). The radial injector also exhibits low CO with increasing swirl and excess air but for only a limited range. The co-swirl injector only has low CO and low NO_x at a few low excess air and low swirl conditions.

Keeping with the hypothesis of this research, it is necessary to determine if the high performance is due to better mixing of the fuel and air prior to reaction. Premixing prior to reaction is considered to be an idealized goal for control of emissions utilizing locally lean equivalence ratios. Premixing is not used in practical systems due to the safety and cost issues associated with the possibility of flashback within the burner or delivery system. In the laboratory setting, however, it is appropriate to determine whether fully premixed performance is superior to the counter-swirl injector performance shown in Figure 6.4, or if the counter-swirl injector achieves its high performance by emulating a premixed system.

6.1.3. Premixed Comparison

The premixed condition was achieved by splitting the fuel flow into two streams and introducing the fuel into the swirl and axial air lines directly after metering. This was done far upstream of the burner such that each line had ample distance and time to become well mixed. The fuel flow to each line was controlled to give the same, overall equivalence ratio. The central fuel tube was left in the burner to provide the same annulus geometry but no flow was introduced via the injector. The resulting performance for the premixed condition is shown in Figure 6.7 in comparison to the counter-swirl injector.

These results show that the fully premixed condition yields performance inferior to the counter-swirl injector, represented by the small region of performance greater than 0.70. The poor performance is due to high CO emissions over most of the premixed stability map. These results illustrate that high performance for this burner geometry is due to an optimal fuel and air distribution which is *not* uniform.

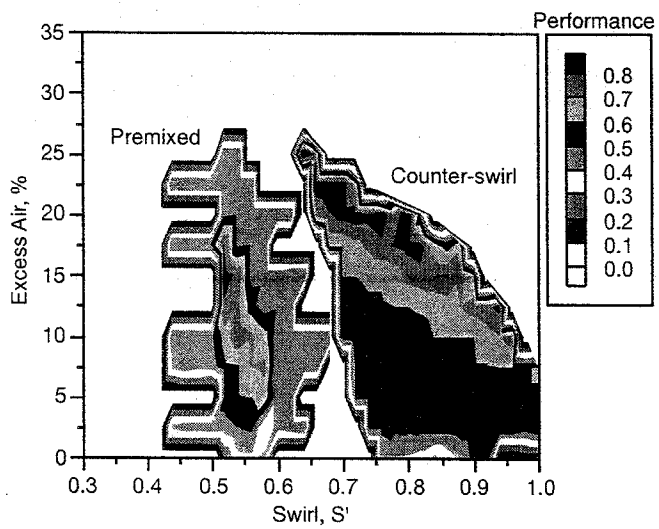

Figure 6.7: Premixed and Counter-swirl Performance

Since the premixed case is not the ultimate condition to emulate due to the reduced performance overall, attention is focused on the discrete fuel injectors. Determining the reasons for the various behavior of the co-swirl, radial, and counter-swirl injectors requires more detailed flow-field information. In order to provide this detail, the scope of the problem space was reduced to a more manageable set of conditions.

6.1.4. Selected Conditions

The performance maps for each injector were used to select conditions of varying performance to conduct detailed measurements. The conditions were selected to provide comparisons of high and low performance, high and low excess air, and high and low amounts of swirl. These conditions are shown in Figure 6.8 and listed in Table 6.1.

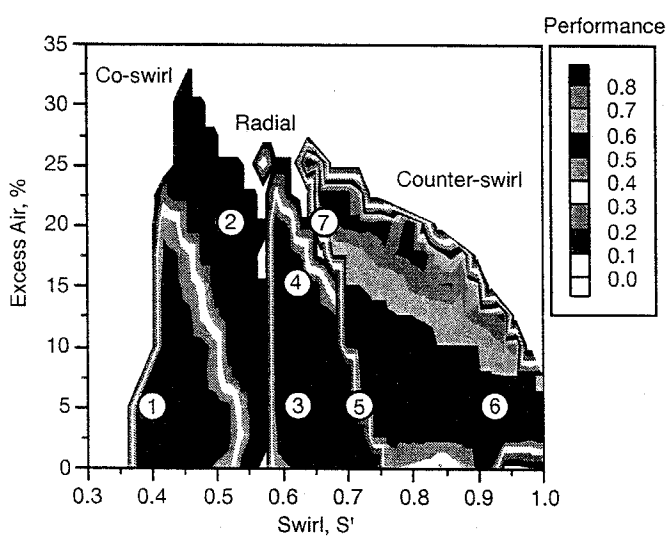

Figure 6.8: Performance Map and Selected Conditions

Table 6.1: Selected Conditions

No.	Injector	Excess Air	Swirl S'	NO_x ppm	CO ppm	Efficiency %	Performance J
①	Co-swirl	5%	0.40	32	41	99.999	0.58
②	Co-swirl	20%	0.52	15	1,397	99.212	0.45
③	Radial	5%	0.62	49	21	99.994	0.53
④	Radial	15%	0.62	28	39	99.988	0.60
⑤	Counter-swirl	5%	0.72	52	20	99.994	0.52
⑥	Counter-swirl	5%	0.92	36	23	99.993	0.58
⑦	Counter-swirl	20%	0.66	23	27	99.991	0.71

6.1.5. Exhaust Measurements Summary

Exhaust emissions for the different mixing scenarios, represented by the co-swirl, radial, and counter-swirl injectors, were measured over the entire operational space for each injector. In general, the co-swirl injector exhibits the lowest NO_x but has the highest CO. The counter-swirl injector exhibits the lowest overall CO but has high NO_x at low excess air and low swirl values. All three injectors show the typical trade-off of increased CO with decreasing NO_x, however, the counter-swirl injector displays the least CO sensitivity. In order to quantify this trade-off and compare conditions, a performance function was introduced. Using this function, the performance index, J, was calculated for each injector condition and plotted. The results reveal that the co-swirl injector displays overall low performance, due to high CO, and the counter-swirl injector displays good performance, especially along a ridge close to the high swirl stability limit.

The co-swirl injector emissions are not very sensitive to the excess air level whereas the counter-swirl injector and radial injector NO_x emissions are greatly decreased with higher excess air. Increasing swirl intensity decreases NO_x emissions for all injectors, especially the radial injector, and increases CO emission, except for the counter-swirl injector at excess air levels below 20% and swirl values less than 0.84.

In order to determine if the higher performance was due to premixed behavior, a fully premixed comparison was conducted. The emissions measurements indicate a limited region of good performance but overall *lower* performance than the counter-swirl injector.

Since fully premixed emulation was not responsible for superior performance, focus was directed at determining the causes for varied performance of the discrete injectors. Using the performance maps, seven conditions with various performance indices were selected for detailed measurements.

6.2. Detailed Measurements

The detailed measurements for all of the conditions listed in Table 6.1 are provided in Miyasato (1998). The following section condenses the findings into a comparison of three conditions, ②, ③, and ⑦. The first two conditions represent "bad" performance. The co-swirl injector at high excess air, ②, represents low NO_x but high CO. The radial injector at 5% excess air, ③, represents low CO but high NO_x. The final condition, ⑦, the counter-swirl injector at 20% excess air, represents the optimum condition. The comparison results will help to identify the flow structures and illuminate the NO_x and CO formation mechanisms. Photographs of the three conditions are presented in Figure 6.9.

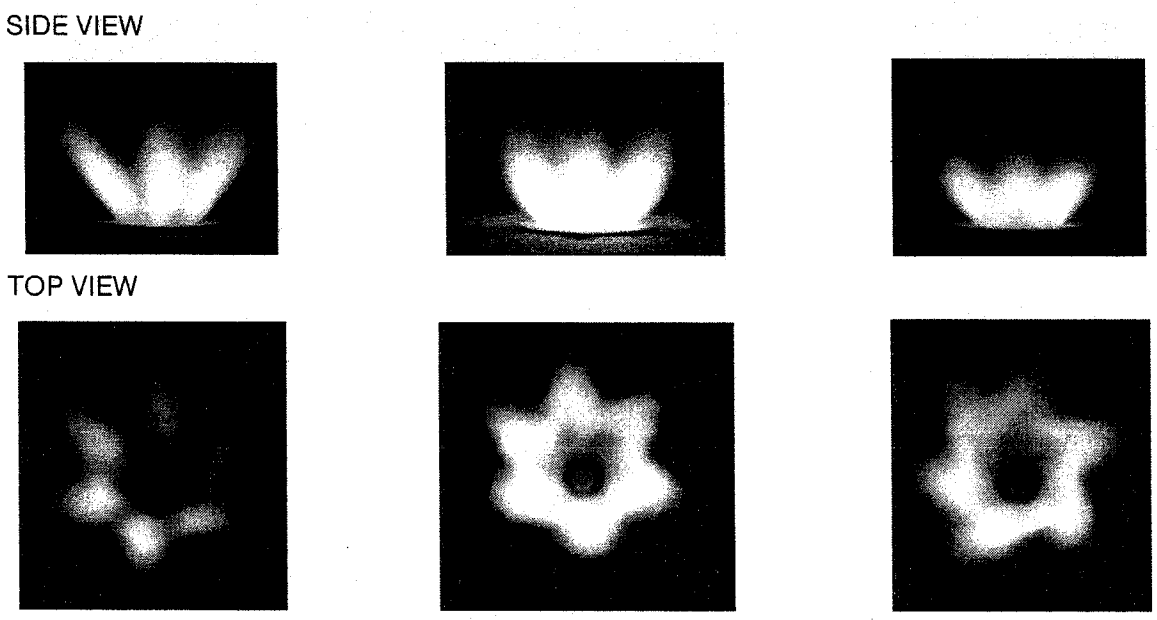

② Co-swirl Injector at 20% Excess Air, S'=0.52

③ Radial Injector at 5% Excess Air, S'=0.62

⑦ Counter-swirl Injector at 25% Excess Air, S'=0.66

Figure 6.9: Reaction Photographs

6.2.1. Burner Exit Flowfield

Measurements of the burner flowfields were taken at three axial locations downstream of the quarl exit along a complete diameter of the burner. The resulting streamlines (velocities), temperature, and NO_x concentration profiles are represented in Figure 6.10 through Figure 6.12. These overlay plots illustrate the interdependencies of the velocity, temperature, and NO_x fields.

The co-swirl injector at 20% excess air, condition ② (Figure 6.10), displays low temperatures and NO_x concentrations with the largest recirculation zone. The radial injector at 5% excess air, condition ③ (Figure 6.11), exhibits high NO_x concentration within the recirculation zone. It is notable that the high temperature contours do not coincide with the high NO_x contours, indicating that the measured NO_x has been formed upstream and convected. The high performance counter-swirl injector case at 20% excess air, ⑦ (Figure 6.12), shows a longer recirculation zone than the radial injector case at 5% excess air, lower NO_x, and lower temperatures. Due to the apparent dependency of temperature and NO_x emissions on the recirculation zone size, the recirculation zone width is plotted against the NO_x emissions in Figure 6.13 for all of the conditions listed in Table 6.1.

The results in Figure 6.13 are plotted in terms of low excess air (5%) and high excess air (15–20%) to discern any trends based on air throughput or dilution. And there is indeed a general trend with excess air as hypothesized from the pervious measurements. The cause of this decrease with recirculation zone size is attributed to the increase in internal flue gas recirculation which drives the reaction temperature down. This can also lead, however, to quenching and an increase in CO emissions and decreased performance. This is exactly what occurs for the co-swirl injector at 20% excess air (condition ②). This is illustrated in Figure 6.14 where the performance index is plotted against the recirculation zone size.

These downstream measurements identified the recirculation zone size as an important parameter in determining the performance. However, it was also discovered that the NO_x was mostly likely formed upstream and convected downstream. As such, measurements within the burner quarl were conducted.

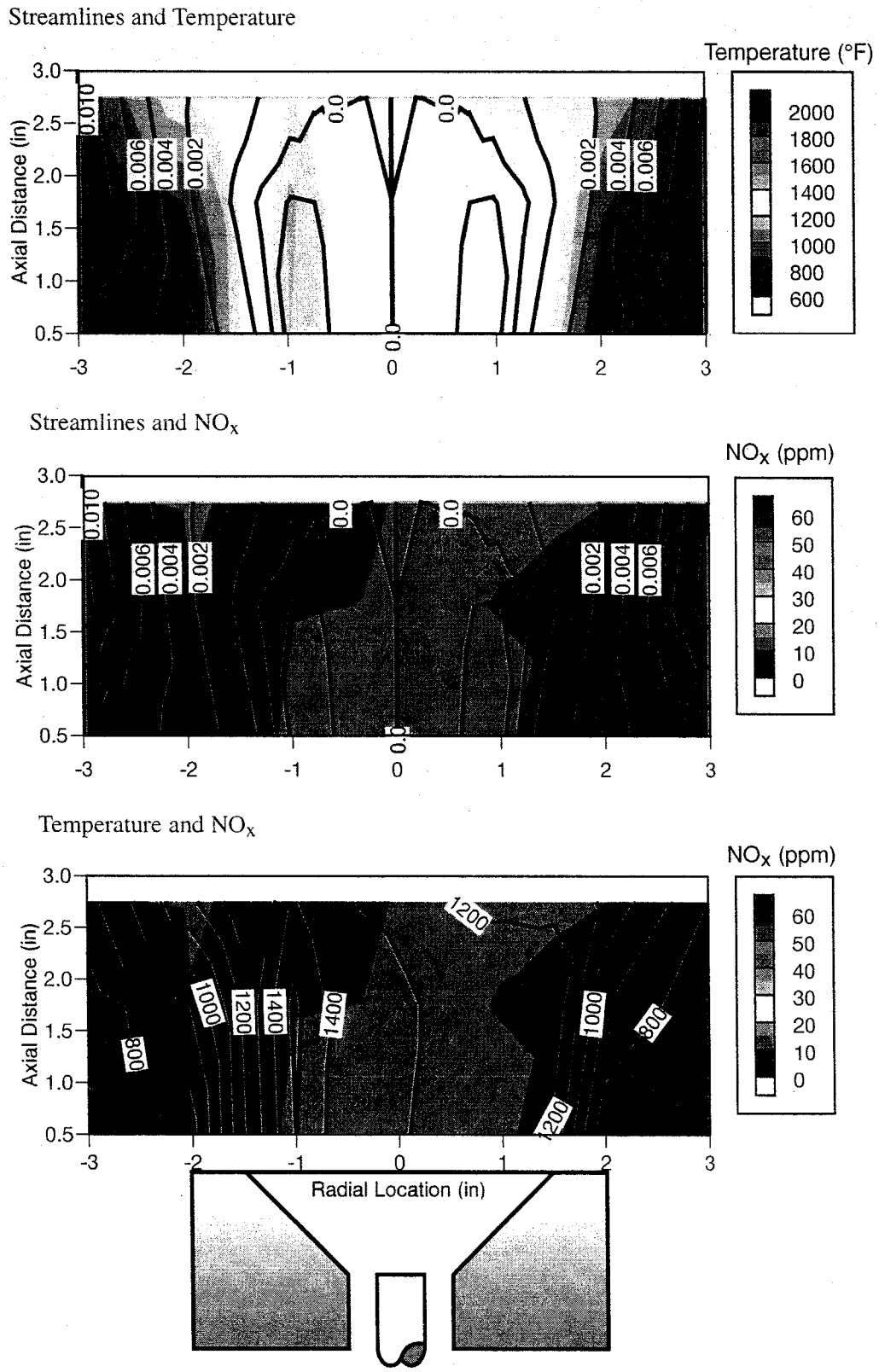

Figure 6.10: Streamlines, NO_x, and Temperature Overlays for Co-swirl Injector at 20% Excess Air, S'=0.52 ②

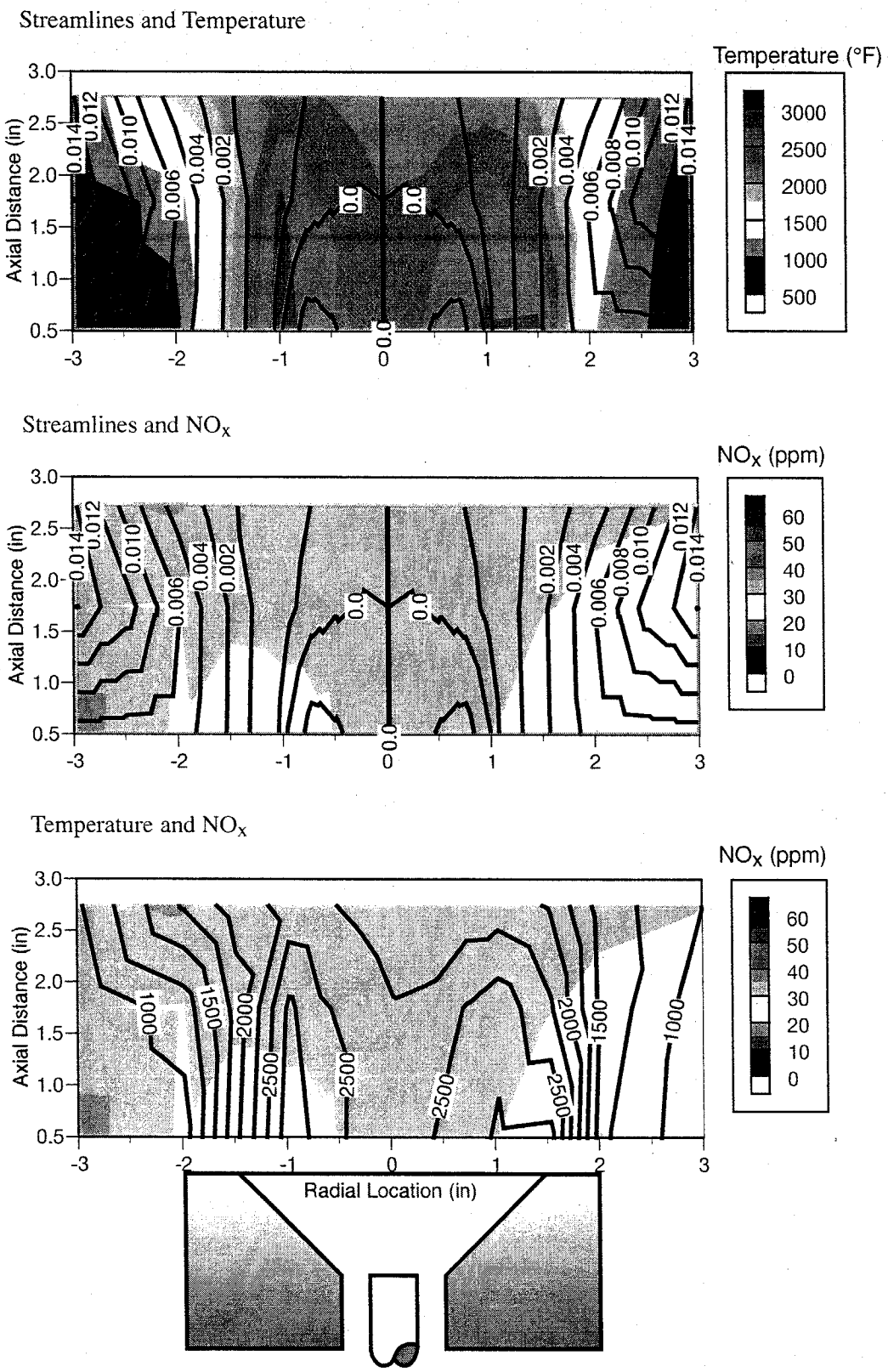

Figure 6.11: Streamlines, NO_x, and Temperature Overlays for the Radial Injector at 5% Excess Air, S'=0.62 ③

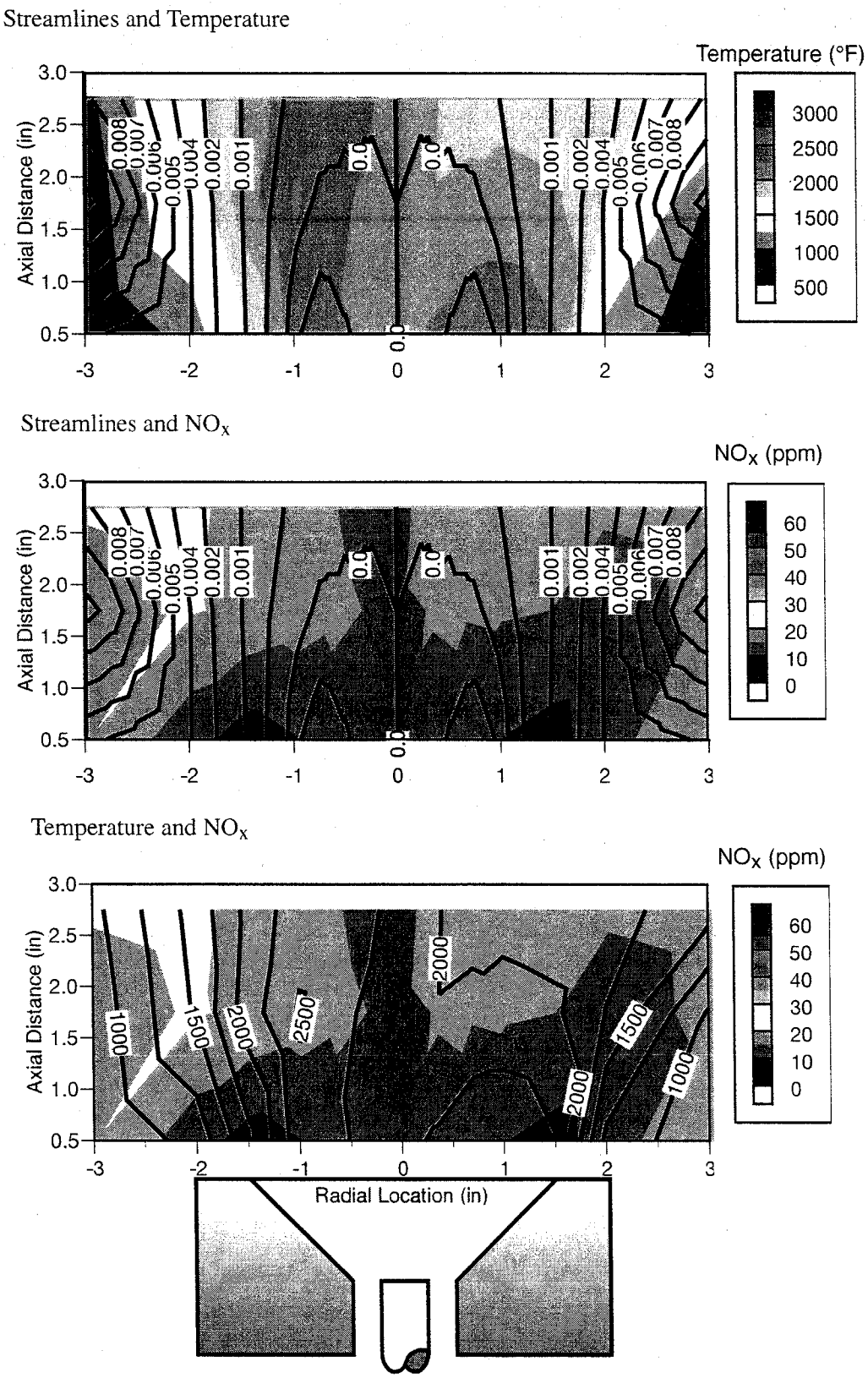

Figure 6.12: Streamlines, NO_x, and Temperature Overlays for Counter-swirl Injector at 20% Excess Air, S=0.66 ⑦

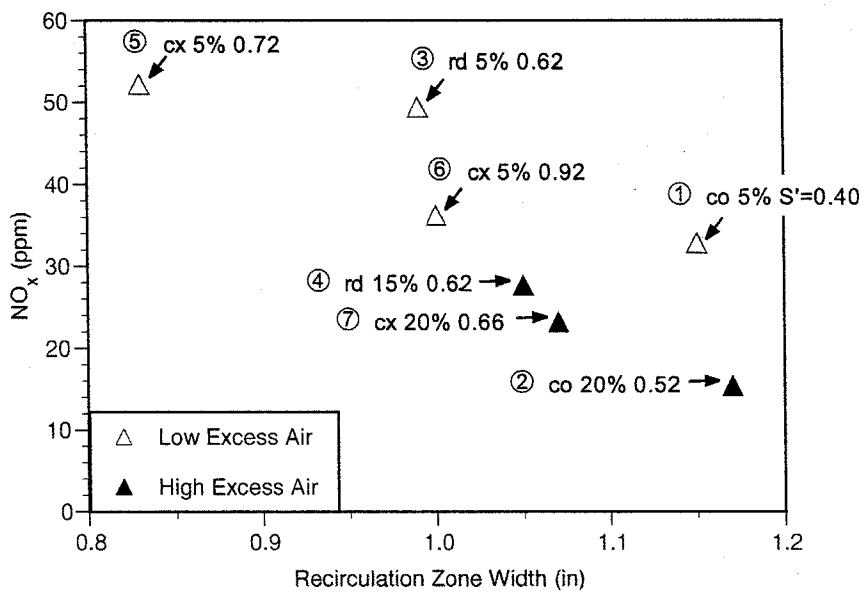

Figure 6.13: NO_x versus Recirculation Zone Size

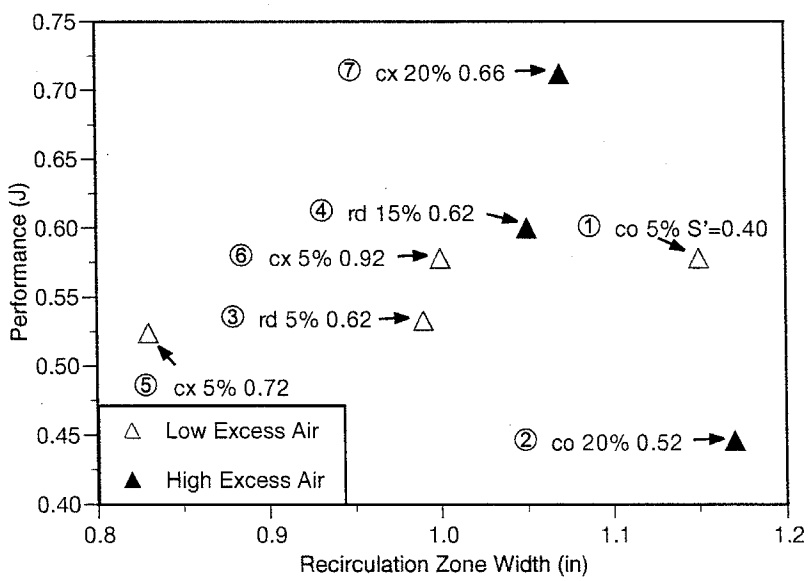

Figure 6.14: Performance versus Recirculation Zone Size

6.2.2. Burner Investigation

Reacting measurements of the emissions and temperature were taken over a one-quarter plane at the burner quarl exit and at 0.5 inches inside the quarl, as shown in Figure 6.15. The local equivalence ratios were calculated for each condition, resulting in the contour maps shown in Figure 6.16 and Figure 6.17 for z=1.0" and 0.5" respectively. The optimum perfectly premixed condition at 12.5% excess air and S'=0.52 (see Figure 6.7) contours are also shown for comparison. These contours illustrate the flow

evolution inside the quarl, with lower equivalence ratios indicating leaner mixtures and better mixing. The high equivalence ratios, signaled by the red color, indicate rich pockets where high temperatures can exist (as with the radial injector at 5% excess air, condition ③) or areas of poor fuel-air contacting with low temperatures (as with the co-swirl injector at 20% excess air, condition ②). In order to quantify these comparisons, histograms were plotted for the equivalence ratios shown in Figure 6.18 at the quarl exit (z=1.0 inch). These plots show that the co-swirl injector has the largest range and standard deviation due to poor mixing. The radial injector and counter-swirl injector have similar standard deviations, indicating fairly good mixing; however since the counter-swirl injector is at a leaner excess air level (20% vs. 5%), the temperature and NO_x values are lower giving rise to higher performance. For the perfectly premixed case, a slight standard deviation is still present, which illustrates the nominal "spread" for this system.

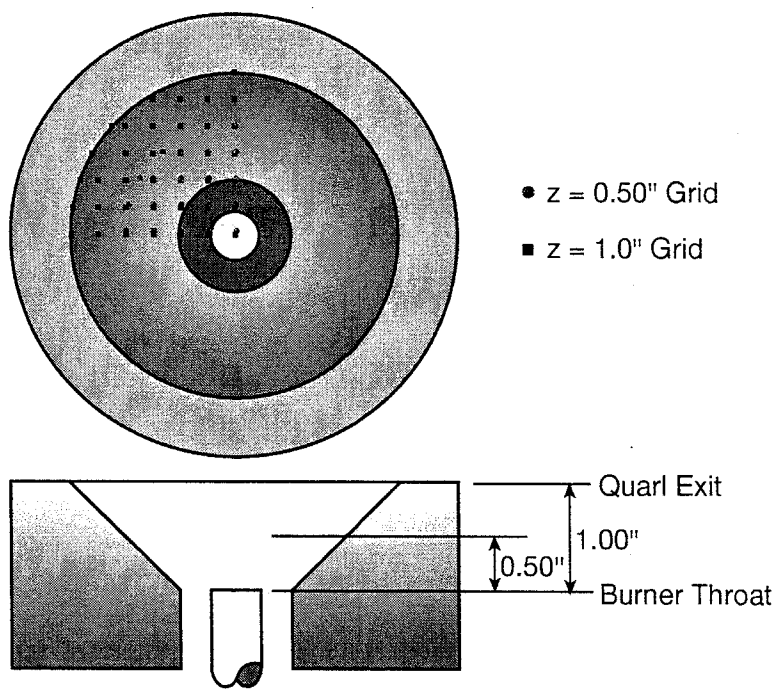

Figure 6.15: In-Quarl Sampling Grid

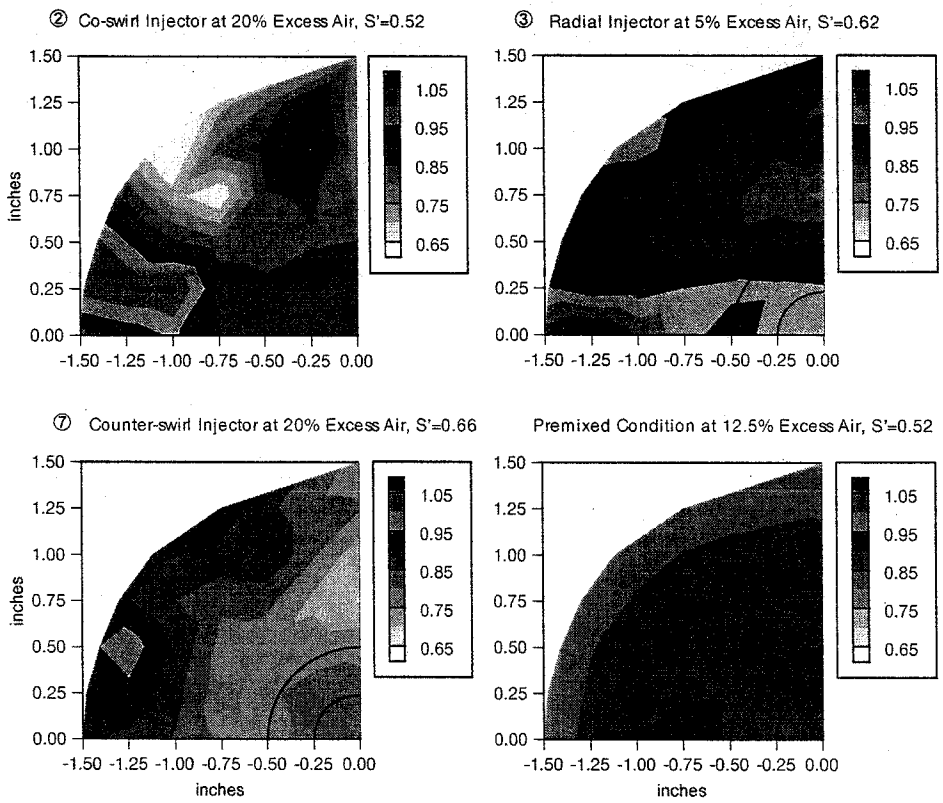

Figure 6.16: Local Equivalence Ratios at Quarl Exit (z=1.0 inch)

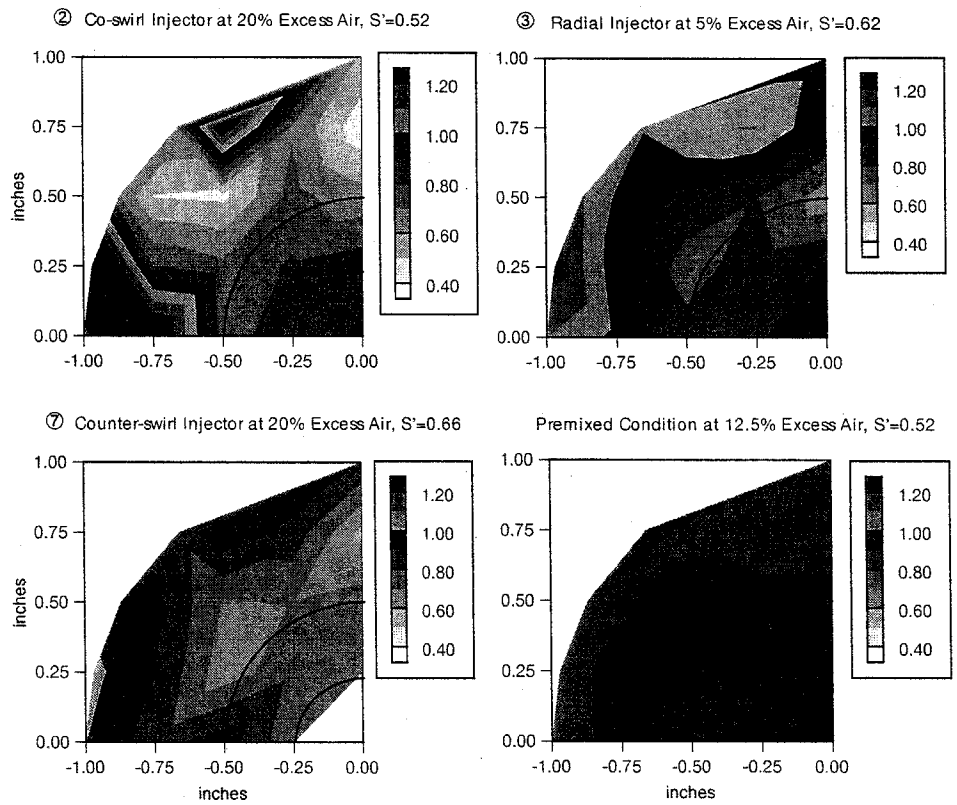

Figure 6.17: Local Equivalence Ratios Inside Quarl (z=0.5 inches)

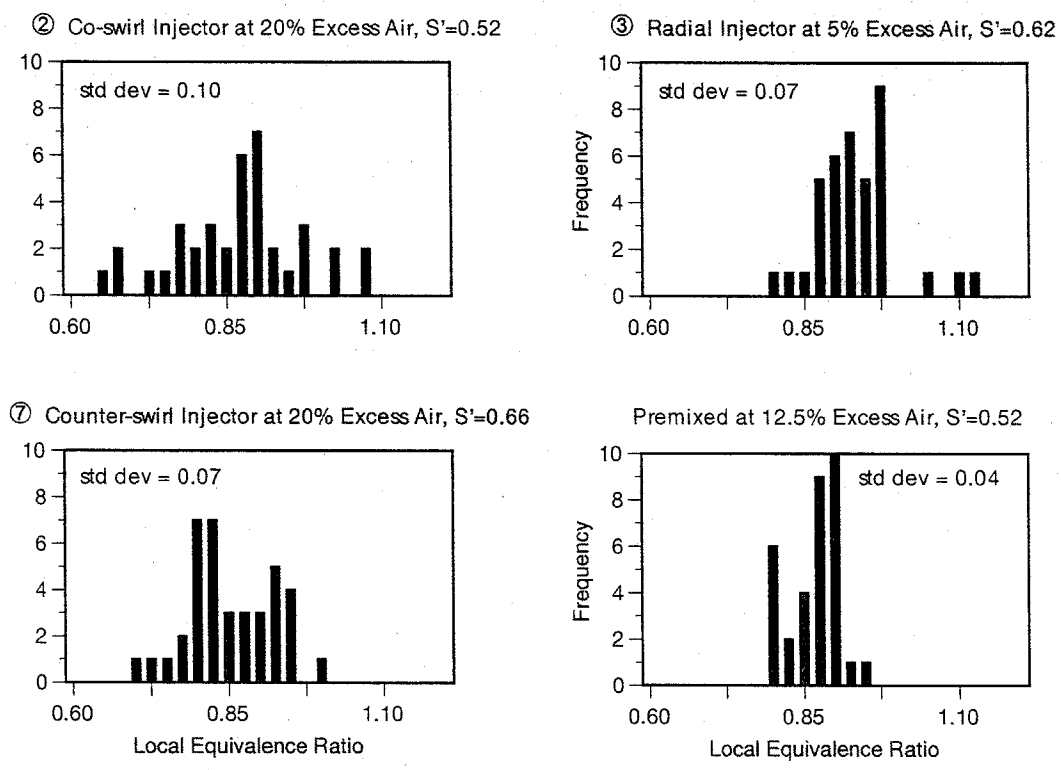

Figure 6.18: Local Equivalence Ratios at Quarl Exit
(red bar indicates theoretical average equivalence ratio)

The measurements at the quarl exit indicate that the better mixed case (⑦) provides the best performance. However, the initial fuel and air mixing is what can be controlled, so measurements upstream are required. These measurements and modeling are presented in the next section.

6.3. Throat Investigations

In order to determine the fuel distribution at the burner throat, acetone was seeded into the fuel stream by diverting the fuel flow into a 5 gallon [0.019 m3], stainless steel canister, one quarter filled with liquid acetone; due to the low vapor pressure of acetone, the volume above the liquid was assumed to be a saturated vapor. The fuel flow was introduced into the bottom of the tank where it bubbled through the liquid acetone and then exited at the top, thereby seeding the flow with approximately 20% acetone. The Nd:Yag laser was used to form a horizontal laser sheet of 266 nm ultraviolet light across the simulated throat. An 8 bit, Xybion intensified camera was then used to capture the acetone fluorescence.

Fluorescence images of the lowest performing condition (② the co-swirl injector at 20% excess air) is compared to the best performing condition (⑦ the counter-swirl injector at 20% excess air, S'=0.66) in Figure 8.58. The images are 20 frame averages and have been pseudo-colored to illustrate the different concentrations. The intensity scale increases from white to red.

Despite the large difference in performance, the co-swirl and counter-swirl injectors at 20% excess air show similar fuel distributions. The co-swirl injector, however, has smaller, more discrete regions of high fuel concentration which correspond to the individual jets evidenced in the reaction photographs (Figure

6.9). The counter-swirl injector has larger regions of fuel that occupy a wider area of the annulus. These small differences have a large impact on the NO_x and CO performance of each injector.

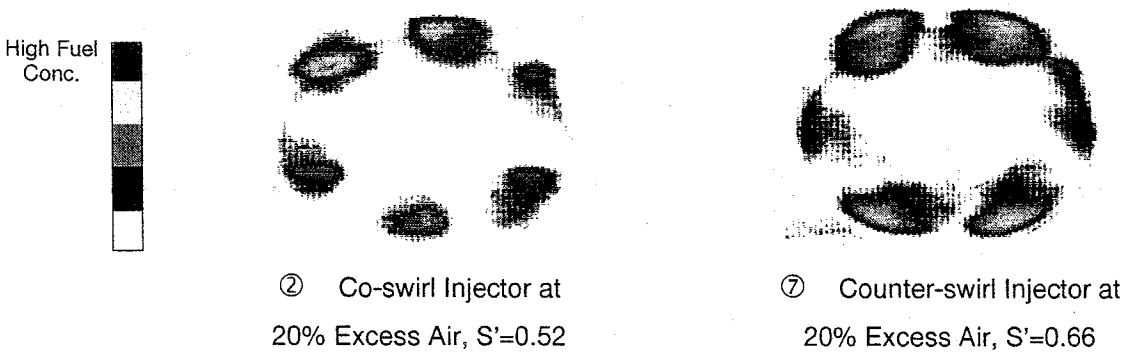

Figure 6.19: Acetone PLIF Fluorescence at Burner Throat

Due to the limited resolution of the camera, it was difficult to make quantitative comparisons of the images. It was clear from the measurements, however, that the fuel injection and subsequent mixing have a large impact on the fuel distribution and performance. The three-dimensional model of the burner throat was used to investigate the fuel injection more closely.

6.3.1. Modeling

The fuel mole fraction at the throat wall and throat exit are shown in Figure 6.20and Figure 6.21, respectively, for the selected three conditions. In Figure 6.20, the co-swirl injector shows limited fuel concentration at the annulus wall, indicating limited jet impingement. In contrast, the fuel jet impinges on the annulus wall (indicated by the orange and red colors) for the radial injector case. The counter-swirl injector shows slight impingement left of the injection plane, against the air flow direction.

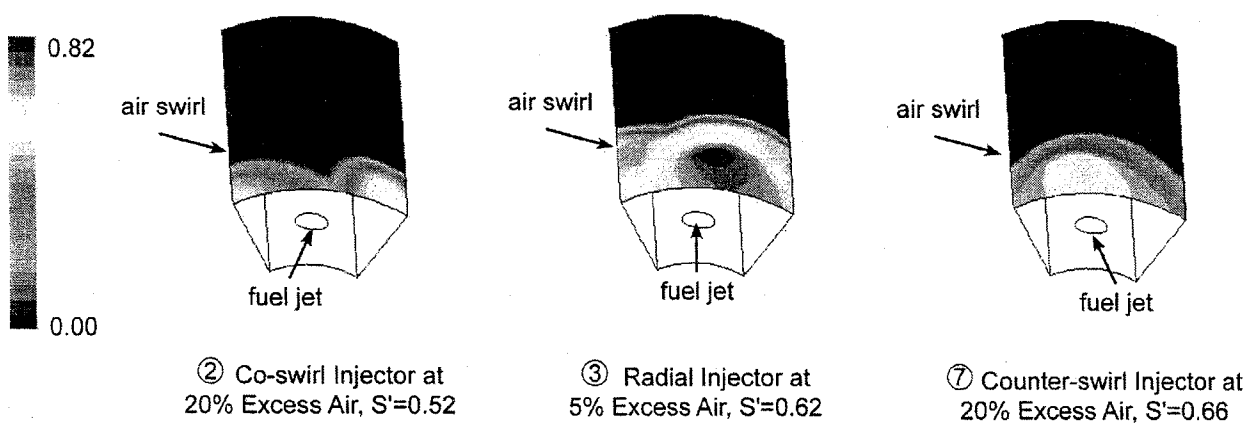

Figure 6.20: Modeling Predictions for Fuel Mole Fractions at Annulus Wall

The fuel mole fraction at the burner throat exit plane is shown Figure 6.21. The co-swirl injector conditions show large, discrete pockets of fuel at the exit, indicating jet coherence at the burner throat. For the radial injector, the fuel jet penetration forms a "ring" of high fuel concentration along the outer ridge of the annulus. Although the counter-swirl injector at 20% also shows a fuel ring around the annulus wall, absent are the large, undulating fuel pockets.

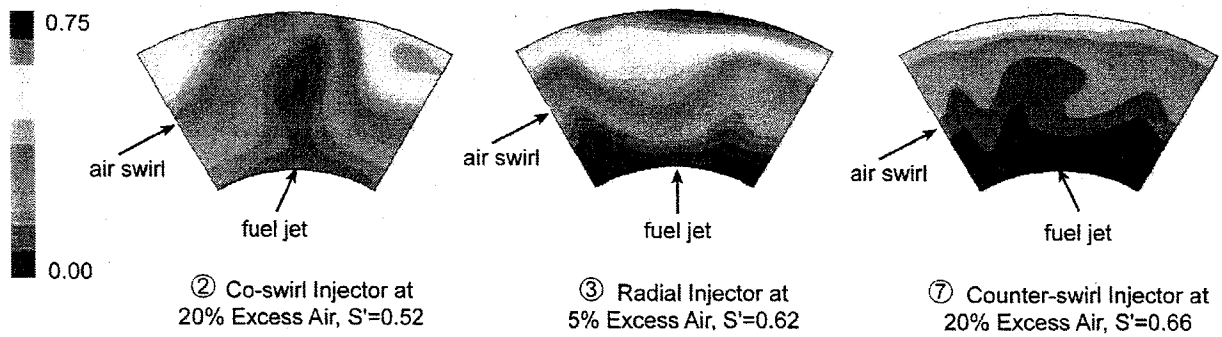

Figure 6.21: Modeling Predictions for Fuel Mole Fractions at Burner Throat

In order to visualize the mixing extent described in the modeling, under reacting conditions, a quartz quarl was installed to allow video of the reaction in the near-fuel jet injection region.

6.3.2. In-Furnace Video

A quartz quarl with a 4 inch elongated straight section was fabricated and installed to provide optical access to the burner throat. The Toshiba lipstick camera and air-cooling jacket were used to image the fuel injection plane and burner throat (see page 19, *Photography and Videography*). A false furnace bottom was also installed to provide the same entrainment patterns to the quarl exit and also serve to protect the video camera from heat and light pollution. The setup for the quartz quarl in-furnace video imaging is shown in Figure 6.22.

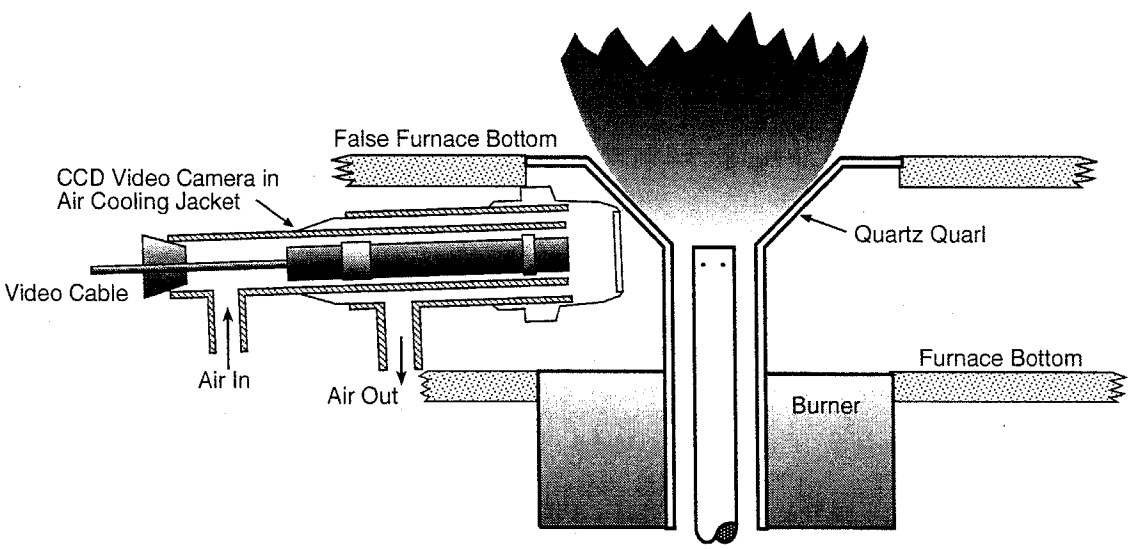

Figure 6.22: Quartz Quarl Video Setup

The ignition regions for the three different injectors is shown in Figure 6.23. From the modeling and previous measurements, the co-swirl injector is known to have the poorest fuel and air mixing; this is represented by the faint and thin ignition region. The radial injector has a small, compact ignition zone, due to the fuel jets' impingement on the annulus wall. The counter-swirl injector, exhibits a large, diffuse

ignition zone, indicating better mixing and more flammable reactants available early in the reaction process.

Co-swirl Injector Radial Injector Counter-swirl Injector

Figure 6.23: Ignition Region Size Comparison

Two other tests were conducted to determine the effect of swirl and excess air on the reaction structure. The first test held the excess air constant and increased the swirl intensity until blow-out while the other test held the swirl constant and increased the excess air until blow-out. The trends for all three injectors were the same, and so only the co-swirl injector images are provided in Figure 6.24. Increasing swirl is shown in the top two images and increasing excess air is shown in the bottom two images. Since the images on the right are nearing blowout, the reaction intensity and luminosity are diminished. The yellow box in each image indicates the region where the image contrast and brightness were adjusted to allow better visualization of the mechanism.

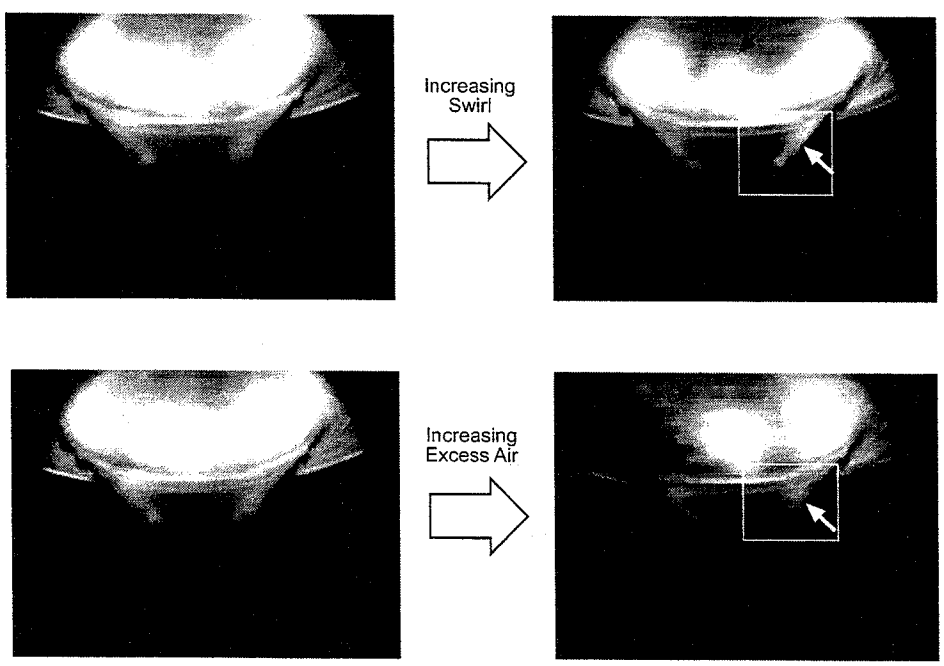

Figure 6.24: The Effect of Increasing Swirl and Excess Air

With increasing swirl, the ignition regions become longer and thinner (as indicated by the yellow arrow), and the downstream reaction petals become more discrete (indicated by the red arrow). The increase in swirl results in a larger recirculation zone in the center of the quarl, creating a higher shear region which "squeezes" the ignition pockets against the quarl wall. This increase in strain continues until flame stretch extinction occurs.

With increasing excess air, the shear mixing increases, diluting the ignition region and forcing it out of the burner throat (marked by the yellow arrow). As a result, the downstream regions are only sporadically ignited (indicated by the red arrow and the lack of a reaction petal). This is due to the increase in axial velocity which prevents the low velocity ignition regions from anchoring the reaction. The increase in shear also prevents the continuous connection between the ignition region and the downstream mixture. Thus, two different mechanisms for extinction are identified: extinction due to flame stretch occurs with too much swirl, and flame blow-out occurs with too much excess air or axial velocity.

6.4. Summary of Mechanistic Findings

The measurements and modeling in the burner were conducted to help illuminate the fuel–air mixing and reaction structure for the mixing variations, co-swirl, radial, and counter-swirl fuel injection. The major findings from these measurements and modeling results are provided below.

- Quarl exit and mid-plane measurements of emissions and temperature show the evolution of the reaction. The best performing condition (⑦, counter-swirl injector at 20% excess air, S'=0.66) has wider fuel distribution, a small central recirculated region of products (CO_2 and NO_x), and low concentrations of CO.
- The local equivalence ratios quantify the emissions observations in that the best performing condition has the most uniform and lean equivalence ratio distribution at both the quarl mid-plane and exit plane, illustrating the better fuel and air mixing for this condition. In contrast, the co-swirl injector displays discrete pockets of very high equivalence ratios, definitively showing the poor fuel and air mixing inherent in this injection strategy.
- Acetone PLIF images of the burner throat further illustrate the fuel distribution differences. The best performing condition, the counter-swirl injector at 20% excess air, S'=0.66 (⑦), has a wide fuel distribution which fills the entire throat, with the highest concentrations occurring nearest the throat wall. The co-swirl injector at 20% excess air (②) has small, discrete regions of fuel, indicative of poor fuel-air mixing.
- CFD modeling of the near-injection region predicts that the fuel jets impinge on the annulus wall for all cases except the co-swirl injector. The predicted throat exit concentrations of fuel qualitatively agree with the acetone PLIF images in that the co-swirl injector has small discrete regions of fuel whereas the counter-swirl injector displays a wider, more uniform fuel distribution.
- Video images of the burner throat show small luminous pockets form at the burner throat, providing the ignition region between and in the wake of the jet impingement locations. The co-swirl injector has thin and long ignition packets and the counter-swirl injector displays larger diffuse packets.

In order to assimilate and process the presented data, a comparison of the high (⑦) and low (②) performance conditions is provided in Table 6.2. Since these two conditions encompass the entire performance range, the implications are more easily identified.

Table 6.2: Results Summary

Counter-swirl Injector at High Performance	*Co-swirl Injector at Low Performance*	*General Findings and Implications*
Exhaust Measurements: • Low CO and high NO_x • Good performance at high excess air and high • Excess air has greater effect than swirl on NO_x	• High CO and low NO_x • Poor performance at high swirl • Excess air not as large a factor	☞ Fuel delivery and cross-flow mixing are important ☞ Fully premixed is *not* optimum
Downstream Measurements: • Petal-like annular structure • Moderate OH and luminosity • Moderate temperatures • Quick CO and HC burnout • Moderate recirculation zone	• Discrete reaction petals • Low OH and luminosity • Lowest temperatures • Slow CO and HC burnout • Largest recirculation zone	☞ Dynamic structure ☞ No reaction and low T fluctuations in center ☞ No central NO_x forming region; NO_x forms along reaction petals ☞ Internal FGR mechanism suggested
Burner Measurements: • Highest negative centerline axial velocities • Broader fuel distribution and small region of recirculated products • High velocity fluctuations at throat • CFD modeling show impingement at annulus wall • Diffuse ignition eddies at throat	• Slowly decaying negative centerline axial velocities • Discrete fuel distribution and large region of recirculated products • Moderate velocity fluctuations at throat • Limited impingement at annulus wall • Thin ignition eddies at throat	☞ Internal FGR evidenced ☞ Impingement provides mixing and ignition stability at throat ☞ Fuel distribution linked to performance ☞ Flame stretch extinction at high swirl limit ☞ Blow off of throat eddies at high excess air limit

Based on these findings, a reaction mechanism is proposed and illustration in Figure 6.25.

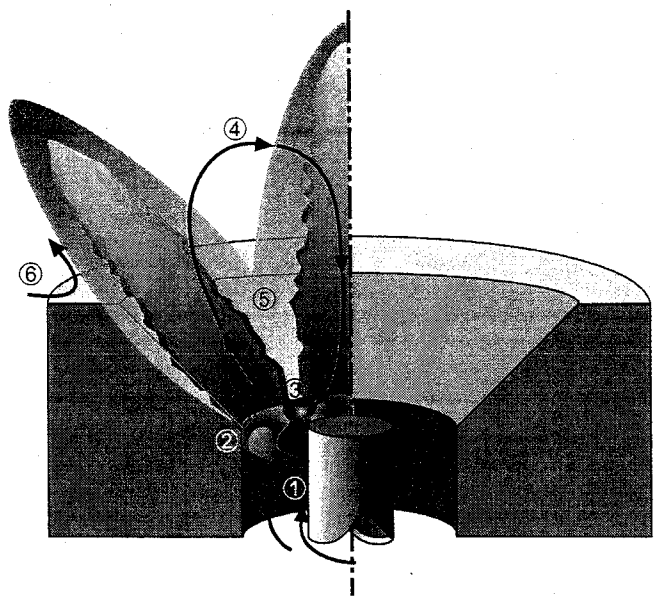

Figure 6.25: Reaction Mechanism for Model Industrial Burner

The fuel jet enters the swirling, cross-flow annulus at ①. The amount of initial mixing is dependent on the fuel injection, with counter-swirl injection providing the most initial mixing and co-swirl fuel injection providing the least amount of initial mixing in the annulus. Impingement of the fuel jet against the annulus wall can occur at ②; however, the location and extent of impingement are dependent on the fuel injection direction, excess air level, and swirl input. The co-swirl injector experiences the least amount of impingement since it is traveling in the same direction as swirling air flow.

Partial premixing and impingement that occur perform several important functions: these factors 1) allow the region between adjacent jets to mix to below the rich flammability limit and 2) establish the fuel distribution and stoichiometries at the periphery of the fuel jets. The ignition location, ③, must have flammable fuel and air mixture ratios, low velocities to sustain the reaction, and a recirculating ignition source. The source of reactive intermediates is provided by the recirculation zone, ④, which recirculates the hot combustion products back upstream to ignite the fresh mixture.

The recirculating flow also forces the reaction outward radially, defining the reaction zone thickness and allowing reaction only between the fuel jets while inside the quarl. The mixing shear layer between the reaction and the recirculated products at ⑤ creates the internal FGR mechanism. If the recirculation zone is very large (e.g., for the co-swirl injector), high CO and HC emissions can result if the reaction is quenched by the large amount of cooler product gases entrained into the reaction zone. If the recirculation zone is increased still, the reaction and ignition regions are squeezed between the recirculation zone and quarl wall, resulting in flame stretch, instability, and eventually extinction. The external recirculation and entrainment occur at ⑥ to provide more air and some combustion products to complete the reaction downstream. Since this region is dependent on entrainment for mixing, the flow velocity affects the subsequent mixing and burnout.

All of the premixing prior to ignition occurs at stages ① and ②. As such, the greater mixing occurs with the counter-swirl injector at the higher excess air conditions due to the increased cross-flow velocity and

subsequent wider fuel distribution. This initial mixing and impingement set up the fuel jet trajectory as it mixes and reacts downstream. Since the mixing is limited once the flow issues into the quarl and interacts with the recirculation zone, this initial mixing is critical for establishing the reacting, local equivalence ratios and thus, the emissions. Perfect premixing, however, does not provide the best performance, as seen in Figure 6.8. Furthermore, several researchers have determined that an optimum level of *partial* premixing exists for improved emissions (Turns *et al.*, 1993; Gore and Zhan, 1996; and Kim *et al.*, 1995).

6.4.1. Application of Mechanistic Understanding

In light of these explanations, condition ⑦, the counter-swirl injector at 20% excess air, S'=0.66, exhibits optimal performance due to

- higher levels of partial premixing as a result of the cross-flow mixing, fuel injection orientation, and jet impingement;
- large ignition regions, allowing stable reaction and good propagation downstream;
- moderate internal FGR which provides NOx reduction without quenching or stretching the reaction; and
- high velocities that provide increased shear mixing and entrainment for quicker CO burnout downstream.

In contrast, condition ②, the co-swirl injector at 20% excess air, exhibits poor performance due to

- poor initial mixing as a result of limited cross-flow mixing and impingement;
- thin ignition regions with poor propagation downstream; and
- larger recirculation zone causing excessive internal FGR and stretching of the reaction front.

These mechanisms now allow the explanation of the global performance trends. The performance, *J*, vs. swirl intensity is shown in Figure 6.26 for the counter-swirl and co-swirl injectors at 20% excess air.

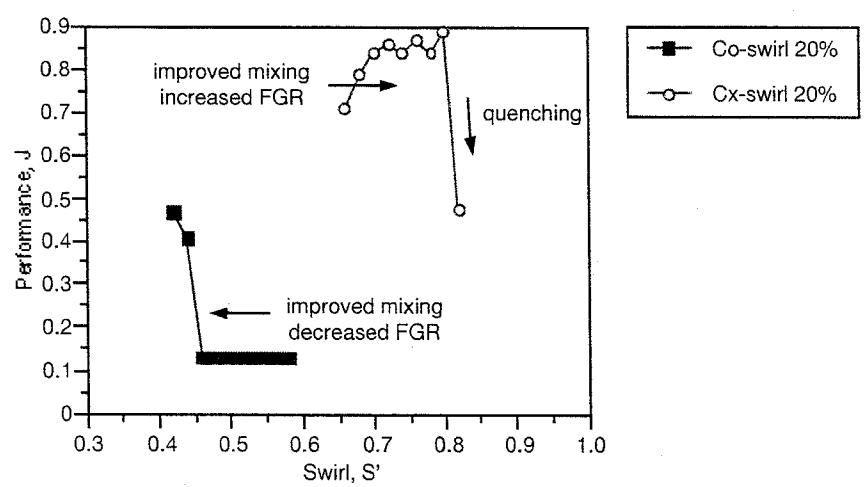

Figure 6.26: Performance vs. Swirl Intensity at 20% Excess Air for Co-swirl and Counter-swirl Injectors

The counter-swirl injector displays better performance overall due to the greater lean fuel distribution. Increasing swirl intensity increases the recirculation zone size, reduces the reaction zone width, and increases the FGR providing NO_X reduction; at the highest swirl value, however, quenching and high CO emissions drop the performance. The co-swirl injector displays overall low performance due to poor fuel distribution and high internal FGR. Unlike the counter-swirl injector, performance increases with *decreasing* swirl due to the reduced internal FGR and the improved cross-flow velocity mixing from the larger axial velocity component.

Although the conventional, in-flame, low NO_x technique of FGR was not directly applied during this program, it is clear from the previous investigation that this type of technique could be introduced to further reduce the overall reaction temperature and NO_x levels. It is expected that the trends of the data would remain consistent since the mechanisms of NO_x reduction would still be due to fast partial premixing of the fuel and air and *internal* flue gas recirculation. The expected trade-off for this NO_x reduction would be a reduction in the lean stability limit due to the quenching phenomenon illustrated in Figure 6.26.

6.5. Active Control Development

Armed with this mechanistic understanding, it was determined that the NO_x and CO active control methodology could rely on the careful management of the initial fuel mixing (controlled by the excess air level and fuel injection direction) and induced flue gas recirculation (swirl intensity and excess air level).

6.5.1. Strategy

The adopted active control strategy is thus to control the fuel and air injection in order to affect the mixing and emissions. The three major components required for active control optimization are shown in Figure 6.27: ① a controllable combustion device, ② an array of feedback sensors, and ③ the computer logic to process the feedback information from the sensors and change the combustion device. The research in this program has focused on developing the combustion device, determining the method of control, applying industrial sensors using conventional emissions analyzers, and integrating these components into an active control system.

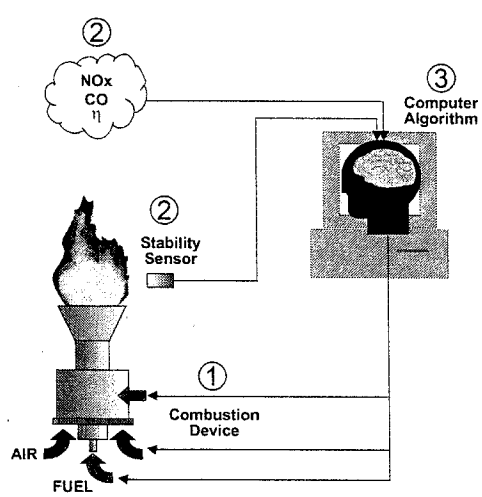

Figure 6.27: Active Control Strategy

The previous work funded by CIEE established that this strategy could work for the model industrial burner (St. John, 1994). The major development under this program was to apply the active control concept to a more industrial burner; the Coen, scaled down Quantum Low NO_x (*QLN*) burner was used for this purpose. Several other improvements were also implemented during the investigation, which will be discussed in the following sections.

6.5.2. Improvements

In order to continue improving the active control concept, several important features were added to the original methodology:

1. Data acquisition using industry standardized software package (*LabView*),
2. Modular coding for greater portability and upgradeability,
3. Incorporation of system efficiency to the cost function, and
4. Demonstration on "real" industrial hardware, fabricated by a major burner manufacturer.

The scaled *QLN* burner was designed and manufactured by Coen for these tests. A schematic of the burner was shown in Figure 5.6. This is a low NO_x burner design that is currently marketed by Coen. The only modifications done to the burner were to add mass flow controllers to the air line and fuel lines in order to have computer and algorithm control of the flow rates for the active optimization.

The modular coding was conducted using a commercial software package, National Instruments' *LabView*, considered by many to be the industry standard for data acquisition. The previous active control program (St. John and Samuelsen, 1994) was written in *Visual Basic*. Although this program worked very well and incorporated a user-friendly interface, the programming and data acquisition were difficult to modify or incorporate new search algorithms. For the current active control program, a modular approach was adopted using *LabView* as the data acquisition engine and different software packages to code the algorithms. A schematic of the software concept is shown in Figure 6.28.

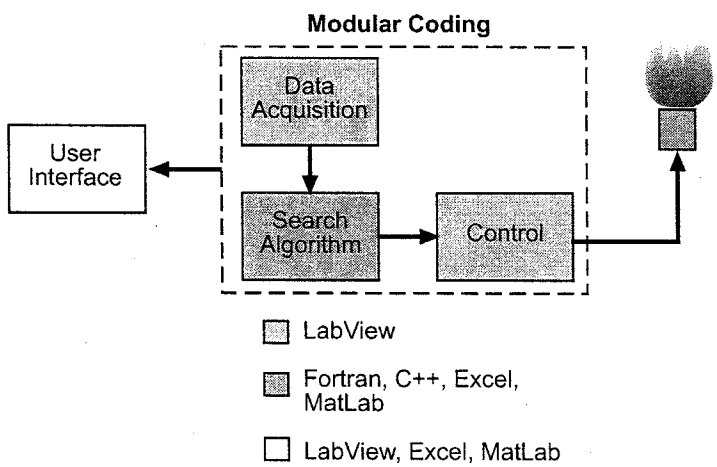

Figure 6.28: Second Generation Active Control Concept

The active control program modules consist of three parts: data acquisition, algorithm, and control; the dashed line in Figure 6.28 represents components that will be transparent to the user in the completed version. The data acquisition and control aspects were handled by *LabView* and National Instruments data acquisition cards. The actual control layout is shown schematically in Figure 6.29. This layout includes future desired upgrades, such as the stability monitor.

The control algorithm was coded using *Fortran* (for the industrial burners) and the conventional direction-set, or Powell's method, of optimization. This optimization strategy simply looks in a prescribed direction for a maximum value of performance. If the new value is higher, then the system continues in that direction; if the new value is lower, the system returns to the previous point and initiates a search in a new direction.

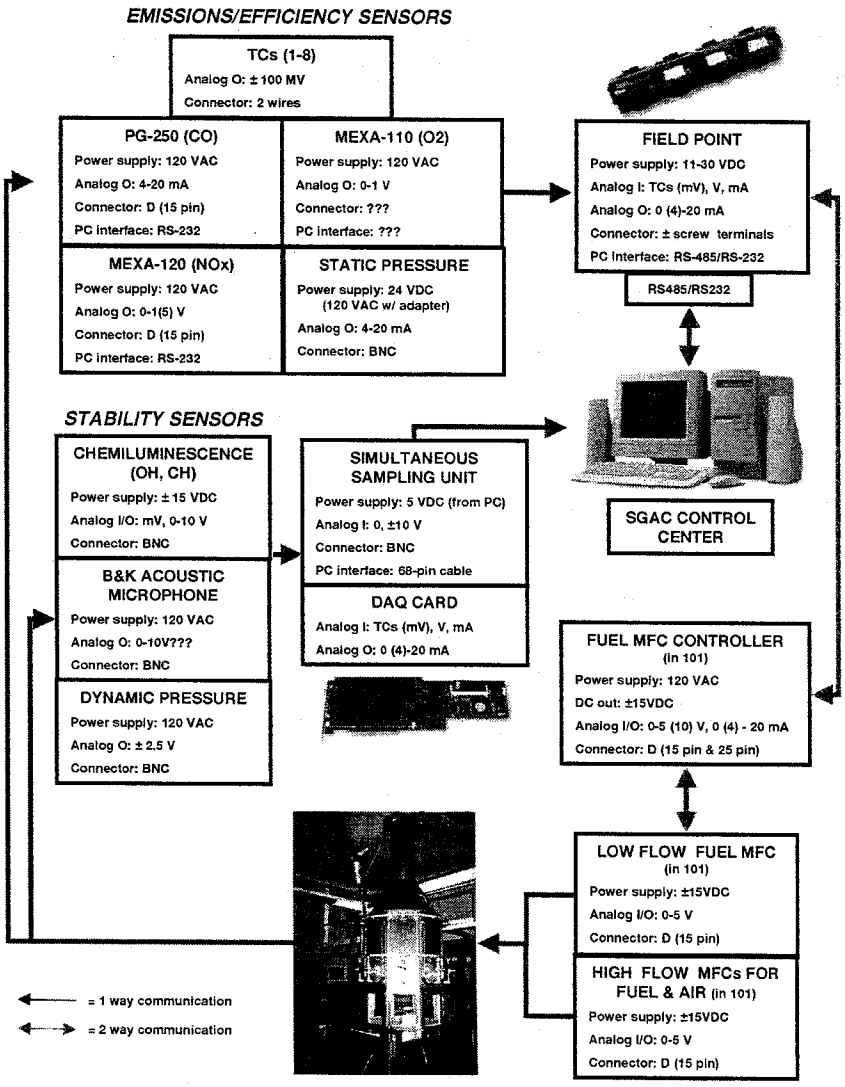

Figure 6.29: Active Control System Schematic

A challenge associated with this simple technique is that the prescribed direction and step size are often times inadequate for all conditions and can optimize on local peaks. An algorithm which can adjust and learn from previous runs would be useful (e.g., fuzzy logic). The next steps for this research will include the comparison of different optimization techniques and incorporation of a "learning" mode to minimize the time for optimization.

An important characteristic of the active control system is the use of a cost function for optimization. This function was previously described in section 6.1.1 Performance Index. For industrial burners, the major operational parameters are low emissions and low cost. The performance function used accounts for NO_x and CO, however, it does not account for system efficiency or a cost factor. In order to

accommodate this factor, the total amount of excess air (or stack O_2%) was incorporated into the performance function. The results of these tests as well as with the baseline performance function based on pollutant emissions are shown in the following section.

6.5.3. Active Control Results

As shown in Figure 5.6, the *QLN* has three fuel streams: core, radial, and outer. The core fuel was set at 25% of the total firing rate, and the remaining fuel was varied between the radial and outer spuds. The remaining fuel was defined as

$$fuel\ split = outer\% - radial\%$$

For example, if all of the remaining fuel is diverted to the outer spuds, this was considered "75% fuel split," or more staging. Conversely, if all of the remaining fuel is diverted to the radial spuds, this was considered "–75% fuel split," or more premixed. The performance map for the *QLN* burner is shown in Figure 6.30. These results indicate a ridge of high performance along the stability limit (represented by the red color).

Using the stack emissions analyzers as the feedback sensors, optimization tests were conducted. The resulting operational history is provided in Figure 6.31.

The active control system successfully optimized to the ridge of high performance located at 25% excess air after 9.5 minutes. This plot, however, exemplifies a limitation of the original performance function based on NO_x and CO emissions; specifically that system efficiency is ignored so higher excess air values are not penalized. A modified performance function was developed to incorporate the stack O_2%, which can be related to system efficiency (Thompson, Shiomoto, and Muzio, 1999).

$$J = w \cdot f(NO_x) + w \cdot g(\eta) + w \cdot h(O_2)$$

For these tests, each function was weighted evenly at 1/3 and the function $h(O_2)$ was linearly increasing with decreasing stack O_2. After incorporating this system efficiency modification, the peak is no longer located at high excess air values and actually relocates to 5-10% excess air and 0-30% fuel split. The map for this performance definition is shown in Figure 6.32.

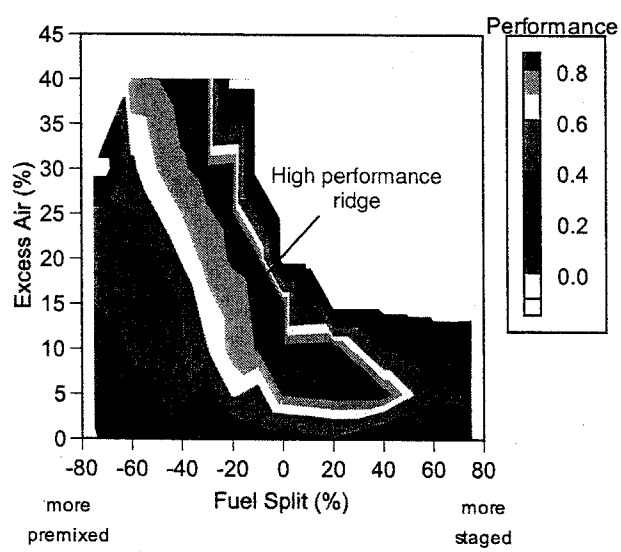

Figure 6.30: *QLN* Burner Performance Map

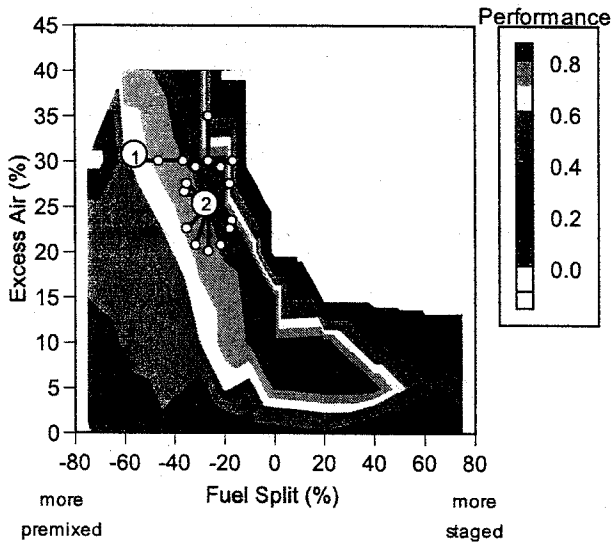

Figure 6.31: *QLN* Active Control History
[① start, ② finish]

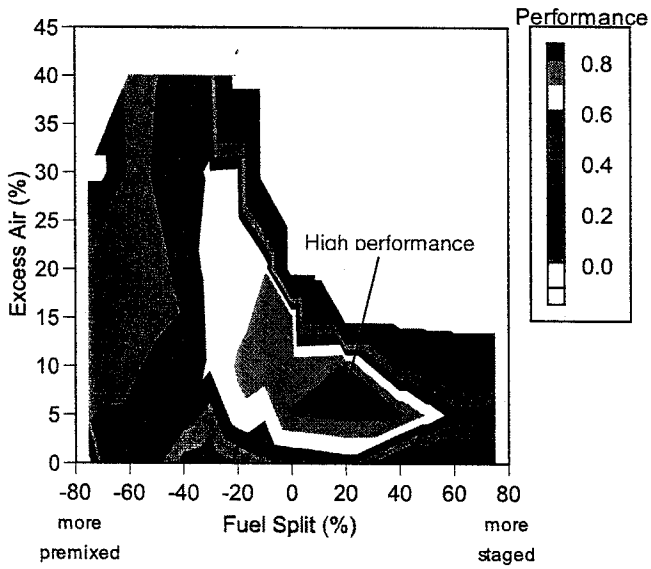

Figure 6.32: *QLN* Burner Performance Map with System Efficiency Factor

The optimization was repeated using this performance definition and the exhaust emissions analyzers for feedback. The active control system successfully optimized in the region of high performance, at lower excess air and more fuel staging, with a response time of 16 minutes. The optimization history is shown in Figure 6.33.

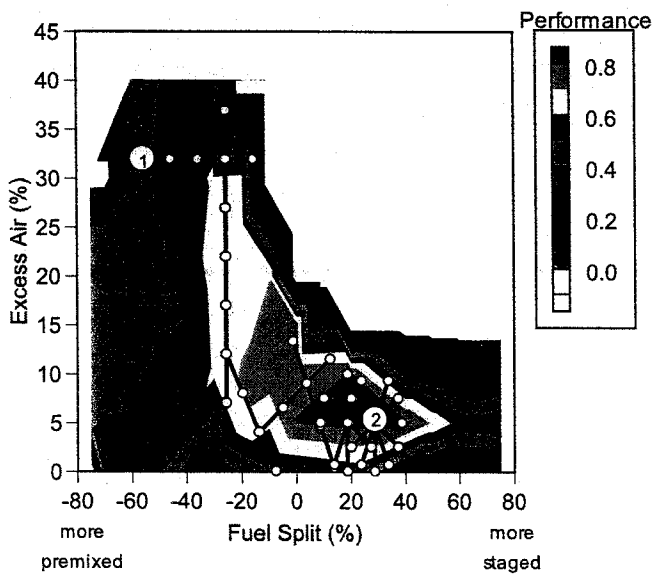

Figure 6.33: *QLN* Active Control with System Efficiency Factor
[① start, ② finish]

For both cost function definitions, the active control system was able to appropriately optimize in the high performance region.

It should be reiterated here, that although equal weighting was applied to all of the control parameters in the cost function (NO_x, CO, and O_2), these factors can and should be adjusted to meet the end-users' regulatory and economic requirements. For example, since NO_x emissions are regulated, the operator would preferentially weight NO_x over cost factors such as system efficiency (O_2). The affect of adjusting the weighting factors would simply change the size of the high performance regions, but the trends of the contours would remain. For example, adjusting the weighting factors to favor the regulated emissions (NO_x and CO) by 75% and the system efficiency by 25% results in the performance map shown in Figure 6.34.

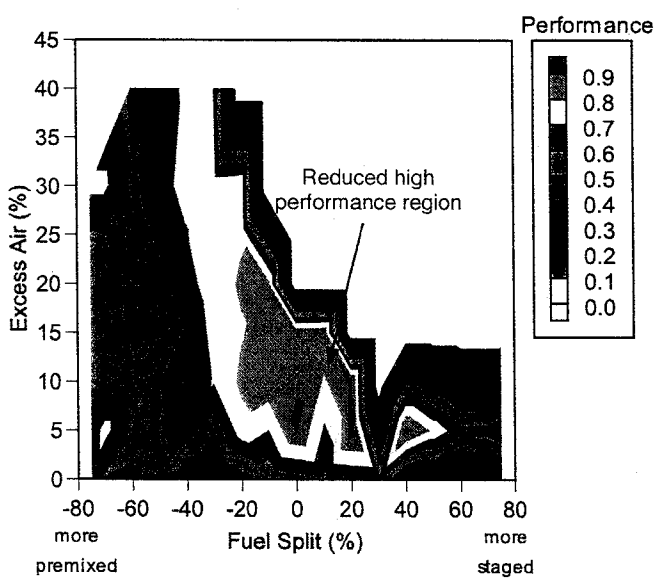

Figure 6.34: *QLN* Burner Performance Map with Adjusted Weighting Factors

This figures illustrates that such a weighting gives little operational flexibility and demonstrates the need for an *active* system to consistently and constantly optimize the burner.

6.5.4. Active Control Summary

Using the mechanistic understanding gained from the detailed measurements in Task 1, the active control methodology was further developed. Since the fuel and air mixing were demonstrated to affect and control the performance, the fuel and air delivery were modified to be computer/algorithm controlled. The active control program was modified in several areas to take advantage of improved computer processing advancements and make future upgrades and changes more user friendly. These modifications included adoption of new data acquisition software and hardware, a modular coding environment, adoption of a new cost function, and application to a real industrial burner design (Coen *QLN*). The modified active control program was successfully demonstrated on the model Coen *QLN* burner. The active control methodology and mechanistic understanding garnered during the Task 1 phase set the groundwork for the industrial burner testing that followed in Task 2.

7. TASK 2A – BOILER SIMULATOR

The focus of this task was the transition of the information garnered from the technology development phase to a more realistic and industrial burner scale. The testing platform in this case was the 400,000 Btu/hr Coen *QLN* Burner.

This section summarizes the research conducted to characterize the scaled Coen *Quantum Low* NO_X (*QLN*) burner, firing at 400,000 Btu/hr. The values measured included exhaust stack emissions, in-situ emissions and temperatures via intrusive probe, and velocities using laser anemometry. A major tool used for these experiments was *Design of Experiments* (DoE), which is a statistical methodology that allows fewer tests to be conducted in order to discern effects due to input factors (such as geometric or operational changes) or combinations of these factors. The variable input factors were fuel split, radial spud depth, throat depth, outer spud depth, and outer spud direction. The responses of interest were NO_X emissions, combustion efficiency, and system efficiency based on heat extraction from the water-cooled panels. The results of the study indicate the most influential factors on NO_X emissions are the fuel split and throat depth. Based on these results, an optimized configuration was selected for detailed, in-situ measurements of temperature, emissions, and velocity (using laser anemometry). A poorly performing configuration was also selected and tested for comparison.

A repeat of the DoE measurements was conducted by a different experimenter to ensure the validity of the data and trends, as well as to establish confidence in the testing protocol. With this confidence, further measurements were conducted on a modified *QLN* configuration with higher velocity radial spud injectors; this configuration was based on a radial spud design more closely aligned with the commercially available *QLN*. A similar DoE was conducted to determine if the emissions, combustion efficiency, and system efficiency were affected by the geometric change. According to the statistical design, the two factors which play a major role in the NO_x emissions were again identified as the fuel split and throat depth.

7.1. Design of Experiments Methodology

Design of Experiments (DoE) is a statistically based approach to experimentation. It can best be described as "a series of tests in which purposeful changes are made to input factors to affect a process and its associated responses." The purpose of DoE is to make the experimental process efficient and the analysis of data statistically sound. The root theory behind this approach is to eliminate testing one factor at a time and instead to incorporate randomization. By randomizing the experiment, probability and statistical techniques may be used in the analysis of the data results. This allows an experimentalist to quantify uncertainties, provide results with statistical confidence levels, and to develop a mathematical model correlating the factors and responses.

In this approach, a researcher first identifies all the factors and responses involved in his or her experiments. In this study, the subject under investigation was the scaled, industrial burner. The variable factors of this burner were either geometrical or operational parameters. The responses of the burner were NO_X emissions, combustion efficiency, and system efficiency. The next two paragraphs explain the factors and measured responses of this burner.

The input factors of this burner are radial depth, throat depth, outer depth, outer direction, overall excess air, and fuel difference. The first four of this list are geometrical parameters and the last two are operational. The four geometric parameters and their respective ranges are shown graphically in Figure 7.1. The operational parameter of overall excess air should be self-explanatory. The higher this value is, the more air is supplied to the burner and thus the more lean its operation. In the initial development of the DoE test matrix, this value was chosen to range from a low of 10% to a high of 30%.

These values were chosen on the basis that typical operation of this burner in boiler applications would be between 15% to 20% excess air. The second operational parameter is titled fuel difference. Since this burner has three fuel lines and a constant total fuel flow rate of 6.58 scfm, this allows the user to select how much fuel should be injected at each location. The fuel flow rate for the core injector was chosen to be held constant at 25% for these tests. An explanation for this decision will be given in the early sections the Results. This leaves 75% of 6.58 scfm to be split between the radial and outer fuel injectors. The operational parameter fuel difference is defined as the percent difference between the outer and radial fuel flows. Therefore, a value of +5 would mean that 40% (2.63 scfm) of natural gas is supplied to the outer injectors and 35% (2.30 scfm) of natural gas is supplied to the radial injectors. A value of 0 would indicate equal flow (37.5% = 2.47 scfm) between the outer and radial fuel injectors.

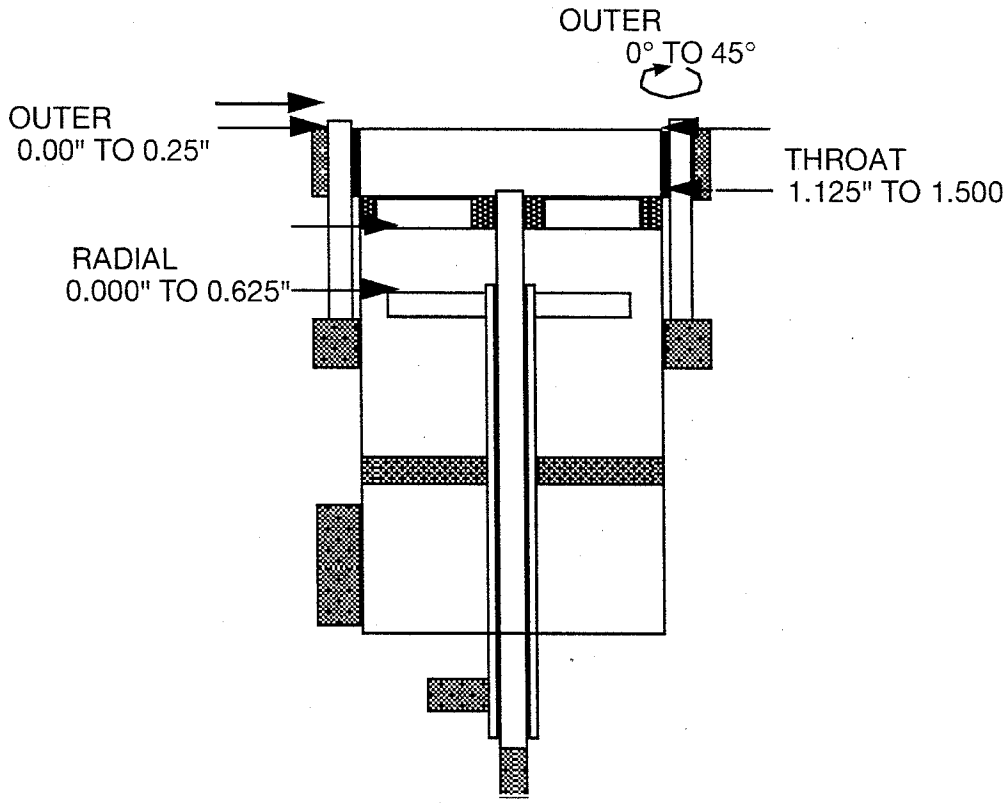

Figure 7.1: Variable Geometric Parameters on Subject Burner

The responses to be monitored in these tests are NO_X emissions, combustion efficiency, and system efficiency. All NO_X emissions are measured via the stack and then corrected to 3.0% O_2. Combustion efficiency is a function of the fuel used and the measured CO and HC stack emissions. The third response, system efficiency, was based on the flow rate, the bulk inlet temperature, and the bulk outlet temperature of the water passing through the panels. These measured values could be used in the equation $Q = m \cdot c_p \cdot \Delta T$ to calculate the total amount of heat extracted through the panels. The desired system efficiency was to maximize the water heat extraction.

Now with a concrete understanding of all the factors and responses of this burner, a DoE matrix may be developed. In this development phase, a sequence of choices must be made. The first decision is to select the type of design. Since this burner experiment has 6 factors, each of which have a range of values, a 2-level factorial design was chosen. A factorial design simply implies that more than one factor is involved

in the experiment. A 2-level design implies that each factor has a specified low and high value. Therefore, in general, a 2-level factorial design is generated by selecting a high and low level for each of the factors and then placing all possible combinations of these in a test matrix. For example, with 6 factors at 2 levels each, the total number of experiments required would be $2^6 = 64$. This type of test matrix is called a full 2-level factorial. The word "full" is used to set it apart from "fractional" 2-level factorials. The difference between these two designs will be explained in the next paragraph.

Using the example from the previous paragraph, a full 2-level factorial with 6 factors would require 64 runs. From these runs, 64 statistics can be calculated which estimate the following effects:

		Interactions				
Average	Main Effects	2-Factor	3-Factor	4-Factor	5-Factor	6-Factor
1	6	14	22	14	6	1

Figure 7.2: Statistical Effects for a Full 2-Level Factorial with Six Factors

Even though all these effects can be calculated, they are not of equal importance or magnitude. In terms of magnitude, main effects tend to be the highest, then 2-Factor effects, then 3-Factor effects, and so on. This phenomenon, therefore, often allows the experimentalist to neglect higher order interactions. By doing so, an experimentalist largely reduces the number of runs required to achieve largely similar results as if he or she had done all possible combinations. Therefore, in the example given, a half-fractional 2-level factorial would only require 32 runs, and a quarter-fractional factorial would only require 16 runs. These test matrices can also be designated as a 2^{6-1} and 2^{6-2} factorials, respectively. The trade-off when performing fewer runs in an attempt to glean the same information is a loss in resolution. While a full factorial would provide all statistical details, a fractional factorial would have to implicitly calculate some higher order interactions and may eliminate others altogether. In conclusion, the final decision on which factorial (full or fractional) to perform is a trade-off between efficiency and resolution. For this research, a half-fractional factorial was selected. A half-fractional factorial with 6 factors has a designated resolution of VI. According to Box, Hunter, and Hunter, resolution VI designs are just about as accurate as full factorials, assuming that no four factor (and higher) interactions occur (Box, Hunter, and Hunter, 1978).

After the type of factorial is selected, three other important decisions must also be made. These are replicates, blocks, and center points. Replicates are simply repeats of test conditions. By incorporating replicates in a test matrix, an estimate of experimental error or standard deviation of the effects is made possible. For this matrix, a single replicate was chosen for each of the 32 test conditions. A second option in the matrix development phase is to block experiments. This allows the researcher to place experiments in categories which share something in common. For example, if half of the runs were performed on day one and the second half on day two, he or she may select two blocks. This may increase accuracy, but one or more effects will not be estimable due to blocking. Even though the test runs for this DoE matrix were taken on various days, a single block was still chosen. The final option is center points. Center points allow estimates of pure error and test for curvature of the response in relation to the input factors. For this matrix, five center points were chosen.

The end result of this development is a randomized DoE test matrix with a total of 69 runs (32 original, 32 replicates, and 5 center points). Design-Ease™ software was used to develop the matrix and was also used in the post-processing of the data after the completion of the experiments. Figure 7.3 shows an image of the first 10 runs of this matrix. The first column is the run's design identification; notice that

runs 1 and 10 have the same identification and are repeats of one another. The second column is the actual run order. The third column is the block number, which is 1 for all runs in this matrix. The next six columns are the six factors, and the last four columns are the responses. All 69 runs were performed and the data results will be explained in the following section.

Std	Dsn Id	Run	Block	Radial Depth inches Factor	Throat Depth inches Factor	Excess Air % Factor	Outer Depth inches Factor	Fuel Diff % Factor	Outer Dir. deg Factor	NOx ppm Response	Comb. Eff % Response	Sys Eff. (#1) % Response
7	4	1	1	0.000	1.500	10.00	0.000	-5.00	0.00			
2	1	2	1	0.625	1.125	10.00	0.000	-5.00	0.00			
58	29	3	1	0.625	1.125	30.00	0.250	5.00	45.00			
13	7	4	1	0.625	1.500	30.00	0.000	-5.00	0.00			
30	15	5	1	0.625	1.500	30.00	0.250	-5.00	45.00			
5	3	6	1	0.625	1.500	10.00	0.000	-5.00	45.00			
14	7	7	1	0.625	1.500	30.00	0.000	-5.00	0.00			
36	18	8	1	0.000	1.125	10.00	0.000	5.00	0.00			
21	11	9	1	0.625	1.500	10.00	0.250	-5.00	0.00			
8	4	10	1	0.000	1.500	10.00	0.000	-5.00	0.00			

Figure 7.3: Image of First 10 Runs from Design of Experiments Test Matrix

This section explains the results of the experiments. For clarity, it is also subdivided into two major sections: (1) design optimization and (2) characterization. This section details the accomplishments of the tasks three through seven from section 3 and seeks to reach the goals of the study. As a reminder, the five objectives are explicitly restated here:

- Define the stability limits of the burner. Quantify NO_X emissions over identified stability range.
- Delineate a strategy to statistically identify the important geometrical and operational factors. Utilize Design of Experiments (DoE) to develop a test matrix
- Conduct emissions and efficiency testing of 69 runs in the DoE matrix. Determine statistical significance of results with DoE analyses.
- Identify high burner performance and low burner performance configurations.
- Acquire detailed in-situ data of the velocity, temperature, and species fields at both high performance and low performance conditions.

7.2. Design Optimization

This major section will explain the accomplishment of the first four objectives listed above. This section is subdivided into four sections. The first provides results of the first two objectives; the second and third provide results of the third objective; and the fourth sub-section provides results of the fourth objective.

Stability Exploration and Test Matrix Development

After the burner and all accessory components were successfully installed, initial exploratory testing began. The purposes of these first experiments were to: (1) identify the stability limits of the burner and (2) select the range of variation for the geometrical and operational parameters.

An equal and important purpose of these first tests was to finalize the first overall goal of this Thesis: to develop a scaled burner which simulates the full-scale, industrial model. This goal was completed

through on-site visits by the burner manufacturer. A burner configuration was specified by the company representative and the burner was ignited. While reacting, minor changes were made to the placement of the core fuel injector until the representative was satisfied with the appearance of the burner. At the conclusion of this visit, the representative gave approval of the burner because of its notably similar characteristics to the full-scale, industrial model.

The subject burner is designed to operate at a full load of 400,000 Btu/hr. This simply means that the total fuel flow rate to the burner is held constant at 6.58 scfm for all tests. This value of 6.58 is attained by calculating the higher heating value of the laboratory's natural gas and then calculating the required fuel flow rate to achieve 400,000 Btu/hr. As is explained in the *Experiment* section, this burner operates with three fuel lines. Therefore, 6.58 scfm must be split among these three lines. One goal in these initial stages was to decide on how much fuel would be supplied to the core injector. Emissions and stability tests were conducted at a single baseline, geometrical configuration. Input from the burner manufacturer stated the core fuel flow rate should be greater than 10% but less than 25% of the total fuel flow. With this in mind, testing was began at a core flow rate of 15%, or 0.99 scfm. With only a few tests, it was readily apparent that the burner would not remain stable with this flow rate. An increase in flow to 18% was a definite improvement but the burner would still blow out at approximately 20% excess air. Three more core fuel percentage conditions (19%, 22%, and 25%) were performed. Each increase in core fuel flow rate showed a direct increase in stability, but also an increase in NO_X emissions. Figure 7.4 shows these results over a range of excess air.

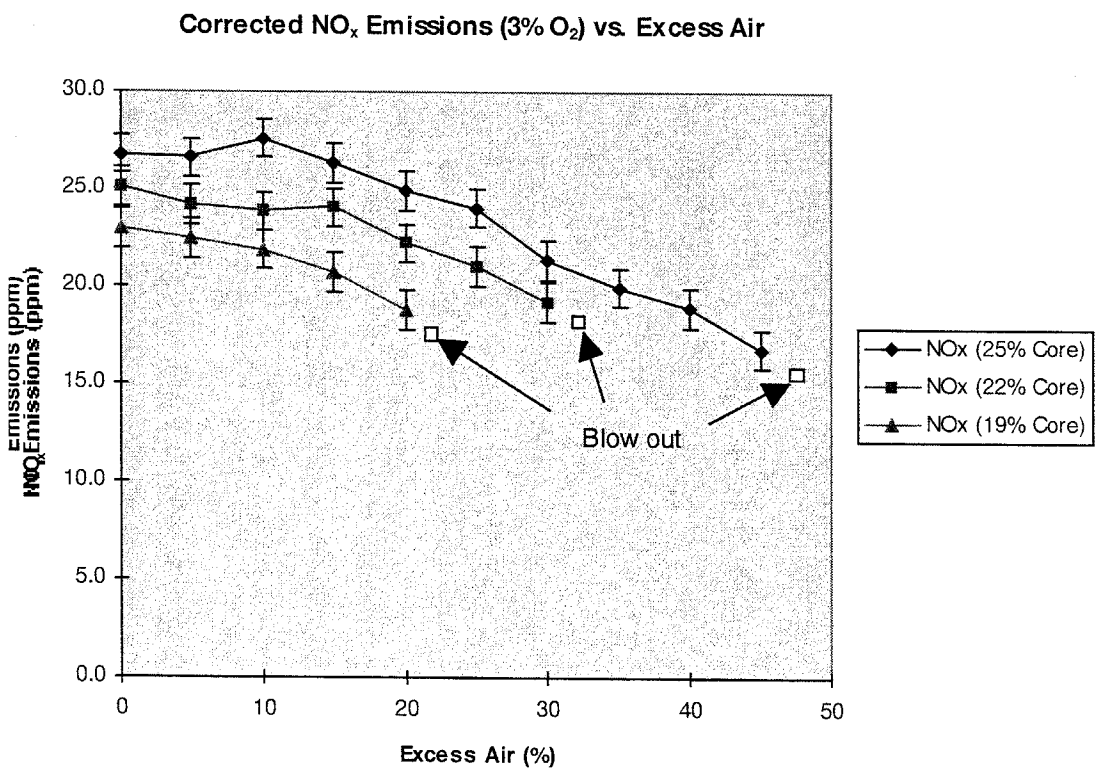

Figure 7.4: Impact of Core Fuel Flow on NO_X Emissions and Stability

Recall that these tests were all performed with a constant geometrical configuration. When the geometrical configuration was altered, such as decreasing the throat depth, the burner would then only

remain lit at the 22% and 25% core fuel flow rate for any excess air flow above 15%. The main conclusion drawn from these tests was to select 1.64 scfm (25% of 6.58) as the core fuel flow rate throughout the DoE matrix. Even though this did give the higher NO_X, it provided the largest stability range, which would be crucial considering the large variety of runs required for the DoE matrix.

These initial tests were also conducted to determine the ranges of the input factors in the DoE matrix. The throat depth was capable of changing from 0.75 inches to 1.50 inches, but due to a large decrease in stability below 1.125 inches, the range of variation was chosen to be between 1.125 and 1.50 inches. The radial depth was capable of moving between 0.00 and 0.625 inches. This parameter appeared to have a slight impact on stability but its full range was used in the matrix. The outer spud depth was capable of moving from 0.00 to 1.50 inches. Even though this large range was possible, the burner manufacturer specified that the depth should not be greater than 0.25 inches. Therefore, the range of 0.00 to 0.25 inches was chosen. The outer spud direction was selected to range between 0° and 45°. This was made on the basis of practicality rather than stability. If the angle of injection from the outer injectors was greater than 45°, they would have been injecting pure fuel directly opposite from the center of the reaction. Intuitively, this could lead to a large decrease in the combustion efficiency of the burner. The final factor is the percent fuel difference. In these initial stages, it was identified that injecting less than 30% of the total fuel flow through the radial injectors would make the burner largely unstable. Due to this, the range of the percent fuel difference factor was chosen as -5.0 to +5.0. This indicates that both the outer and radial fuel flows would range from 35% to 40% of the total flow. At +5.0, the outer fuel flow would be 2.63 scfm (40% of 6.58) and the radial fuel flow would be 2.30 scfm (35% of 6.58). At -5.0, these values would be reversed; the outer flow would be 2.30 scfm and the radial flow would be 2.63 scfm.

Much of the development process of the DoE test matrix was given previously in the *Design of Experiments* section. The matrix consists of six factors, each with a low and high value. The six factors and their associated ranges are further detailed in Figure 7.5

The three responses of this matrix are NO_X emissions (corrected to 3.0% O_2), combustion efficiency, and system efficiency based on heat extraction. The six factors and three responses were entered into a design development program to produce a half-fractional factorial test matrix. The design program automatically selects the combinations required and provides a randomized test matrix. An image of the first ten runs from this program was shown in Figure 7.3 but a table of all 69 runs is now given in Figure 7.6. All 69 tests were run and the data required for NO_X, combustion efficiency, and system efficiency were monitored for each run. The next section will explain the results and the statistical analyses.

FACTOR	LOW VALUE	HIGH VALUE	CENTER POINT	EXPLANATION
RADIAL DEPTH	0.000 in.	0.625 in.	0.3125 in.	Distance between top of radial injectors and base of distribution plate
THROAT DEPTH	1.125 in.	1.500 in.	1.3125 in.	Length of throat
EXCESS AIR	10%	30%	20%	Total amount of burner excess air flow
FUEL DIFFERENCE	-5.0%	+5.0%	0.0%	Percentage difference between outer and radial flow (%outer - %radial)
OUTER DEPTH	0.00 in.	0.25 in.	0.125 in.	Vertical distance between throat exit plane and outer injector
OUTER DIRECTION	0 deg.	45 deg.	22.5 deg.	Angle of outer injector in reference to burner centerline

Figure 7.5: Summary of Six Factors in DoE Test Matrix

Design Id	Run Order	Block Number	Radial Depth	Throat Depth	Excess Air	Outer Depth	Fuel Difference	Outer Direction	NOx (ppm)	Comb. Eff. %	Sys. Eff. 1 %
4	1	1	0.625	1.500	10	0.000	-5.0	0.0			
1	2	1	0.000	1.125	10	0.000	-5.0	0.0			
29	3	1	0.000	1.125	30	0.250	5.0	45.0			
7	4	1	0.000	1.500	30	0.000	-5.0	0.0			
15	5	1	0.000	1.500	30	0.250	-5.0	45.0			
3	6	1	0.000	1.500	10	0.000	-5.0	45.0			
7	7	1	0.000	1.500	30	0.000	-5.0	0.0			
18	8	1	0.625	1.125	10	0.000	5.0	0.0			
11	9	1	0.000	1.500	10	0.250	-5.0	0.0			
4	10	1	0.625	1.500	10	0.000	-5.0	0.0			
6	11	1	0.625	1.125	30	0.000	-5.0	0.0			
13	12	1	0.000	1.125	30	0.250	-5.0	0.0			
19	13	1	0.000	1.500	10	0.000	5.0	0.0			
24	14	1	0.625	1.500	30	0.000	5.0	0.0			
31	15	1	0.000	1.500	30	0.250	5.0	0.0			
17	16	1	0.000	1.125	10	0.000	5.0	45.0			
5	17	1	0.000	1.125	30	0.000	-5.0	45.0			
8	18	1	0.625	1.500	30	0.000	-5.0	45.0			
14	19	1	0.625	1.125	30	0.250	-5.0	45.0			
28	20	1	0.625	1.500	10	0.250	5.0	0.0			
32	21	1	0.625	1.500	30	0.250	5.0	45.0			
19	22	1	0.000	1.500	10	0.000	5.0	0.0			
24	23	1	0.625	1.500	30	0.000	5.0	0.0			
31	24	1	0.000	1.500	30	0.250	5.0	0.0			
10	25	1	0.625	1.125	10	0.250	-5.0	0.0			
23	26	1	0.000	1.500	30	0.000	5.0	45.0			
6	27	1	0.625	1.125	30	0.000	-5.0	0.0			
25	28	1	0.000	1.125	10	0.250	5.0	0.0			
32	29	1	0.625	1.500	30	0.250	5.0	45.0			
30	30	1	0.625	1.125	30	0.250	5.0	0.0			
22	31	1	0.625	1.125	30	0.000	5.0	45.0			
18	32	1	0.625	1.125	10	0.000	5.0	0.0			
12	33	1	0.625	1.500	10	0.250	-5.0	45.0			
0	34	1	0.313	1.313	20	0.125	0.0	22.5			
13	35	1	0.000	1.125	30	0.250	-5.0	0.0			
23	36	1	0.000	1.500	30	0.000	5.0	45.0			
8	37	1	0.625	1.500	30	0.000	-5.0	45.0			
2	38	1	0.625	1.125	10	0.000	-5.0	45.0			
0	39	1	0.313	1.313	20	0.125	0.0	22.5			
2	40	1	0.625	1.125	10	0.000	-5.0	45.0			
0	41	1	0.313	1.313	20	0.125	0.0	22.5			
22	42	1	0.625	1.125	30	0.000	5.0	45.0			
29	43	1	0.000	1.125	30	0.250	5.0	45.0			
26	44	1	0.625	1.125	10	0.250	5.0	45.0			
3	45	1	0.000	1.500	10	0.000	-5.0	45.0			
9	46	1	0.000	1.125	10	0.250	-5.0	45.0			
15	47	1	0.000	1.500	30	0.250	-5.0	45.0			
0	48	1	0.313	1.313	20	0.125	0.0	22.5			
11	49	1	0.000	1.500	10	0.250	-5.0	0.0			
10	50	1	0.625	1.125	10	0.250	-5.0	0.0			
26	51	1	0.625	1.125	10	0.250	5.0	45.0			
9	52	1	0.000	1.125	10	0.250	-5.0	45.0			
21	53	1	0.000	1.125	30	0.000	5.0	0.0			
21	54	1	0.000	1.125	30	0.000	5.0	0.0			
28	55	1	0.625	1.500	10	0.250	5.0	0.0			
17	56	1	0.000	1.125	10	0.000	5.0	45.0			
27	57	1	0.000	1.500	10	0.250	5.0	45.0			
20	58	1	0.625	1.500	10	0.000	5.0	45.0			
27	59	1	0.000	1.500	10	0.250	5.0	45.0			
12	60	1	0.625	1.500	10	0.250	-5.0	45.0			
20	61	1	0.625	1.500	10	0.000	5.0	45.0			
25	62	1	0.000	1.125	10	0.250	5.0	0.0			
0	63	1	0.313	1.313	20	0.125	0.0	22.5			
16	64	1	0.625	1.500	30	0.250	-5.0	0.0			
1	65	1	0.000	1.125	10	0.000	-5.0	0.0			
5	66	1	0.000	1.125	30	0.000	-5.0	45.0			
30	67	1	0.625	1.125	30	0.250	5.0	0.0			
14	68	1	0.625	1.125	30	0.250	-5.0	45.0			
16	69	1	0.625	1.500	30	0.250	-5.0	0.0			

Figure 7.6: Complete Design of Experiments (DoE) Test Matrix